
# Modeling of mineral-melt interfaces: an atomic scale view on partially molten rocks

**Dissertation zur Erlangung des Doktorgrades im Fachbereich Geowissenschaften an der Freien Universität Berlin**

**Samia Faiz Gurmani**

**Fachrichtung Geophysik**

**Berlin, 2012**

Erstgutachter: Dr. Sandro Jahn
Zweitgutachter: PD Dr. Ralf Milke

Tag der Disputation: 21.05.2012

# Erklärung

Hiermit versichere ich, daß ich die vorliegende Arbeit selbständig verfaßt und keine anderen als die angegebenen Hilfsmittel benutzt habe. Die Stellen der Arbeit, die anderen Werken wörtlich oder inhaltlich entnommen sind, wurden durch entsprechende Angaben der Quellen kenntlich gemacht.

Diese Arbeit hat in gleicher oder ähnlicher Form noch keiner Prüfungsbehörde vorgelegen.

A part of this work entered into this publication:

**Gurmani**, **S.**; **Jahn**, **S.**; **Brasse**, **H.**; **Schilling**, **F. R.** (**2011**) : Atomic scale view on partially molten rocks: Molecular dynamics simulations of melt-wetted olivine grain boundaries. Journal of Geophysical Research, 116, B12209. doi 10.1029/2011JB008519

This work is dedicated to my brothers, husband, and son

# Acknowledgments

I thank God for his grace, wisdom, favor, faithfulness and providing me the opportunity to step in the excellent world of science.

The long journey of my doctoral study has ended. It is with great delight that I acknowledge my debts to those who have great contribution for the success of the project. First and foremost, I am highly indebted to my supervisor Dr. Sandro Jahn for his, guidance, constructive comments and encouragement. I was very lucky to benefit from his rich expertise and critical comments that built my scientific proficiency. He has stimulated me to work hard because of his valuable input. He was very friendly, considerate and always polite to me during the years of my stay at the GFZ. He was always there for me when I needed motivation during the difficult stages of the PhD work and was kind enough to share my personal issues. I hope that our cooperation will continue in the future.

Furthermore, I would like to express my appreciation to Dr. Heinrich Brasse. I have benefited a lot from your experience, critical comments and advice. You have been a constant inspiration to me and your support has contributed enormously to the success of this project. Your office doors were always open to me when I needed advice and support; not only in my academic life but also dealing with my administrative difficulties. Especially, I owe my thanks to Prof. Dr. Frank R Schilling for his extensive discussions around my work and interesting explorations in project have been very helpful.

I would also like to thank Dr. Piotr Kowalski and Dr.Sergio Speziale for proof reading of this dissertation and fruitful scientific discussions. My officemates: George Speakermann

for introducing large variety of sweets and chocolates in office and his nice scientific discussion was always very helpful for me, and Dr. Omar Adjaouad, who was supportive in every way. A very special thank to Volker Haigis for his time and help during an important part of my project and translating summary into German language. My special thanks to whole section 3.3, for their friendly environment. I would like to thank Frau Beate Hein for solving administrative problems at GFZ. Especially, many thanks go to Hans-Peter Nabein and Reiner Schulz, they always helped me regarding my computer problems and other technical stuff.

My stay in Germany was made easy due to company of many friends in Berlin and Marburg. I would like to thank Waqas, Faheem and Azhar from Marburg, and Farooq bhai, Asma and Hajra from Berlin.

This research would have never been realized without the persistence and endurance of my husband and son. You two with your support made this achievement joyful and an excellent experience for me. I see myself unable to even express my feelings about the love and patience that I observed from you. Thanks for everything.

I finish with Pakistan, where the most basic source of my life energy resides: my family. I have an amazing family, unique in many ways. Their support has been unconditional all these years; they have cherished with me every great moment and supported me whenever I needed it. Especially Bibi and Paru for daily phone calls with their entertaining chit chat and care. I have no unique and precious words to thank my Lalas (brothers) Aslam Gurmani and Akram Gurmani, who supports me financially and morally at every step of my life; it's all because of you both. I also would like to thank my in laws for their support and love. Last but not least my Mom; for love support and infinite prayers.

# Summary

Partial melting is an important geological process in the deep Earth that affects physical, chemical and rheological properties of rocks. The effect of partial melting on mantle dynamics depends on both the amount of melt and how it is distributed within the crystalline matrix. A few percent of melt have potentially large effect on the physical properties of rocks. In this work, atomic scale simulations are used to study the structure and transport properties of ultrathin melt films between olivine grains, which is a simple model system of partially molten peridotite.

The model system consists of 0.8 to 7.0 nm thick layers of magnesium silicate melt with a composition close to $MgSiO_3$ (enstatite) confined between $Mg_2SiO_4$ forsterite crystals. We examine how the atomic structure, the chemistry and the self-diffusion coefficients vary across the interface and investigate their dependence on the thickness of the melt layer and the crystal orientation. The particle interactions are represented by an advanced ionic model. From the particle trajectories, we derive various properties, like charge densities, cation coordinations, chemical compositions, and self-diffusion coefficients. Interfacial layers of up to 2 nm thickness show distinctly different physical behavior than the bulk melt and the bulk mineral.

The simulation results indicate that for crystal orientations with higher surface energy, the self-diffusion coefficients of all ionic species in the melt decrease at constant melt layer thickness. By increasing the melt layer thickness between the crystals, the average mobility of ions in the melt is increased. On the interfacial part the charge mobility of all species decreases due to solid-like ordering between atoms. For modeling the petro-

physical behavior of partially molten rocks, the effective diameter for the conducting channels is reduced by up to two nanometers, which effects the rheological and transport properties of partially molten rocks, especially in the presence of ultra-thin melt films in well-wetted systems. In the latter case, the electrical conductivity of the confined melt in a partially molten rock could be reduced up to a factor of two due to interfacial effects.

A slight difference is observed in the interfacial properties due to change in chemical composition, pressure and temperature conditions. When calcium is added to the system, the self-diffusion coefficients of all species slightly change. At different pressure and temperature, a huge difference is observed in the self-diffusion coefficients. Freezing of the system and confinement effect is clearly observed at 2000 K with pressure of 10 GPa, and at 2400 K with 10 GPa pressure.

Non-equilibrium molecular dynamics simulations with constant shear rate are performed on this system showing complex rheological behavior in the vicinity of interfaces. A dependence of the viscosity on shear rate is observed which constitutes *non-Newtonian* behavior of the melt at the high shear rates accessible to molecular dynamics. The viscosity calculated from non-equilibrium molecular dynamics simulations is found to be somewhat higher then the viscosity calculated from equilibrium molecular dynamics simulations. The viscosity at the lowest modeled shear rate is in good agreement with the experimental viscosity.

# Zusammenfassung

Das partielle Aufschmelzen von Gestein ist ein wichtiger geologischer Prozess in der tiefen Erde, der seine physikalischen, chemischen und rheologischen Eigenschaften beeinflusst. Die Wirkung von partiell geschmolzenem Gestein auf die Manteldynamik hängt sowohl von der Menge der Schmelze als auch von ihrer Verteilung in der kristallinen Matrix ab. Einige wenige Prozent Schmelzanteil können einen großen Einfluss auf die physikalischen Eigenschaften des Gesteins haben. In dieser Arbeit werden Simulationen auf atomarer Ebene durchgeführt, um die Struktur und Transporteigenschaften ultradünner Schmelzfilme zwischen Olivinkörnern zu untersuchen, die ein einfaches Modellsystem für partiell geschmolzenen Peridotit darstellen.

Das Modellsystem besteht aus 0.8 bis 7.0 nm dicken Schichten von Magnesiumsilikat schmelze mit einer Zusammensetzung in der Nähe von $MgSiO_3$ (Enstatit), die seitlich von Forsterit-Kristallen ($Mg_2SiO_4$) begrenzt werden. Wir untersuchen die Änderung der atomaren Struktur, der chemischen Zusammensetzung und der Selbstdiffusionskoeffizienten entlang eines Profils senkrecht zur Grenzfläche sowie ihre Abhängigkeit von der Dicke der Schmelzschicht und der Orientierung der Kristalle. Die Wechselwirkung zwischen den Atomen wird durch ein erweitertes ionisches Modell beschrieben. Aus den atomaren Trajektorien erhalten wir verschiedene Eigenschaften wie die Ladungsdichte, Koordinationszahlen der Kationen, die chemische Zusammensetzung und Selbstdiffusionskoeffizienten. Grenzflächenschichten von bis zu 2 nm Dicke weisen ein deutlich anderes physikalischen Verhalten auf als ausgedehnte Schmelzen und Mineralien.

Die Ergebnisse der Simulationen zeigen, dass für Kristallorientierungen mit höherer

Oberflächenenergie die Selbstdiffusionskoeffizienten aller Ionen in der Schmelze bei konstanter Dicke der Schmelzschicht niedriger sind. Mit wachsender Dicke der Schmelzschicht zwischen den Kristallen erhöht sich die durchschnittliche Mobilität der Ionen in der Schmelze. Nahe der Grenzfläche ist die Ladungsmobilität niedriger, da sich dort eine festkörperartige Anordnung der Atome ausbildet. Für die Modellierung des gesteinsphysikalischen Verhaltens von partiell geschmolzenem Gestein ergibt sich, dass der effektive Durchmesser von leitenden Kanälen um bis zu 2 nm verringert ist, was sich auf die Rheologie und die Transporteigenschaften von partiell geschmolzenem Gestein auswirkt, besonders in Anwesenheit von ultradünnen Schmelzfilmen in gut benetzten Systemen. In diesem Fall könnte sich die elektrische Leitfähigkeit der seitlich eingeschlossenen Schmelze in partiell geschmolzenem Gestein aufgrund von Grenzflächeneffekten um einen Faktor von bis zu 2 verringern.

Bei den Grenzflächeneigenschaften werden bei Änderung der chemischen Zusammensetzung, des Drucks und der Temperatur kleine Unterschiede beobachtet. Wird Calcium zum System hinzugefügt, ändern sich die Selbstdiffusionskoeffizie ten aller Ionen leicht. Bei unterschiedlichen Druck- und Temperaturbedingungen werden stark veränderte Selbstdiffusionskoeffizienten beobachtet. Ein Einfrieren des Systems und ein Einschließungseffekt sind deutlich sichtbar bei 2000 K und einem Druck von 10 GPa, ebenso bei 2400 K und 10 GPa.

Auch Nicht-Gleichgewichts-Molekulardynamik mit einer konstanten Scherrate wurde mit diesem System durchgeführt. Sie zeigt ein kompliziertes rheologisches Verhalten in der Nähe der Grenzflächen an. Es wird eine Abhängigkeit der Viskosität von der Scherrate beobachtet, was ein nicht-Newtonsches Verhalten der Schmelze bei den hohen Scherraten darstellt, die mit molekulardynamischen Simulationen erreicht werden können. Die mit Hilfe von Nicht-Gleichgewichts- Molekulardynamik berechnete Viskosität ist etwas größer als die mit Hilfe von Gleichgewichts-Molekulardynamik bestimmte. Die

Viskosität, die sich mit der niedrigsten modellierten Scherrate ergibt, stimmt gut mit der experimentell bestimmten Viskosität überein.

# Table of Contents

# List of Figures

# List of Tables

# Chapter 1

# Introduction

The evolution of the Earth, its present structure and dynamics depends on processes that take place beneath and upon its surface (Poirier, 2000). For the understanding of these processes, we need to investigate the chemical composition, temperature and pressure conditions, and the phases present at the conditions of the Earth's interior. Direct access to rock samples is limited to about 10 km depth (Kozlovsky and Andrianov, 1987). Most of our understanding of the deeper interior of the Earth comes from seismological observations, geomagnetic and gravity measurements made at the surface (Anderson, 1989).

Experimental and theoretical determinations of material properties at extreme pressures and temperatures are of primary importance in the study of the Earth's interior. Numerical modeling of mantle and core dynamic behavior, and computer simulation of minerals and rocks also play an important role in studies of the composition, structure and internal dynamics of our planet (Gillan et al., 2006). The presence of partial melts has a major influence on the physical, chemical and rheological behavior of crustal and mantle rocks (Kohlstedt and Holtzman, 2009). The process of partial melting is considered very important for the chemical differentiation in the Earth's crust and mantle. Our knowledge about Earth's past and present state and dynamics are dependent on an understanding of the nature of partial melting (Karato, 1986). The availability of mobile ions as charge carriers makes partial melts a primary source of increased electrical conductivity in the deep Earth (Toffelmier and Tyburczy, 2007).

Partial melting takes place at different geological environments, from granitic partial melts in the continental crust to basaltic or carbonate partial melts in the upper mantle. Partial melting is considered to be very important for the chemical differentiation of the Earth, and partial melt is the initial process of magmatism. Partial melting takes place in the Earth's mantle, when minerals with lower melting points, like feldspars and pyroxenes, melt and leave behind olivine crystals, forming basaltic magma. Magma formation is strictly connected to the large scale convection of the mantle (Tackley, 2012). After the formation, magma migrates upward into Earth's crust, starts cooling and then solidifies. Parts of the mantle are expected to partially melt in e.g. subduction zones, the vicinity of hotspot ,and at mid-ocean ridges (see Fig. 1.1).

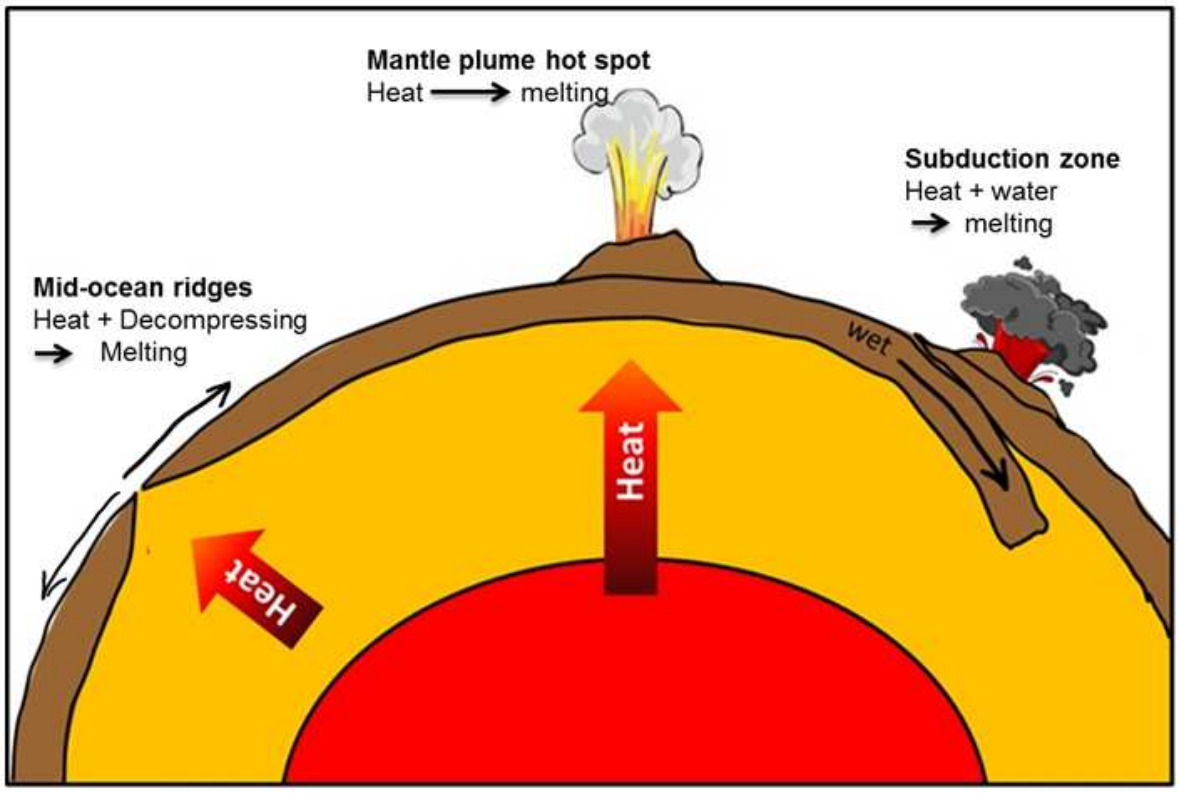


Fig. 1.1: Occurrence of different type of partial melt (magma) in three different geological settings: basaltic mid ocean ridges, subduction zone and hotspot.

The most productive source of magma are mid-ocean ridges where magma generated

by decompression melting rises to the surface and produces oceanic crust of gabbro and basalt. Partial melting occurs in the mantle wedge above subducting lithospheric slabs, triggered by fluids released from the sinking lithospheric material (Tatsumi, 1989; Davies and Stevenson, 1992). In hotspots, magma ascend from very deep in the Earth's mantle, probably from the boundary between the core and the base of the mantle. The magmas produced are basaltic and have a similar major elements composition as mid-ocean ridge basalts. The initial composition of the magma depends on the source rock, and on the degree of partial melting. Melting of a mantle source gives a basaltic magma while melting of a crustal source causes more siliceous magmas. But this initial magma composition changes during transport towards surface or during storage in the crust (Anthony et al., 2011; Anderson, 2007).

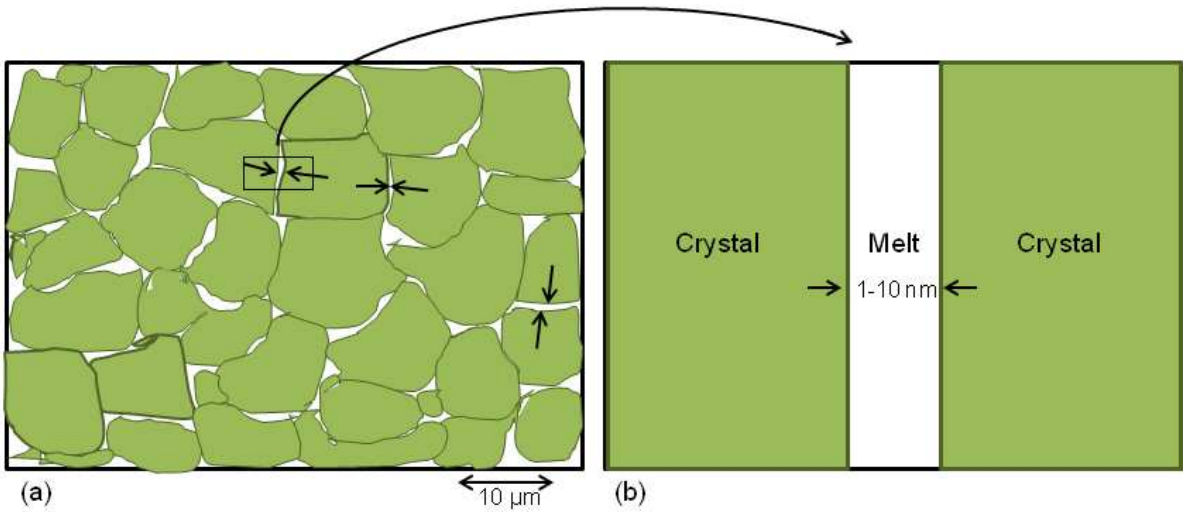


Fig. 1.2: (a) Sketch of melt distribution and fraction of melt between olivine grains. (b) Related sketch of our system to study the melt (about 1-10 nm) between olivine grains on atomic scale. Green area represents olivine grains and white area is the confined melt between grains.

Partially molten rocks are widely investigated in laboratory studies (Yoshino et al., 2005; ten Grotenhuis et al., 2005). A schematic diagram of the distribution of melt between olivine grains with continuously changing local melt fraction is shown in figure 1.2(a). From experimental approach, it is not possible to study the structural and

transport properties of ultra thin melt films confined between solid at nanoscale. By using molecular dynamics simulations we can study such ultra thin melt film on atomic scale. Figure 1.2(b) shows the sketch of our studied system of ultra thin melt film confined between two olivine grains.

The majority of the Earth's upper mantle consists of olivine (Agee, 1998). In fact, magnesium-rich olivine is the majority ingredient (about 60 % of the rock) of the rock peridotite, the main component of Earth's upper mantle (Walker et al., 2003). The composition of peridotite varies widely, reflecting the relative proportion of pyroxenes, plagioclase, spinel, garnet and amphibole (Winter, 2001). peridotitic rocks are assumed to make up much of the volume of the Earth's mantle (Putnis, 1992).

Olivins are a family of closely related silicates which crystallize with orthorhombic symmetry (Deer et al., 1997). $M_2SiO_4$ is the general formula of olivine minerals, where M is e.g. Mg, $Fe^{2+}$ or Ca. Most natural olivines have a composition of the continuous solid solution the two end-members magnesium silicate (forsterite) $Mg_2SiO_4$ and iron silicate (fayalite) $Fe_2SiO_4$.

The structure of olivine consists of isolated $SiO_4$ tetrahedra connected by divalent cations in sixfold coordination (Fig. 1.3). The olivine structure can be described as either an orthosilicate or a distorted hexagonally close packed (HCP) lattice of oxygens. Half of the octahedral sites of the oxygen lattice are occupied by magnesium or iron and one eighth of the tetrahedral sites occupied by silicon (Bragg and Brown, 1926). Figure 1.3 shows the arrangement of the isolated $SiO_4$ tetrahedra pointing alternately up (red) and down (green) along rows parallel to the c-axis. In the olivine structure, there are two slightly different octahedral metal sites M1 and M2. The M2 sites are larger and more distorted from the regular geometry and M1 site is more regular.

$Mg_2SiO_4$-forsterite is the Mg end-member of olivine, and remains always of primary

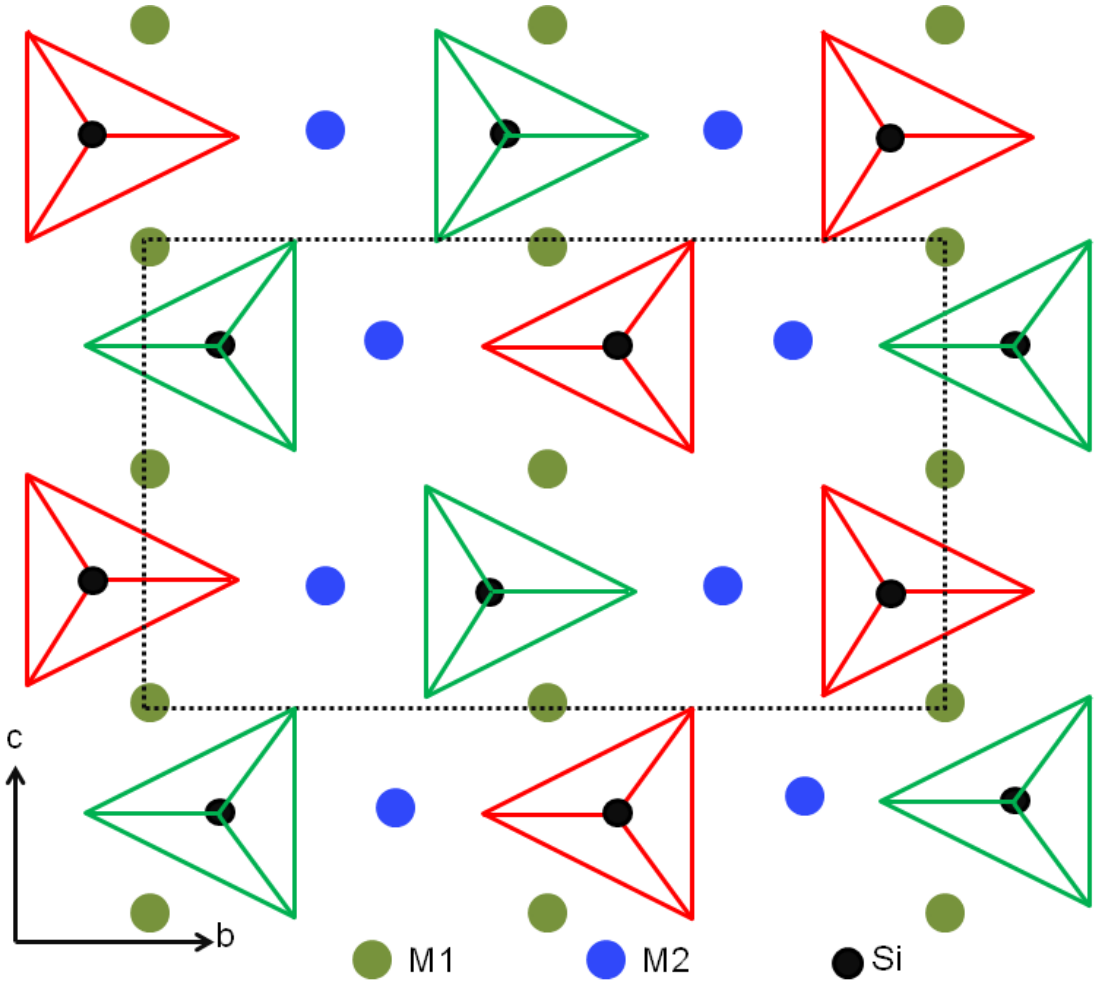


Fig. 1.3: Structure of olivine which shows the possible M1 and M2 sites, and connectivity of $SiO_4$ tetrahedra, which point alternately up and down along the rows parallel to c-axis. Black dotted box represents the unit cell.

interest to scientists. Thermoplasticity of olivine is responsible for the motion of the continental plates. Furthermore, the olivine-to-wadsleyite phase transition at high pressure and high temperature is responsible for a major seismic discontinuity at a depth of 410 $km$ (Bina, 1997).

The literature and the previous work done on partially molten mantle rocks prove the importance of these rocks and olivine, and their crucial role in determining physical properties and dynamic behavior of the upper mantle of the Earth. A number of investigations of partial melting and the properties of partially molten rocks have been

performed and published the results (Waff and Bulau, 1979; de Kloe et al., 2000; Riley and Kohlstedt, 1990; Kohlstedt, 1992; Hirth and Kohlstedt, 1995; Kohlstedt and Zimmerman, 1996; Mei and Kohlstedt, 2000; Mei et al., 2002).

Interconnectivity of melt strongly influences the electrical conductivity of partially molten rocks (Sato and Ida, 1984; Partzsch et al., 2000). Electrical conductivity of the asthenosphere is difficult to resolve by deep electromagnetic sounding due to the abundance of high conductivity zones in the crust which blur the image at depth. The clearest indications for an enhanced conductivity originate from cratonic areas (Eaton et al., 2009) and from studies of the oceanic asthenosphere (Baba et al., 2006). Under favorable conditions, the asthenospheric wedge beneath volcanic arcs may be resolved (Brasse and Eydam, 2008). The electrical properties of minerals and rocks are strongly dependent on temperature, pressure, composition, melt distribution, point defect chemistry and also frequency at which measurements are made (Roberts and Tyburczy, 1993).

Systematic experimental studies have been made to have a better understanding of the influence of an existing melt or fluid on rock properties such as seismic velocities or the electrical conductivity. *Schmeling* (Schmeling, 1985, 1986) showed that the physical properties of a rock are not only determined by the total amount but also by the distribution of the melt or fluid phase on the grain scale. *Robert and Tyburczy* (Roberts and Tyburczy, 1999) investigated the electrical response of an olivine-basalt partial melt as a function of temperature. The relation of electrical conductivity, degree of partial melting and melt distribution was studied by *Partzsch et al.* (Partzsch et al., 2000). Partial melting of mafic rocks under pressure and electrical conductivity is also recently studied by *Maumus et al.* (Maumus et al., 2005). Electrical conductivity of olivine and its dependence on melt distribution was described by *ten Grotenhuis* (ten Grotenhuis et al., 2004, 2005).

The concept of dihedral wetting angle is often used to describe the melt micro-structure and the connectivity of adjacent melt pockets (Waff and Bulau, 1979). Theory predicts that the distribution of melt on the grain boundaries is determined by the difference between interfacial energies of grain boundaries and melt-crystal interfaces (Waff and Bulau, 1982). Subsequent studies have shown that flat crystalline interfaces co-exist with smoothly curved crystal-melt interfaces in equilibrium micro-structures of ultramafic partial melts (Waff and Faul, 1992) and that a single dihedral angle expression is inappropriate for olivine due to its distinct surface energy anisotropy (Cmiral et al., 1998).

The dihedral angle becomes very small or even approaches zero degrees towards high pressure and temperature in well wetted partially molten peridotite (Yoshino et al., 2009) allowing for very thin melt layers. Fluid filled pore geometry in texturally equilibrated rocks characterized by dihedral angles and degree of faceting was investigated by measuring the grain boundaries wetness by *Yoshino* and his co-workers (Yoshino et al., 2005; Yoshioka et al., 2007).

*Hess* (Hess, 1994) showed that the thermodynamics of thin confined fluid films depends crucially on the film thickness and the film tension. Ultrathin amorphous films (1-2 nm) were found in olivine grain boundaries in mantle xenoliths (Wirth, 1996; Drury and Fitz Gerald, 1996; de Kloe et al., 2000). They provide evidence for the existence of thin melt layers in the grain boundaries during partial melting. Chemical analysis across olivine grain boundaries in three specimens (a peridotite ultramylonite, olivine phenocrysts in a basaltic rock and synthesized compacts of olivine + diopside) (Hiraga et al., 2003) showed an enrichment of trace elements in an interfacial layer of about 5 nm thickness. *Faul et al.* (Faul et al., 2004) studied olivine-olivine grain boundaries in melt-bearing olivine polycrystals and observed a region of about 1 nm thickness that is structurally and chemically different from the olivine grain interiors. Several

experimental studies have been published on the rheological behavior of partially molten mantle aggregates (Cooper and Kohlstedt, 1984; Bussod and Christie, 1991; Kohlstedt and Zimmerman, 1996). The effect of melt distribution and grain size on the rheology of mantle rocks was reviewed by *Kohlstedt and Zimmerman* (Kohlstedt and Zimmerman, 1996) and *Kohlstedt and Holtzman* (Kohlstedt and Holtzman, 2009).

Knowledge of viscosity of mantle silicate melts is necessary in order to quantitatively model volcanic and magmatic processes. The relationship between viscosity of a partially molten rock and melt fraction is critically very important for the characterizing the rheological behavior of the interior of Earth. With the addition of only 1-3 vol% of melt, the viscosity of partially molten rocks decreases by a factor of 2-5, such as MORB (Cooper and Kohlstedt, 1986; Kohlstedt and Zimmerman, 1996; Mei et al., 2002). Viscosity of magma is a critical parameter to understand the igneous processes, such as melt segregation and migration in source regions, magma mixing, magma recharge, differentiation by crystal fractionation, convection in magma chambers, and magma fragmentation. Viscosity controls variety of theses processes like rates of crystal growth and convection dynamics (Solomatov and Stevenson, 1993a; Tonk and Melosh, 1990). Viscosity must also have influenced the rate of cooling of the early Earth. In addition, the transport properties of magma would have strongly influenced early differentiation mechanisms. Processes in which viscosity and diffusivity of molten mantle would have been important include chemical equilibration between silicates and core forming metallic liquids and the physics of crystal settling in a convecting magma ocean (Rubie et al., 2003; Solomatov and Stevenson, 1993b).

Many research groups have measured viscosity of silicate melts experimentally at different pressure and temperature (Kushiro, 1978a,b; Urbain et al., 1982; Reid et al., 2003; Liebske et al., 2005). Different models are developed to estimate the viscosity of silicate melts (Bottinga and Weill, 1972; Baker, 1996; Hess and Dingwell, 1996; Giordano and

Russell, 2007; Hui and Zhang, 2007; Giordano et al., 2008). These models are very helpful to estimates the viscosity which have strong compositional dependence. Non-equilibrium molecular dynamics simulations are very useful to calculate viscosity at the atomic level (Ashurst and Hoover, 1975; Cummuings and Morriss, 1987; Fuller and Rowley, 1998). In non-equilibrium molecular dynamics simulations, shear is applied directly to the simulation cell. From equilibrium molecular dynamics simulations, viscosity is calculated from stress auto correlation functions (Allen and Tildesley, 1987). *Adjaoud et al* (Adjaoud et al., 2011) calculated transport properties of liquid $Mg_2SiO_4$ at high pressure from stress auto correlation functions by applying molecular dynamics simulations. Recently shear viscosity of $MgSiO_3$ was calculated from molecular dynamics simulation using a pair-wise additive potential at different temperature by *Nevins et al* (Nevins et al., 2009) and viscosity of molten $Mg_2SiO_4$ at different pressure using molecular dynamics simulation was calculated by *Martin et al* (Martin et al., 2009). From first principles molecular dynamics simulations, viscosity of $MgSiO_3$ liquid at condition of Earth's mantle was also calculated by *Wan et al.* (Wan et al., 2007) and *Karki et al.* (Karki and Stixrude, 2010). Both, molecular dynamics simulation and first principle simulation show good agreement with experimental results.

Hence, an understanding of the mechanical and physical properties of olivine and partial melts of olivine rich mantle rocks has major geophysical importance. Ultimately, it is desirable to have a description of the olivine on an atomic scale, specifying the atomic interaction between particles. From such a description it is possible to predict its physical and thermal properties at any temperatures and pressures which is not accessible in the laboratory. We perform classical molecular dynamics (MD) simulation to study the structure of olivine-melt interfaces on atomic scale.

Molecular dynamic (MD) simulations has been widely used for analyzing the structures and properties of minerals and melts. MD simulations provide valuable information

especially at high temperature and high pressure where conventional experiments are difficult to perform or sometime impossible. With the development of the molecular dynamics simulation techniques, it became possible to calculate from a given interaction model a very wide range of physical properties of solid and liquids, such as structural and transport properties and dynamical response functions.

Molecular modeling techniques have been successfully used in many studies to investigate the atomic structure and physical properties of various types of solid-liquid interfaces. This includes classical force field and *ab initio* molecular dynamics simulations of melting behavior of oxides and silicates, e.g. (Belonoshko and Dubrovinsky, 1996; Alfe, 2005) or detailed structural investigations of solid-liquid interfaces of ionic systems, e.g. (Lanning et al., 2004). Confinement effects on melting and freezing of confined material were reviewed, e.g., by *Alcoutlabi and McKenna* (Alcoutlabi and McKenna, 2005) and *Alba − Simionesco et al.* (Alba-Simionesco et al., 2006).

In this thesis, the physical properties of mineral-melt interfaces are investigated on atomic level using molecular dynamics simulations. We study the structure, chemistry and transport properties of ultrathin melt films confined between olivine crystals as a simple model system of partially molten peridotite. The studied model system consists of magnesium silicate melt which is close to the composition of enstatite $MgSiO_3$ and confined between crystals of forsterite $Mg_2SiO_4$. In addition, the shear viscosity of the confined melt is studied by non-equilibrium molecular dynamics simulations.

In the first part, the structural and transport properties of mineral-melt interfaces are investigated using equilibrium molecular dynamics simulation. The structural and transport properties are calculated for three different types of crystal surface terminations to investigate the effect of grain orientation on interfacial and melt properties. Different sizes of melt thicknesses are used to observe the effect of thin melt films confined between crystals. As pressure and temperature conditions are a very important factor to

study the properties of mineral-interfaces, the effect of different P-T conditions on our system is also studied.

In the second part, non-equilibrium molecular dynamics simulation is used to calculate the melt viscosity. A constant shear rate is applied to the interface and the respective viscosity is derived. The dependence of the viscosity on shear rate is investigated. For reference, the viscosity of bulk melt is calculated from both equilibrium molecular dynamics and non-equilibrium molecular dynamics simulations.

Finally, some implications of the results on the electrical conductivity of partially molten rocks are discussed.

# Chapter 2

# Simulation Techniques

Computer simulations on the atomic scale have become a powerful and standard method to investigate many-body problems in various scientific fields of physics, chemistry, biology and especially in material sciences. They allow to model the properties of macroscopic systems by reference to their microscopic structure. Studies of the behavior of materials in a wide range of physical conditions ( such as extreme pressure (P) and temperature (T)), which are not always accessible experimentally, can be done by simulation.

There are different approaches for atomic scale computer simulation of materials. They can be divided into two categories, one is based on classical and the other on a quantum mechanical description of particle interactions. Classical molecular dynamics simulations use potential models and are especially suited to apply for long simulation times and large simulation cells. Quantum mechanical methods ( also referred to as ab-initio or first principles methods ), such as density functional theory generally give a more accurate solution but are computationally much more expensive, which puts limit on the simulation cell size and time scale. Density functional theory is the most time-efficient approach to compute the electronic structure of many-electron systems.

For molecular dynamics simulations, length scales range from 0.1-10 nm and time scales are typically in the range of femtoseconds to nanoseconds. The accessible range in terms of time and length scales for classical and quantum methods is shown in figure 2.1. Classical molecular dynamics simulation is used for this study as a reliable modeling of

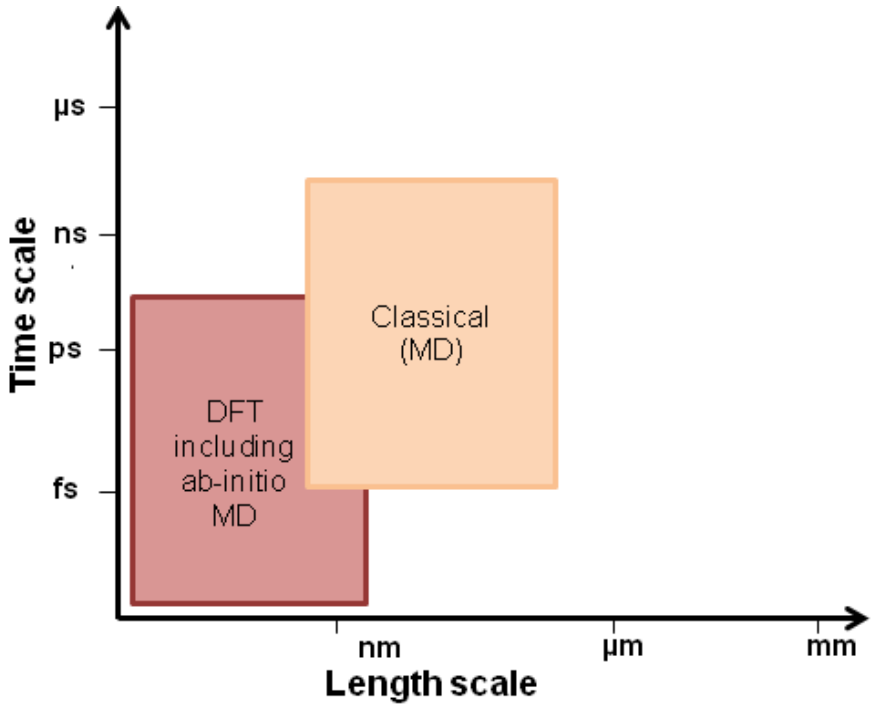


Fig. 2.1: Time and length scale range for density functional theory and classical molecular dynamics simulations.

the structure and transport properties of crystal-melt interfaces requires large simulation cells and long simulation times. This is not possible with density functional theory because it would be computationally too expensive to model a system with thousands of atoms. In this chapter, classical simulation methods used for this study are outlined.

## 2.1 Potential Models

To study the behavior of any material accurately using classical methods requires a good and transferable interaction potential.

Interatomic potentials for oxide materials have been developed over the years by using ionic models and describing the interaction between particles in terms of pair potentials of the Born-Mayer and Buckingham form (Catlow et al., 1988). Polarization effects

may be treated by choosing the shell model (Dick and Overhauser, 1958) or the method introduced by *Wilson* and *Madden* (Wilson and Madden, 1993). There are two ways to parametrize interatomic potentials, either empirically by adjusting the potential parameters to achieve the best possible agreement between calculated and experimental properties (crystal structures, dielectric and elastic constants) (Matsui, 1999, 2000) or determined theoretically via *ab initio* calculations (Kendrick and Mackrodt, 1983; van Beest et al., 1990; Tangney and Scandolo, 2002; Aguado et al., 2003b; Madden et al., 2006).

### 2.1.1 Rigid Ion Model

The rigid ion model (RIM) is the simplest and computationally least expensive approach. In this model the ions are considered as rigid bodies, in which deformation and polarization are neglected. A typical potential form used in this model is given by (Catlow et al., 1988).

$$V_{ij}(r_{ij}) = \frac{z_i z_j}{r_{ij}} + B_{ij} e^{\frac{-r_{ij}}{\rho_{ij}}} - \frac{C_{ij}}{r_{ij}^6} - \frac{D_{ij}}{r_{ij}^8} \tag{2.1}$$

where $r_{ij}$ is the distance between atoms $i$ and $j$, $z_i$ and $z_j$ are the effective charges associated with the atoms $i$ and $j$ respectively. The first term of the equation is the electrostatic potential of point charges (Coulombic potential) and is generally evaluated by using the Ewald summation method (see section 2.1.4) (Allen and Tildesley, 1987; Frenkel and Smit, 2001). The second term represents the repulsive interaction between ions due to the overlap of their electron charge densities at short distances. The repulsion is modeled to decay exponentially with distance, $B_{ij}$ and $\rho_{ij}$ are parameters that depend on the type of interacting ions. The last two terms represent the van der Waals dispersion, considering a sum of dipole-dipole and dipole-quadrupole attraction with

parameters $C_{ij}$ and $D_{ij}$.

The advantage of this potential is that it has a small number of parameters and it is fast for large systems and for long simulations. *Guillot* and *Sator* (Guillot and Sator, 2007a,b) have used this type of potential to study some properties of silicates melts in a wide range of chemical compositions and pressure.

*Matsui* developed a transferable interatomic potential model of this type to describe the four component system CMAS ($CaO$-$MgO$-$Al_2O_3$-$SiO_2$) which produces satisfactorily the structure, the molar volume and bulk modulus (Matsui, 1994, 1996). Later on, this study was extended to NCMAS ( $Na_2O$-$CaO$-$MgO$-$Al_2O_3$- $SiO_2$) system (Matsui, 1998a). In Matsui's original model the van der Waals coefficients are regarded as fitting parameters.

It has been shown that rigid ion model is too simple as it does not consider the non-central forces which are very important in ionic systems composed of ions with large polarizabilities, like oxides (Catlow et al., 1976; Cohen et al., 1987; Wilson et al., 1996c,b). *Matsui* extended the model by introducing ionic polarization in the form of shell model. Furthermore, the repulsive radii of ions are allowed to deform isotropically under the effect of other ions in the crystal (Matsui, 1998b, 1999). This is so called breathing shell model (BSM) has two additional parameters each polarizable and deformable type of ion. *Matsui et al.* show that MD simulation with the BSM is a very successful approach in reproducing very accurately not only the measured crystal structures and elastic constants of MgO, CaO and the $Mg_2SiO_4$ polymorphs but also their pressure and temperature dependencies over wide T, P ranges (Matsui, 1999; Matsui et al., 2000). Later in 2000, this method was applied to observe structural and transport properties of $MgSiO_3$ perovskite over wide temperature and pressure ranges where experimental data are available (Matsunaga, 2000).

### 2.1.2 Aspherical Ion Model (AIM) Model

The Aspherical Ion Model follows the same idea as the (BSM). However, it is constructed in a more systematic way and it includes explicitly all contributions to the ionic interactions assumed to be important. It treats ions as formally charged, closed shell particles.

A detailed description of the AIM and its parametrization using *first principles* methods has been described by *Aguado et al.* and *Madden et al.* (Aguado et al., 2003a; Madden et al., 2006). An accurate and transferable set of AIM potential parameters for the CMAS system was presented by *Jahn* and *Madden* (Jahn and Madden, 2007). The following description of the of AIM model is taken from the paper of *Jahn* and *Madden* (Jahn and Madden, 2007): "The AIM model is based on the classical theory of intermolecular forces (Stone, 1996) and constructed from four components: the charge-charge interaction and dispersion interactions, a polarizable part and short-range repulsion terms.

$$V = V^{qq} + V^{disp} + V^{rep} + V^{pol} \tag{2.2}$$

The first two components, the charge-charge and dispersion are pairwise additive as in the normal Born-Mayer-type pair potential. The first term ($V^{qq}$) charge-charge interaction is simple a Coulomb potential between ions $i$ and $j$ separated by some distance $r_{ij}$

$$V^{qq} = \sum_{i \leq j} \frac{q^i q^j}{r^{ij}}, \tag{2.3}$$

with $q^i$ being the formal charge on ion $i$ (-2 for O, +3 for Al, +4 for Si, +2 for Mg and Ca). Dispersion effects are represented by dipole-dipole and dipole-quadrupole terms

$$V^{disp} = -\sum_{i \leq j} [1 - f_6^{ij}(r^{ij})] \frac{C_6^{ij}}{(r^{ij})^6} + [1 - f_8^{ij}(r^{ij})] \frac{C_8^{ij}}{(r^{ij})^8} \tag{2.4}$$

where $C_6^{ij}$ and $C_8^{ij}$ are the dipole-dipole and dipole-quadrupole dispersion coefficients respectively, and $f_n^{ij}$ are Tang-Toennies dispersion damping functions (Tang and Toennies, 1984), which describe short-range corrections to the asymptotic dispersion term:

$$f_n^{ij}(r^{ij}) = c_n^{ij} e^{-b_n^{ij} r^{ij}} \sum_{k=0}^{k_{max}} \frac{(b_n^{ij} r^{ij})^k}{k!} \tag{2.5}$$

For the dispersion interactions we set $c_6^{ij} = c_8^{ij} = 1$, $b_6^{ij} = b_8^{ij}$ and $k_{max} = 4$.

For the short range repulsive interaction terms of the potential, deformable oxygen anions and rigid cations are considered. The cation-cation repulsion is sufficiently modeled by the Coulombic term due to the small size of cation. The shape deformations are taken as relatively insignificant for the anion-anion repulsions, which are therefore represented by a simple Born-Mayer exponential functions, but they are substantial in the shell of nearest neighbors, i.e. for the anion-cation repulsion. The expression used here for the short range repulsion is given by

$$\begin{aligned} V^{rep} = \sum_{i\in O, j\in Ca,Mg,Al,Si} & [A^{ij} e^{-a^{ij}\rho^{ij}} + B^{ij} e^{-b^{ij}\rho^{ij}} + \\ & C^{ij} e^{-c^{ij} r^{ij}}] + \sum_{i,j\in O} A^{OO} e^{-a^{OO} r^{ij}} + \\ & \sum_{i\in O} [D(e^{\beta\delta\sigma^i} + e^{-\beta\delta\sigma^i}) + (e^{\zeta^2|\nu^i|^2} - 1) + \\ & (e^{\eta^2|\kappa^i|^2} - 1)], \end{aligned} \tag{2.6}$$

where

$$\rho^{ij} = r^{ij} - \delta\sigma^i - S_\alpha^{(1)} \nu_\alpha^i - S_{\alpha\beta}^{(2)} \kappa_{\alpha\beta}^i, \tag{2.7}$$

and summation of repeated indices is implied. The variable $\delta\sigma^i$ characterizes the deviation of the radius of oxide anion $i$ from its default value, $\{\nu_\alpha^i\}$ are a set of three variables describing the Cartesian components of a dipolar distortion of the ion, and $\{\kappa_{\alpha\beta}^i\}$ are

a set of five independent variables describing the corresponding quadrupolar shape distortions. In Eqn. 2.6, $\mid \kappa \mid^2 = \kappa_{xx}^2 + \kappa_{yy}^2 + \kappa_{zz}^2 + 2(\kappa_{xy}^2 + \kappa_{xz}^2 + \kappa_{yz}^2)$ and $S_\alpha^{(1)} = r_\alpha^{ij}/r^{ij}$ and $S_{\alpha\beta}^{(2)} = 3r_\alpha^{ij}r_\beta^{ij}/r^{ij^2} - \delta_{\alpha\beta}$ are interaction tensors. The last summations include the self-energy terms, representing the energy required to deform the anion charge density, with $\beta$, $\zeta$ and $\eta$ as effective force constants. The extent of each ion's distortion is determined at each molecular dynamics (MD) time-step by energy minimization. Especially for the high pressure phases, the introduction of an additional 'rigid' Born-Mayer-type term in the anion-cation repulsion interaction has proven useful. This extra exponential function ($C^{-+}e^{-c^{-+}r^{ij}}$ in Eqn. 2.6) accounts for the hard core of the anion.

Polarization effects are considered up to the quadrupolar level (Wilson et al., 1996a). Since the ionic polarizabilities of light cations are usually much smaller than those of the anions (Heaton et al., 2006), only oxygen ions are regarded as being polarizable. Further, the oxygen polarizabilities are approximated by constants. The polarization part of the potential including dipolar and quadropolar contributions can be written as

$$\begin{aligned} V^{pol} &= \sum_{i,j\in O}\Bigg((q^i\mu_\alpha^j - q^j\mu_\alpha^i)T_\alpha^{(1)} + (\frac{q^i\theta_{\alpha\beta}^j}{3} + \frac{\theta_{\alpha\beta}^i q^j}{3} - \mu_\alpha^i\mu_\beta^j)T_{\alpha\beta}^{(2)} \\ &\quad + (\frac{\mu_\alpha^i\theta_{\beta\gamma}^j}{3} + \frac{\theta_{\alpha\beta}^i\mu_\gamma^j}{3})T_{\alpha\beta\gamma}^{(3)} + \frac{\theta_{\alpha\beta}^i\theta_{\gamma\delta}^j}{9}T_{\alpha\beta\gamma\delta}^{(4)})\Bigg) \\ &\quad + \sum_{i\in O, j\in Ca,Mg,Al,Si}\left(q^j\mu_\alpha^i[1 - f_D^{ij}(r^{ij})]T_\alpha^{(1)} + \frac{\theta_{\alpha\beta}^i q^j}{3}[1 - f_Q^{ij}(r^{ij})]T_{\alpha\beta}^{(2)}\right) \\ &\quad + \sum_{i\in O}\left(\frac{1}{2\alpha}\mid\vec{\mu}^i\mid^2 + \frac{1}{6C}\theta_{\alpha\beta}^i\theta_{\alpha\beta}^i\right) \end{aligned} \tag{2.8}$$

$\alpha$ and $C$ are the dipole and quadrupole polarizabilities of the anion, respectively. $T_{\alpha\beta\gamma\delta} = \nabla_\alpha\nabla_\beta\nabla_\gamma\nabla_\delta ... \frac{1}{r^{ij}}$ are the multipole interaction tensors (Stone, 1996). $\mu_\alpha^i$ $(\alpha = x, y, z)$ are the Cartesian coordinates of the induced dipole on ion $i$, $\theta_{\alpha\beta}^i$ $(\alpha, \beta = x, y, z)$ are the respective components of the quadrupole tensor. Summation over repeated indices

| | O-O | Ca-O | Mg-O | Al-O | Si-O |
|---|---|---|---|---|---|
| $A^{ij}$ | 1068.0 | 40.168 | 41.439 | 18.149 | 43.277 |
| $a^{ij}$ | 2.6658 | 1.5029 | 1.6588 | 1.4101 | 1.5418 |
| $B^{ij}$ | | 50532. | 59375. | 51319. | 43962. |
| $b^{ij}$ | | 3.5070 | 3.9114 | 3.8406 | 3.9812 |
| $C^{ij}$ | | 6283.5 | 6283.5 | 6283.5 | 6283.5 |
| $c^{ij}$ | | 4.2435 | 4.2435 | 4.2435 | 4.2435 |
| $b_D^{ij}$ | | 2.0261 | 2.2148 | 2.2886 | 2.1250 |
| $c_D^{ij}$ | | 3.9994 | 2.8280 | 2.3836 | 1.5933 |
| $b_Q^{ij}$ | | 1.5297 | 1.9300 | 2.1318 | 1.9566 |
| $c_Q^{ij}$ | | 1.6301 | 1.3317 | 1.2508 | 1.0592 |
| $C_6^{ij}$ | 44.372 | 2.1793 | 2.1793 | 2.1793 | 2.1793 |
| $C_8^{ij}$ | 853.29 | 25.305 | 25.305 | 25.305 | 25.305 |
| $b_{disp}^{ij}$ | 1.4385 | 2.2057 | 2.2057 | 2.2057 | 2.2057 |
| $D$ | 0.49566 | | $\beta$ | 1.2325 | |
| $\zeta$ | 0.89219 | | $\eta$ | 4.3646 | |
| $\alpha$ | 8.7671 | | $C$ | 11.5124 | |

Table 2.1: Parameters in the repulsive and polarization parts of the potential. All values are in atomic units (Jahn and Madden, 2007).

is implied. For the short-range damping of the charge-dipole and charge-quadrupole cation-anion asymptotic functions again Tang-Toennies damping functions (Tang and Toennies, 1984) were used with $k_{max} = 4$ for the dipole ($f_D^{ij}$) and $k_{max} = 6$ for the quadrupole ($f_Q^{ij}$) damping functions. While the parameters $b_D^{ij}$ and $b_Q^{ij}$ determine the range at which the overlap of the charge densities affects the induced multipoles, the parameters $c_D^{ij}$ and $c_Q^{ij}$ determine the strength of the ion response to this effect.

The Aspherical Ion Model (AIM) contains several (seventeen) additional degrees of freedom which describe the state of the electron charge density of the ion. The AIM potential takes into account the compression of the electron density of the anion, and ionic shape deformation and the polarization effect which are very important for many-body system (Madden and Wilson, 2000; Madden et al., 2006). The AIM potential parameters are optimized by reference to *first principles* DFT calculations (Aguado

et al., 2003a). The AIM parameters are obtained by fitting classical forces, stresses and multipoles to the corresponding *ab initio* data. First of all, the polarizable part is optimized by fitting the multipoles only. Secondly, the short-range repulsive terms and the deformation self-energy parameters are optimized by fitting the stress tensors and forces. The parameters for dispersion interactions remain fixed to values of earlier alumina potential since dispersion is not well represented by standard DFT (Jahn et al., 2006). The resulting potential parameters are given in Table 2.1."

This advanced ionic interaction model has been successfully applied to study properties of MgO-$Al_2O_3$ melts (Jahn, 2008). The model has been shown to be accurate and transferable in a wide range of pressures, temperatures and chemical compositions (Jahn and Madden, 2007). It has been used, e.g., to model the structure and properties of pure forsterite melt (Adjaoud et al., 2008, 2011) or high pressure phase transitions in enstatites (Jahn and Martoňák, 2008, 2009; Jahn, 2010).

### 2.1.3 Periodic boundary conditions

Computer simulations using interaction potentials are usually performed on small systems. If we consider a system of 2000 molecules in the simulation box, 900 on the surface. These molecules on the surface experience different forces than the bulk molecules. To avoid such surface effect, and to conserve the composition of simulation cell it is common to apply periodic boundary conditions. It is a very useful technique to make a simulation that consists of only a few hundred atoms behave as if it was infinite in size.

In periodic boundary conditions, the simulation box is replicated throughout space to form an infinite cell. For the simulation, when a molecule moves in the central box, its periodic image in every one of the replicated boxes moves with exactly the same

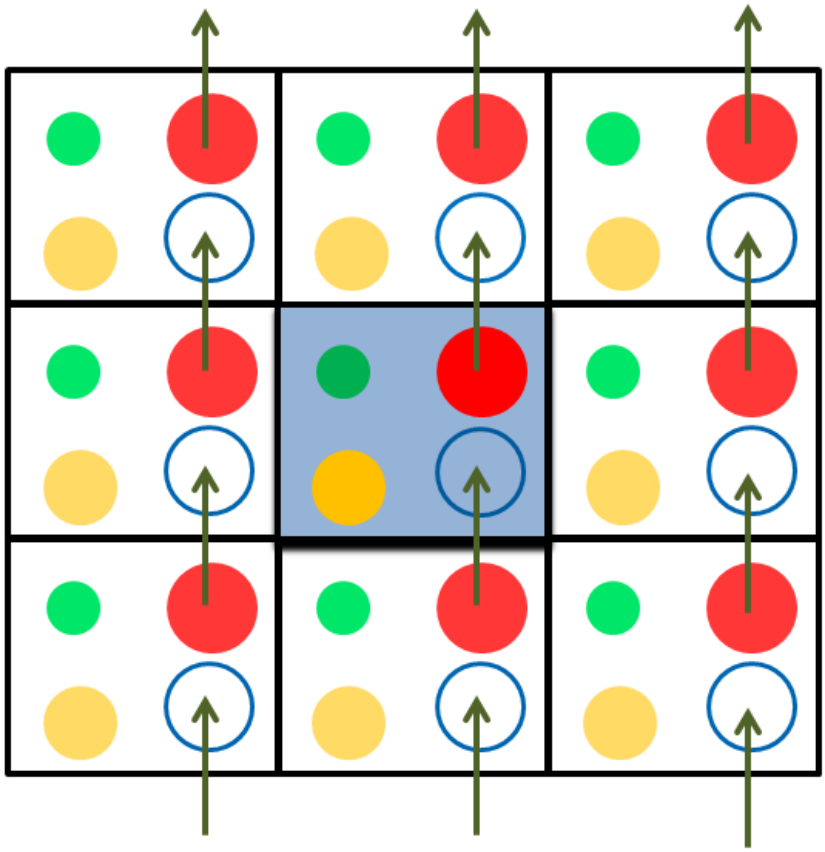

Fig. 2.2: Illustration of two-dimensional periodic boundary conditions consisting of a central simulation cell surrounded by replica system. The straight upward solid arrows indicate an atom leaving the central cell and re-entering on the opposite side.

orientation in exactly the same way. Thus, as a molecule leaves the central box, one of its images will enter through the opposite face. There are no walls at the boundary of the central box. A two-dimensional periodic image of such a system is shown in Figure 2.2. As a particle moves through a boundary, all its corresponding images move across their corresponding boundaries. In this way the number of atoms in the central box and in the entire system is conserved. Therefore the shape of the cells must be space filling.

Since some parts of the interatomic potentials decrease strongly with distance, we can limit the evaluation of the corresponding interactions to a certain distance set by the cut-off radius $r_{cut}$, as shown in figure 2.3. It is important that the sphere with $r$=$r_{cut}$ fits into the simulation cell. In our case, the $r_{cut}$= 14 atomic unit $\simeq$ 7 $\mathring{A}$.

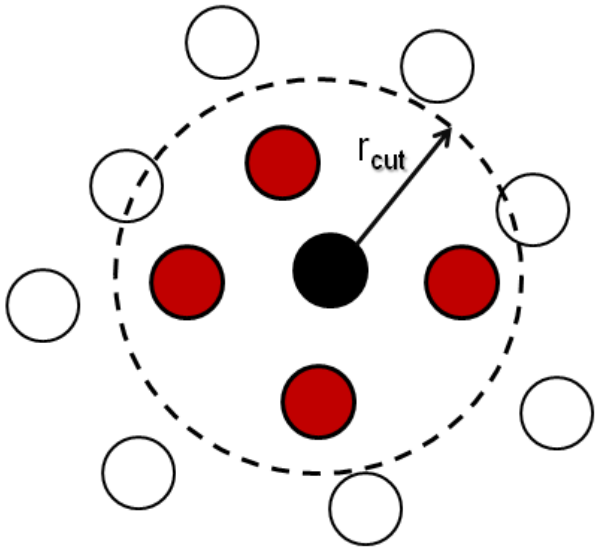


Fig. 2.3: Setting up a cut-off radius in an interatomic potential.

The **minimum image convention** (MIC) method is used by considering only interactions between a particle and the closest periodic image of its neighbors. The electrostatic interactions are more long-ranged than the repulsive terms and they therefore need special treatment which is provided e.g by Ewald summation (Allen and Tildesley, 1987).

### 2.1.4 The Ewald Sum

A long range force is defined as one which falls off no faster than $r^{-d}$ where $d$ is the dimensionality of the system. Typical examples for long range forces are ion-ion (Coulombic interaction) and dipole-dipole potentials which are proportional to $r^{-1}$ and $r^{-3}$, respectively (Allen and Tildesley, 1987; Frenkel and Smit, 2001).

The Ewald sum is a method to calculate efficiently the electrostatic interactions between ions. This is done by splitting the interaction into a screened short range part that is treated in real space and the remaining long range term, which is computed in reciprocal space (Allen and Tildesley, 1987). This technique was originally developed to study the ionic crystals (Ewald, 1921; Madelung, 1918) but it is applicable to any periodic system

of interacting particles. In the AIM MD code the polynomial terms of the potential are long-ranged and treated with Ewald summation.

## 2.2 Molecular Dynamics (MD) Simulation

Molecular dynamics (MD) is a computer simulation technique where the time evolution of a set of interacting atoms is followed by integrating their equations of motion with boundary conditions appropriate for the geometry or symmetry of the system. Statistical mechanics provides the theoretical basis for extracting properties from such molecular dynamics simulations. The dynamic and transport properties can be obtained from time correlation functions. In order to investigate the microscopic behavior of a system from the laws of classical mechanics, MD requires a description of the interaction potential (or force field) as an input.

The quality of the result an MD simulation depends on the accuracy of the description of inter-particle interaction potential. This choice depends very strongly on application. Thus the MD technique acts as a computational microscope. This microscopic information is then converted to the macroscopic observable like pressure, temperature, heat capacity and stress tensor etc. using statistical mechanics.

At the beginning of a MD simulation, the initial positions and momenta of the particles are specified. The particles interact with each other through an interaction potential. Then, Newton's second law of motion is solved (more detail is given in the following part) to describe the motion of particles in the simulation box (tracking out trajectories in space). Finally, physical quantities as a function of particles positions and their momenta are derived. Statistical mechanics is used to average over many of these instantaneous calculations.

### Classical Mechanics

The molecular dynamics simulation is based on Newton's second law or the equation of motion. From the knowledge of the force acting on each atom, it is possible to determine the acceleration of each atom in the system at a given instant. Integration of the equations of motion then yields a trajectory that describes the positions, velocities and accelerations of the particle as they vary with time. From this trajectory, the average values of properties can be calculated. Once the positions and velocities of each atom are known, the state of the system can be predicted at any time in future or past.

Newton's equation of motion for particle 'i' is given by,

$$\vec{F_i} = m_i \frac{d^2\vec{r}_i}{dt^2} = m_i \vec{a}_i \tag{2.9}$$

where $\vec{F}$ is the force exerted on particle i, $m_i$ is its mass and $\vec{a_i}$ is its acceleration.

Acceleration for particle 'i' is defined as

$$\vec{a}_i = \frac{d\vec{v}_i}{dt} = \frac{d^2\vec{r}_i}{dt^2} \tag{2.10}$$

The force can also be expressed as the gradient of the potential energy,

$$\vec{F_i} = -\frac{\partial V}{\partial \vec{r_i}} \tag{2.11}$$

Where $V$ is the potential energy of the system.

$$V = V(\vec{r_1}, \vec{r_2}, ...\vec{r_i}, ...\vec{r_n}) \tag{2.12}$$

Combining equations 2.9 and 2.11 gives

$$-\frac{\partial V}{\partial \vec{r}_i} = m_i \frac{d^2 \vec{r}_i}{dt^2} \tag{2.13}$$

Newton's equation of motion can then relate the derivative of the potential energy to the changes in position as a function of time.

Now, we need to solve the differential equations e. g. 2.9 and 2.13. An analytical solution is difficult and often impossible for a system of more than a few interacting particles, because the force acting on a particle depends on the positions of all other particles and the integration of the equation 2.13 would involve integrating over a sum.

### Integration Algorithms

The potential energy is a function of the atomic positions in three dimensions of all the atoms in the system. Due to the complicated nature of the second order differential equation of motion (equation 2.13), it is solved numerically.

The most important properties of a successful simulation algorithm are as follows:

- The algorithm should conserve energy and momentum.
- It should be stable and give an accurate description of the targeted system.
- The algorithm should be computationally efficient.
- It should permit a long time step $\delta t$ for integration.
- Algorithm should have a simple structure and be easy to program.

The molecular positions, velocities, and accelerations are given at time $t$. We search for positions, velocities and etc. at a later time $t + \delta t$ , to a sufficient degree of accuracy. If the classical trajectory is continuous, then an estimate of the positions, velocities etc.

at time $t + \delta t$ may be obtained by Taylor expansion about time t:

$$r(t + \delta t) = r(t) + v(t)\delta t + \frac{1}{2}a(t)\delta t^2 + \frac{1}{6}b(t)\delta t^3 + ... \tag{2.14}$$

$$v(t + \delta t) = v(t) + a(t)\delta t + \frac{1}{2}b(t)\delta t^2 + ... \tag{2.15}$$

$$a(t + \delta t) = a(t) + b(t)\delta t + ... \tag{2.16}$$

$$b(t + \delta t) = b(t) + .... \tag{2.17}$$

where $r$ and $v$ are the positions and the velocities, $a$ is the accelerations, and $b$ stands for the third time derivative of r.

Numerous numerical algorithms have been developed for integrating the equations of motion e.g. Verlet algorithm, velocity Verlet, Beeman's algorithm, and leap-frog algorithm which we use in our simulations (Allen and Tildesley, 1987).

**The leap-frog algorithm**

In this algorithm, the velocities are first calculated at time $t + \frac{1}{2}\delta t$, these are used to calculate the positions $r$ at time $r(t + \delta t)$.

$$r(t + \delta t) = r(t) + v(t + \frac{1}{2}\delta t)\delta t \tag{2.18}$$

$$v(t + \frac{1}{2}\delta t) = v(t - \frac{1}{2}\delta t) + a(t)\delta t \tag{2.19}$$

The a(t) is taken from the equation 2.9.

In this way, the velocities *leap* over the positions, then the positions *leap* over the velocities (Allen and Tildesley, 1987). The advantage of this algorithm is that the velocities are explicitly calculated and eliminate the problem of adding small and large numbers. However, the disadvantage is that the velocities are not synchronized with

positions. The velocities at time $t$ can be estimated by relationship:

$$v(t) = \frac{1}{2}[v(t - \frac{1}{2}\delta t) + v(t + \frac{1}{2}\delta t)] \tag{2.20}$$

In the next step, thermodynamics is used to control all the variables, like pressure, temperature and energy, in the system (discussed below).

**Thermodynamics**

The connection between microscopic simulations and macroscopic properties is made via *statistical mechanics* which provides the accurate mathematical expressions that relate macroscopic properties to the motion of atoms to the atoms and molecules of the N-body system.

The *thermodynamic state* of a system is usually defined by a small set of variables, for example, the pressure $P$, the temperature $T$, and the number of particles $N$. There are four ensembles which are commonly used (Frenkel and Smit, 2001). In the micro-canonical, or constant-$NVE$ ensemble, the thermodynamic state is characterized by a constant number of atoms, constant volume $V$, and constant energy $E$. This ensemble corresponds to an isolated system. The canonical or constant-$NVT$ ensemble is characterized by a fixed number of atoms $N$, a fixed volume $V$, and a fixed temperature $T$. In the isothermal-isobaric constant-$NPT$ ensemble the number of atoms $N$, temperature $T$, and pressure $P$ are fixed. Finally, the grand canonical ensemble $\mu$VT has a constant chemical potential $\mu$, volume $V$ and temperature $T$. $NVT$ and $NPT$ ensembles are used here (see section 2.4).

**Total Energy**

The total energy is given by,

$$E = \frac{1}{2}\sum_{i=1}^{N} m_i {v_i}^2 + V(r_i) \tag{2.21}$$

which is the sum of kinetic and potential energies.

The absolute temperature T of a system in thermal equilibrium can be computed using Boltzmann's equipartition theorem which states that each degree of freedom of the system has associated with it $1/2k_BT$ of thermal energy on average. where $k_B = 1.38 \times 10^{-23}$ J/K is Boltzmann's constant, and temperature T measured in Kelvins (K).

$$\frac{3}{2}Nk_BT = \langle \frac{1}{2}\sum_{i=1}^{N} m_i {v_i}^2 \rangle \tag{2.22}$$

where $\langle ... \rangle$ denotes a time (ensemble) average. Thus the temperature is determined by the average kinetic energy (Allen and Tildesley, 1987). Each atom has three degrees of freedom (it moves in 3-dimensional space), and there are N atoms in the system.

**Pressure Tensor**

In a fully periodic system of volume V, the pressure tensor for a system of N atoms can be evaluated from

$$P_{\alpha\beta} = \frac{1}{V}(\sum_i p_{i\alpha}p_{i\beta}/m_i + \sum_i r_{i\alpha}f_{i\beta}) \tag{2.23}$$

for ($\alpha \neq \beta$) element of the pressure tensor (Allen and Tildesley, 1987). Where $m_i$ and $p_i$ are the mass and momentum of particle i. The sum involving $r_{i\alpha}$ and $f_{i\beta}$ implies a sum over all the indvidual force contributions $f_{i\beta}$ to the total force on i. Where $\alpha\beta = xy, yz, zx$ of $P_{\alpha\beta}$.

More Explanation about pressure tensor calculation is given in the book by Allen and Tildesley (Allen and Tildesley, 1987).

## 2.3 Non-Equilibrium MD Simulation

Molecular dynamics simulations have become a powerful tool in studying both equilibrium and non-equilibrium atomistic processes in material science. Non-equilibrium molecular dynamics (NEMD) has emerged as a very efficient simulation process to study directly the viscosity of a fluid under the effect of applied shear to the system..

Different approaches are developed for viscosity calculation by using NEMD simulations in the past few years (Ashurst and Hoover, 1975, 1977; Evans and Hoover, 1986; Fuller and Rowley, 1998) and some useful models are also developed for the viscosity calculation of fliuds (Giordano and Russell, 2007; Hui and Zhang, 2007; Giordano et al., 2008). A remarkable progress on NEMD is done by *Hoover* and his coworkers (Hoover, 1993; Evans, 1986; Hoover and Hoover, 2005, 2009).

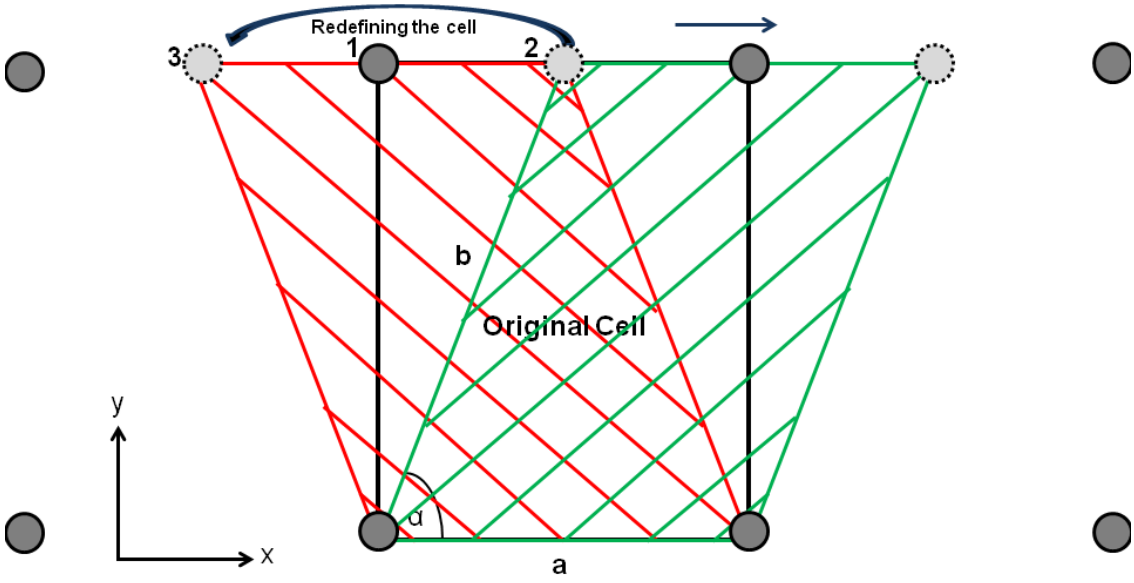


Fig. 2.4: Snapshot of applying shear to the simulation cell, initially the cell is sheared from position 1 to position 2 after n steps. And then the cell is redefined from position 2 to position 3.

Here, we introduce non-equilibrium behavior to our AIM potential with the same periodic boundary conditions using Ewald sum. A constant shear velocity is applied to

the periodically repeated cell in the xy-plane as shown in figure 2.4. In figure 2.4 the black box shows the original cell which is represented by position 1. A constant shear is applied to this cell along x-direction. After many steps, the number of steps which depends on the size of the simulation cell and the shear rate green box with position 2. The upper edge of the cell is displaced by $\Delta x$ ; $\vec{b} = \vec{b} + \Delta x\vec{x}$. If, after n steps, $\Delta x \geq \frac{a}{2}$, the cell vectors are redefined as $\vec{b} = \vec{b} - \vec{a}$ which gives identical cell due to periodic boundary conditions. The redefined cell box is shown as red box with position 3 in Figure 2.4. This redefinition of the cell vectors preserves the volume and the physical properties of the system.

## 2.4 Setup of the Forsterite-Melt Interfaces

The temperature condition of the simulations was chosen to sample the forsterite + liquid two-phase region of the $Mg_2SiO_4-MgSiO_3$ phase diagram shown in Fig. 2.5. The pressure of 1 atmosphere (ambient) is taken. Figure 2.5 is modified according to the system which is studied here. The red circle represents the temperature of our studied system in the phase diagram. And the composition range of all the interfaces A-D lies on the red dashed line which is at 2000 K in the figure.

According to the experimental measurements, the melting temperature of forsterite at ambient pressure is 2163±25 K (Bowen and Andersen, 1914) and enstatite melts incongruently at 1830 K to form a silicate rich melt and forsterite (Lange and Carmichael, 1987). At the conditions of our simulations, $T = 2000$ K and ambient pressure, forsterite coexists with a silicate melt that is slightly enriched in MgO compared to $MgSiO_3$. Starting with a pure $MgSiO_3$ melt, the somewhat different equilibrium melt composition at a given $P-T$ condition is expected to self-adjust in the course of the simulation. Ambient pressure conditions were chosen to allow direct comparison of the obtained transport

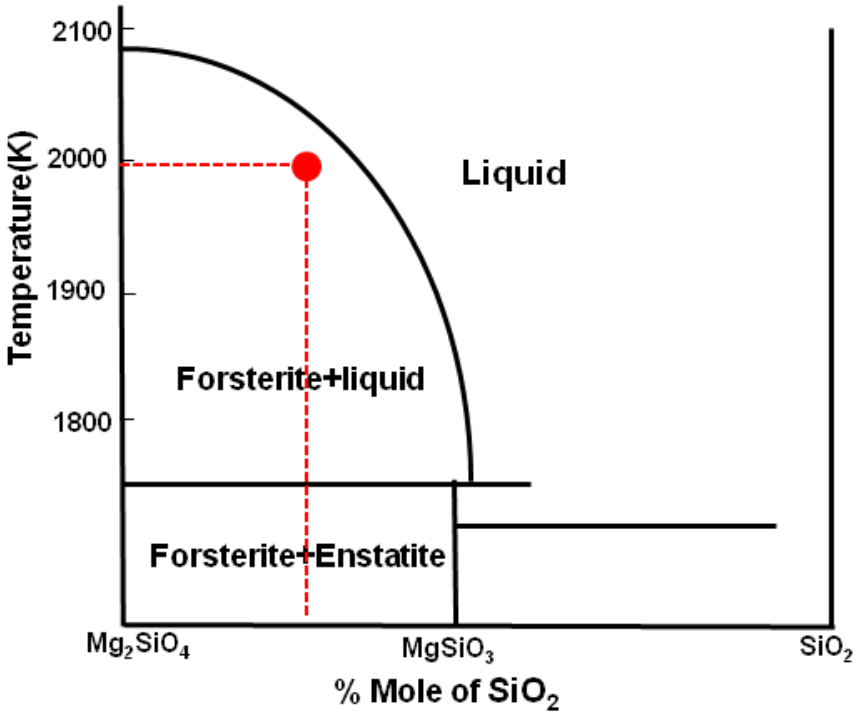


Fig. 2.5: Modified phase diagram (Barth, 1962, page 97) of the system used for this study. The red dotted lines and the circle represents the existence of our system in the phase diagram at 2000 K for ambient pressure.

properties to experimental work on partially molten rocks (e.g. (ten Grotenhuis et al., 2005)).

The simulation cells of the initial silicate melt ($MgSiO_3$) and of the forsterite crystal ($Mg_2SiO_4$) contain a total of 480 ions (96 formula units) and 672 ions (96 formula units), respectively. Solid and melt simulation cells are equilibrated separately. The melt simulation cell is equilibrated for 50 ps in the $NPT$ ensemble (constant number of atoms/ions, pressure and temperature) using an isotropic barostat (Martyna et al., 1994) coupled to a Nosé-Hoover thermostat (Nosé and Klein, 1983). Similarly, the forsterite simulation cell is equilibrated at the same conditions in the $NPT$ ensemble but using an anisotropic barostat keeping the simulation cell orthorhombic. After equilibration, the barostat is switched off and production runs of 250 ps length for the solid and 500 ps

length for the melt are performed in the $NVT$ ensemble (constant volume). The results of both simulations are used as reference to represent the structure and properties of the bulk crystal and the bulk melt.

After separate equilibration of solid and melt, interfaces are constructed between them as follows. First, the crystal cells are rotated to yield three different surface terminations: (010), (100) and (001). Then, four different melt layers are constructed by using 1x1x0.5, 1x1x1, 1x1x2 and 1x1x4 supercells of the melt simulation box. The 1x1x0.5 cell with 240 ions was re-equilibrated after removing half of the ions from the cubic box and reducing the simulation cell length in one dimension. The different melts are subsequently confined between two crystal cells (2×672 ions) leaving a small gap between melt and solid of 0.1 nm to avoid direct ion contacts. To overcome the misfit in the cross-section between melt and crystal, the particle positions in the melt are rescaled in the interfacial plane. Thus, 12 different solid-melt interfaces with three different surface terminations and four different melt thickness layers are obtained. In the following, we refer to interfaces containing initial melt layer thicknesses ($d$) of 0.8 nm, 1.6 nm, 3.3 nm and 6.5 nm as A-, B-, C- and D-interfaces. The total numbers of ions in these supercells are 1584, 1824, 2304 and 3264, respectively.

Fig. 2.6 shows the simulation box (black) of interface C with (010) crystal surface termination containing 2304 total number of atoms.

Two different ranges of pressure and temperature are applied to the system to check the stability of the system. In one case, only pressure is changed from ambient to 10 GPa but temperature is kept same as before, i.e. 2000 K. In second case, both are increased, pressure to 10 GPa and temperature from 2000 K to 2400 K. For these two cases, molecular dynamics simulations are done only with (010) crystal surface termination for all four interfaces. Similarly, all the steps are repeated as done before, system is equilibrated first and then production runs are started.

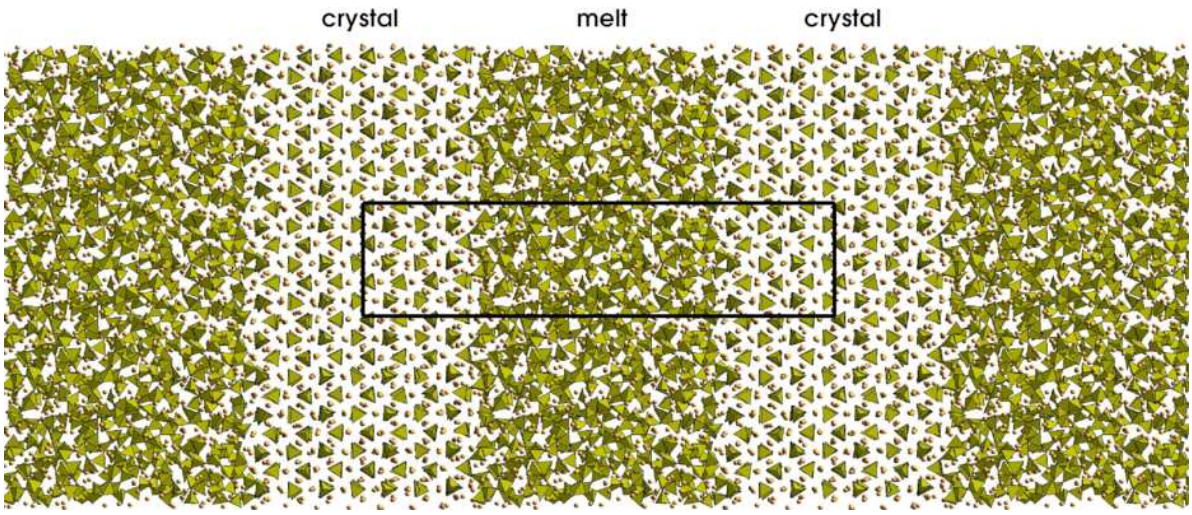


Fig. 2.6: Snapshot from simulation of interface C with (010) crystal surface termination. $SiO_4$ tetrahedral units and Mg ions are shown in polyhedral representation and as balls, respectively. Black lines indicate the simulation box, which is about 7 nm long and periodically repeated in three dimensions. Thus, the model is composed of alternating melt (disordered) and crystal (ordered) layers

## 2.5 Technical Details of the Simulation

All interfaces are equilibrated at ambient pressure and 2000 K for 50 ps in the $NPT$ ensemble. The gaps are closed during equilibration within few starting steps. Due to the different interfacial cross sections of the orthorhombic crystal cell in different orientations, the resulting thickness of the melt layers after equilibration varies slightly between interfaces with different surface terminations but with the same number of melt atoms. After equilibration, production runs of 700 ps length for all interfaces are collected in the $NVT$ ensemble. From the particle trajectories we derive various properties like charge density, cation coordination, connectivity of $SiO_4$ tetrahedra and self-diffusion coefficients. For a detailed analysis of the various properties across the interface, the simulation cell of each interface is divided into layers parallel to the interface.

NEMD simulation is used for the viscosity calculation of our system, again the system is equilibrated for 50 ps in the $NPT$ ensemble (constant number of atoms/ions, pressure

and temperature) using an isotropic barostat (Martyna et al., 1994) coupled to a Nosé-Hoover thermostat (Nosé and Klein, 1983). These calculations are done with positions of the last 700 ps from equilibrium molecular dynamic simulations for all interfaces of (010) orientation only. Different shear rates are applied to the bulk melt and all the interfaces.

Calcium (Ca) is added as impurity to the interface by replacing some Magnesium (Mg) atoms. We directly replace 18 Mg atoms with Ca, as both have same atomic charge. We choose only interface-C with (100) orientation to see the effect of impurity on the system. After adding Ca, the system is again equilibrated for 50 ps and then production runs are started for 600 ps. All the results are compared and discussed in result section (chapter 3).

Before starting all these calculation, we tested the rigid ion model of Matsui (Matsui, 1994), and also the potential used by Guillot (Guillot and Sator, 2007a) for our system. We need a fast and reliable model as we have to deal with thousands of atoms. Using such potential (RIM), increases the computational efficiency for large system and for longer time. The rigid ion model was not useful for our system because it shows unphysical behavior and could not stabilize the interface at the relevant conditions.

Standard deviation ($\sigma$) is calculated over average of 400-700 ps according to the available data to estimate the errors. The mean standard deviation ($\sigma_{mean}$) is obtained from $\sigma$ by using the relation $\sigma_{mean} = \sigma/\sqrt{N}$.

## 2.6 Analysis Tools

The structural and transport properties of the simulated system are analyzed using different programs and functions, which are discussed in this section. To study the

variation of various properties across the interface, all the interfaces are divided into different numbers of layers in the direction perpendicular to the interface. Figure 2.7

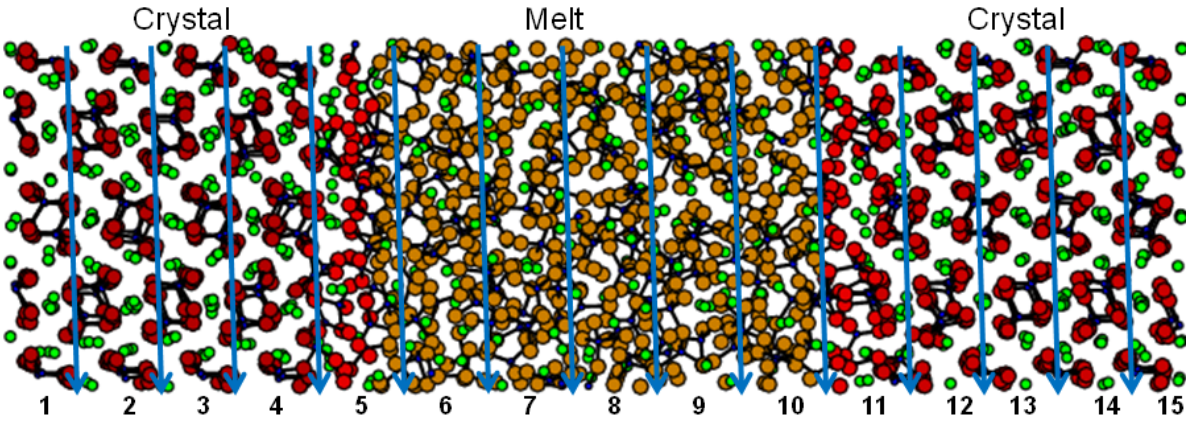


Fig. 2.7: Snapshot from simulation of interface C with (010) crystal surface termination represents the division into layers for analysis.

shows the interface with division into 15 layers. In some cases we divided the interface into as much as 300 layers depending on the size of the interface.

The simulation cells are divided into 100, 150, 200 and 300 for interface A, B, C and D respectively. For the bulk crystal and bulk melt, the simulation cell is divided into 50 layers. For all structural and transport properties, the layer division gives a clear vision to follow the movement of all atoms. Dividing the interfaces into layers, the width of the each layer is kept constant with some increment. The actual number of layers also depends on the specific property of interest.

### 2.6.1 Element Distribution Profiles

The element distribution profiles are obtained by counting all atoms of a given element in a given layer. An average is taken over the whole simulation run and sum them up

For charge distribution $D_c(r)$ profiles we multiply the element distribution profiles by

the respective charge of the ions.

$$D_c(r) = \sum_{i=O,Si,Mg}^{n} \rho(i,r) \times q(i) \tag{2.24}$$

Chemical composition profiles in terms of components MgO and $SiO_2$ are computed for all interfaces and the bulk systems. For each layer, the system is normalized to the total number of MgO and $SiO_2$. The chemical composition profile provides information about the enrichment or depletion of atoms (Mg or Si) across the interface.

The coordination of an atom $i$ was determined by counting the number of atoms of a given species $j$ within a sphere of a given cutoff radius. The cutoff radius is determined by the first minimum in the respective radial distribution function $g_{ij}(r)$ as shown in figure 2.8. From the particle positions, radial distribution functions $g_{ij}(r)$ $[i,j \in (O,Si,Mg)]$ are defined

$$g_{ij}(r) = \frac{N}{\rho N_i N_j} \frac{1}{4\pi r^2} \sum_{\alpha} \sum_{\beta} \langle \delta(r + |\vec{r}_\alpha - \vec{r}_\beta|) \rangle \tag{2.25}$$

The black line on the plot indicates the cutoff radius used for counting the numbers of nearest neighbors of oxygen.

### 2.6.2 Mean Square Displacement

To compute the self-diffusion coefficient, we need to follow the time dependence of the mean square displacement. The mean square displacement is defined as

$$\langle r^2(t) \rangle = \langle |\vec{r}_i(t) - \vec{r}_i(0)|^2 \rangle \tag{2.26}$$

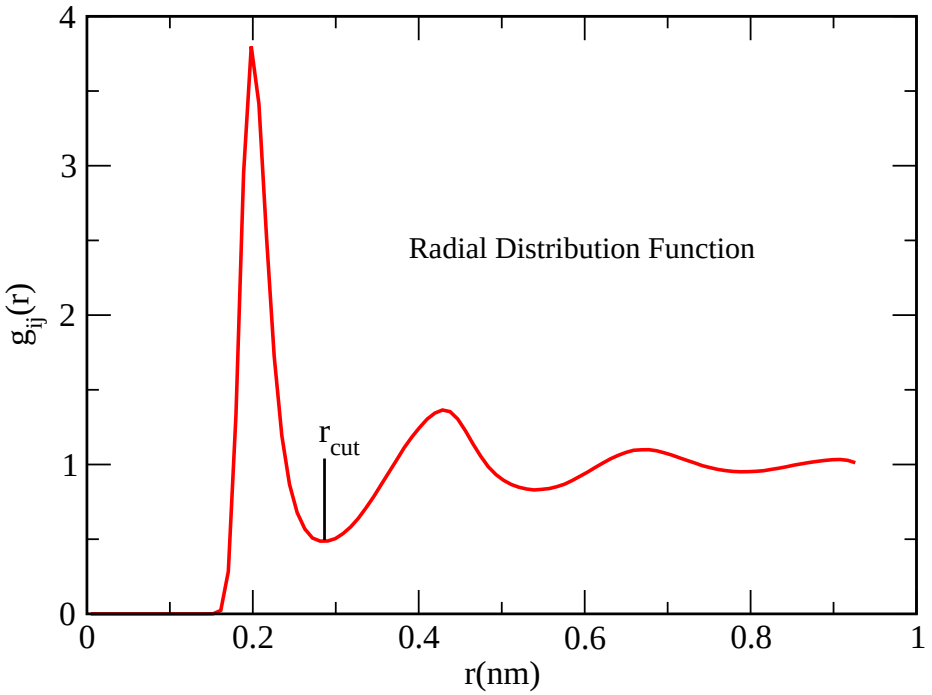


Fig. 2.8: Radial Distribution Function of $MgSiO_3$ melt for O-Mg at 2000 K

$\vec{r}_i(t)$ is the position of particle $i$ at time $t$, and brackets refer to an average over time and ions of the same species. These averages would be computed for each of the $N$ particles in the simulation (Allen and Tildesley, 1987).

The corresponding Einstein relation for the self-diffusion coefficient, valid at long time (Allen and Tildesley, 1987), is

$$D = \lim_{t\to\infty} \frac{< r^2(t) >}{6t} \tag{2.27}$$

or

$$2tD = \frac{1}{3}\langle(\boldsymbol{r}_i(t) - \boldsymbol{r}_i(0))^2\rangle \tag{2.28}$$

Self-diffusion coefficients are calculated from the slope of mean square displacements of ions over a given time $t$ as shown in Fig.2.9.

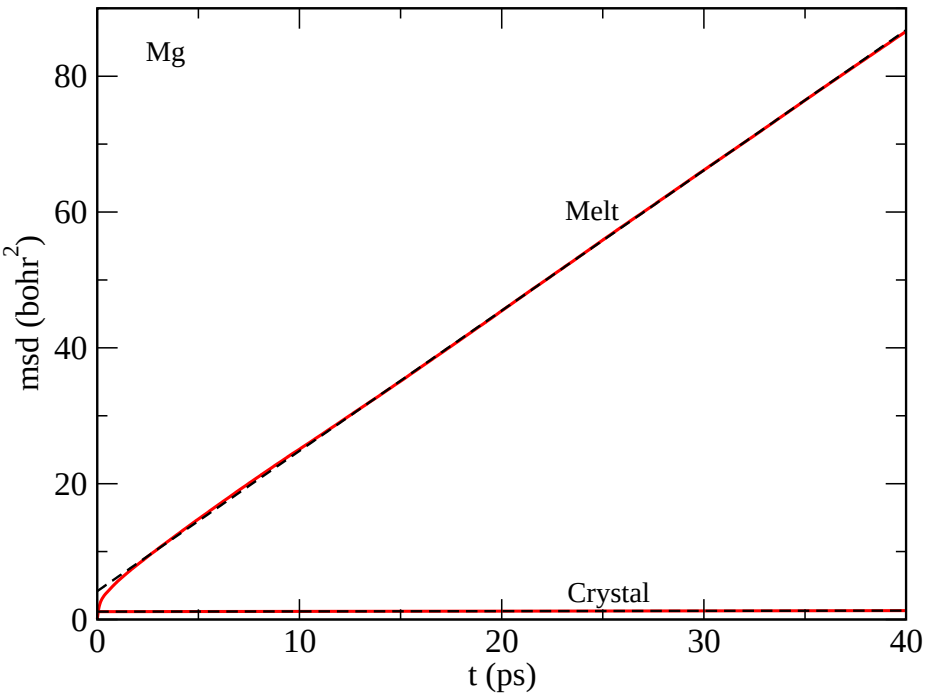


Fig. 2.9: Mean square displacement versus time of Mg from molecular dynamics simulation of forsterite crystal and enstatite melt at 2000 K. Black dashed lines show a linear regression line to the msd in the long time limit.

### 2.6.3 Viscosity

Viscosity is the property of a fluid which describes the resistance to shear deformation. When two layers of a fluid which are a distance $dz$ apart are forced to move one over the other at different velocities, say $u$ and $u + du$, the viscosity together with relative velocity causes a shear stress acting between the fluid layers.

This shear stress is directly proportional to the rate of the change of velocity with respect to $z$. It is denoted by $\sigma_{ij}$ (force per unit area $\frac{F}{A}$).

Mathematically

$$\tau \propto \frac{du}{dz} \tag{2.29}$$

$$\tau = \eta \frac{du}{dz} \tag{2.30}$$

where $\eta$ is the constant of proportionality and is known as the coefficient of viscosity. The velocity gradient $\frac{du}{dz}$ represents the rate of shear strain or rate of shear deformation.

From equation 2.30 we get

$$\eta = \frac{\sigma_{ij}}{\frac{du}{dz}} \tag{2.31}$$

This formula is used to calculate the viscosity for all interfaces and bulk melt at different shear rates. This technique was used by others, e.g. *Naitoh and Ono* (Naitoh and Ono, 1976, 1979; Evans, 1979).

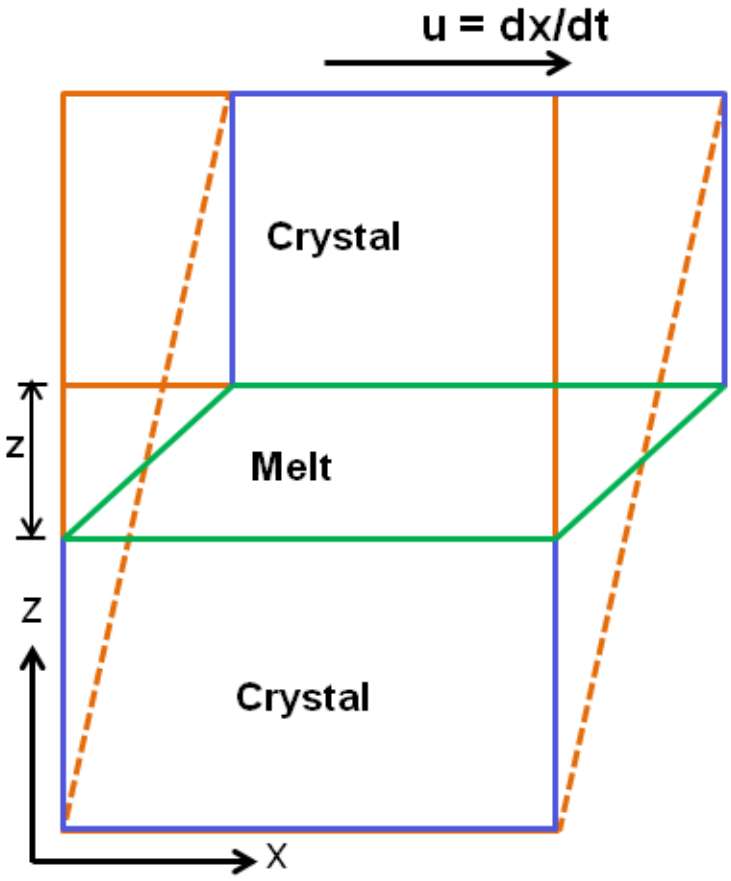


Fig. 2.10: Sketch of applying shear to the interface. Green box represents the effective melt due to shear.

Figure 2.10 shows a sketch to illustrate how the shear is applied to the system. Shear

is applied in $x$-direction on the whole cell. $u$ represents the shear velocity at one end of the simulation cell, whereas the other end remains fixed. The velocity gradient $\frac{du}{dz}$ is calculated to obtain the viscosity from the given respective shear. Considering that shear applied on crystal is zero, we calculated the effective shear rate on melt part only. The shear stress is computed from MD code as described in the book of Allen and Tildesley (Allen and Tildesley, 1987).

Shear viscosity can also be computed from equilibrium MD simulation by using the *Green-Kubo* relation, integrating the autocorrelation function for the off-diagonal elements of the stress tensor which is,

$$\eta = \frac{V}{k_B T} \int_0^\infty dt \langle \sigma_{ij}(t) \sigma_{ij}(0) \rangle \tag{2.32}$$

$V$ is the volume of the system. $\sigma_{ij}$ are the elements of stress tensor. $k_B$ is the Boltzmann constant and $T$ is the temperature. To improve the statistics, an average is performed over five independent elements ($\sigma_{ij}$) to obtain $\eta$: $\sigma_{xy}$, $\sigma_{xz}$, $\sigma_{yz}$, $\sigma_{xx} - \sigma_{yy}$ and $2\sigma_{zz} - \sigma_{xx} - \sigma_{yy}$.

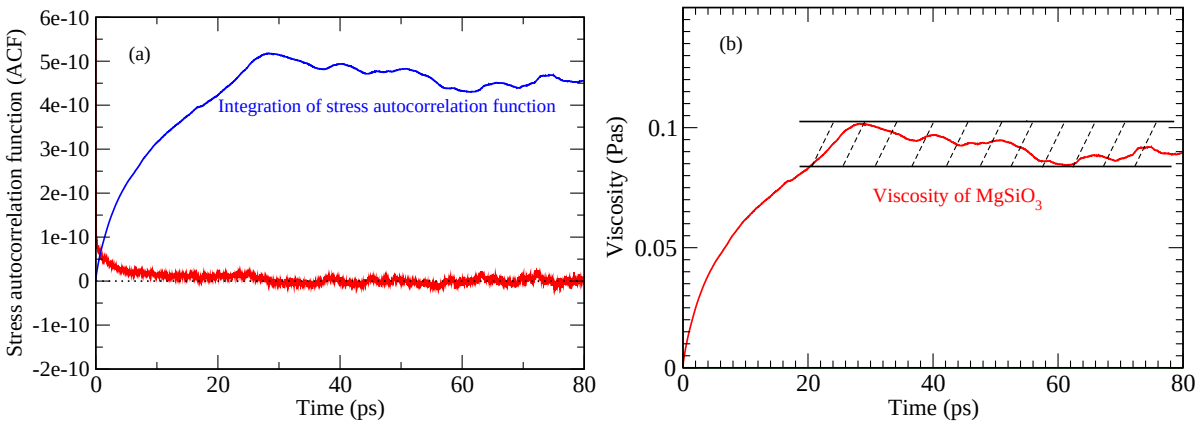


Fig. 2.11: (a) Average of the calculated stress autocorrelation function of $MgSiO_3$ melt with respect to time,(b) Viscosity calculated from stress autocorrelation function of $MgSiO_3$ melt at 2000 $K$. Black horizontal lines with dashed tilted vertical lines represents the error range for the viscosity.

Figure 2.11 illustrates the calculation of melt viscosity by using the *Green-Kubo* relation, i.e. equation (2.31). From the simulation of the melt ($MgSiO_3$), the stress tensor autocorrelation function is plotted versus time and then this function is integrated. Viscosity is calculated by multiplying this integrated function with the constant factor ($\frac{V}{k_B T}$).

# Chapter 3

# Results

## 3.1 Equilibrium Molecular Dynamics Simulation

### 3.1.1 Bulk Properties and Free Crystal Surface

First of all, the results of the bulk systems are presented here. Bulk crystal and bulk melt are first studied separately to have reference properties. In the following part, the structural properties of bulk crystal and bulk melt are discussed in detail. Transport properties of bulk melt, and the elastic properties and the free surface energies of forsterite crystal are investigated.

**∘ Bulk Crystal**

For reference, we first present some structural properties of the bulk forsterite crystal ($Mg_2SiO_4$). As already shown in a previous study (Jahn and Madden, 2007), the AIM potential predicts the forsterite structure in good agreement with experimental data (Fujino et al., 1981). The corresponding lattice constants at ambient conditions are listed in table 3.1.

Table 3.1: Lattice parameters of forsterite from experiment at ambient conditions (Fujino et al., 1981) and AIM simulations at $T = 0$ K (Jahn and Madden, 2007)

| | Experiment | AIM |
|---|---|---|
| $a$ (Å) | 4.75 | 4.73 |
| $b$ (Å) | 10.19 | 10.19 |
| $c$ (Å) | 5.98 | 5.95 |

Similarly, the elastic constants, the thermal expansion at ambient pressure and the volume compression under applied pressure are well reproduced (Jahn and Madden, 2007). Elastic constants of forsterite at ambient conditions are shown in table 3.2.

| | Experimental | AIM |
|---|---|---|
| $c_{11}$ | 329 | 326 |
| $c_{22}$ | 200 | 188 |
| $c_{33}$ | 236 | 232 |
| $c_{44}$ | 67 | 62 |
| $c_{55}$ | 81 | 78 |
| $c_{66}$ | 81 | 82 |
| $c_{12}$ | 67 | 84 |
| $c_{13}$ | 68 | 82 |
| $c_{23}$ | 73 | 80 |

Table 3.2: Elastic constants (GPa) of forsterite at ambient conditions ($T = 0$ for the simulations). AIM predictions (Jahn and Madden, 2007) are compared to experimental data taken from (Fujino et al., 1981) and (Suzuki et al., 1983).

Figure 3.1 shows the atomic and charge distribution profiles of a forsterite crystal along [100]. The total charge distribution (bottom plot of figure 3.1) is obtained by counting all atoms in the respective layer multiplied by their respective charges. This function oscillates around zero due to the imposed charge neutrality of the simulation cell.

Figure 3.2 shows the partial radial distribution functions (RDF's) of the bulk crystal. This function gives the probability of finding a pair of atoms at a distance r. The plotted $g_{ij}(r)$ are at 2000 K. Due to this high temperature the peaks are already very broad. At short distances, which are less than the sum of ionic radii for anion-cation RDF's, g(r) is zero. This is because of strong repulsive forces. The first sharp peak represents a high probability to find two ions e.g. O-Si at the corresponding separation due to the first coordination shell. The radial distribution function then falls and passes through a minimum. The probability of finding two atoms at this minimum separation is small.

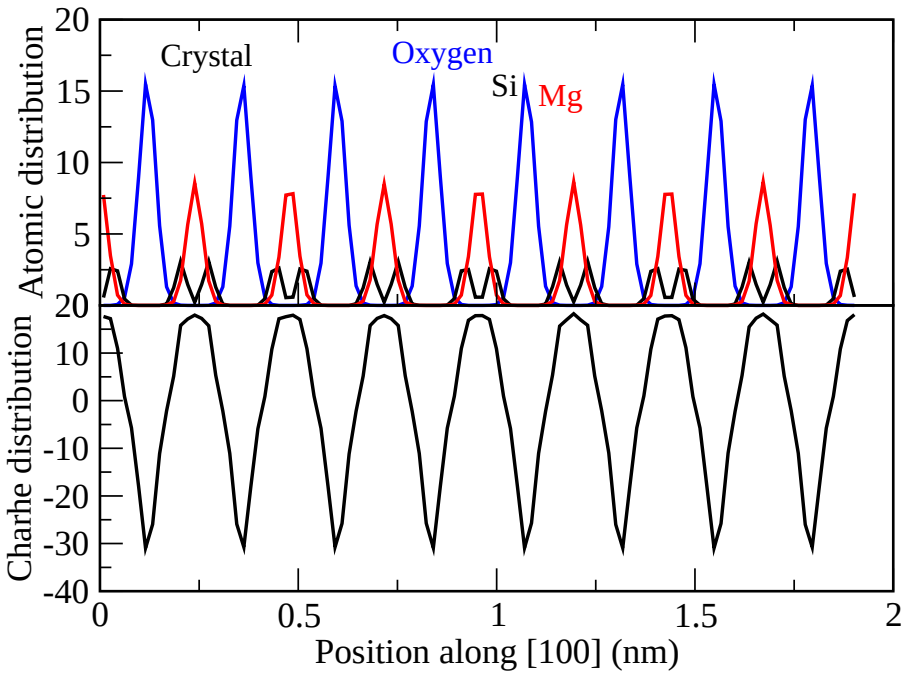


Fig. 3.1: Atomic (top) and charge (bottom) distribution profiles of crystal $Mg_2SiO_4$ along [100].

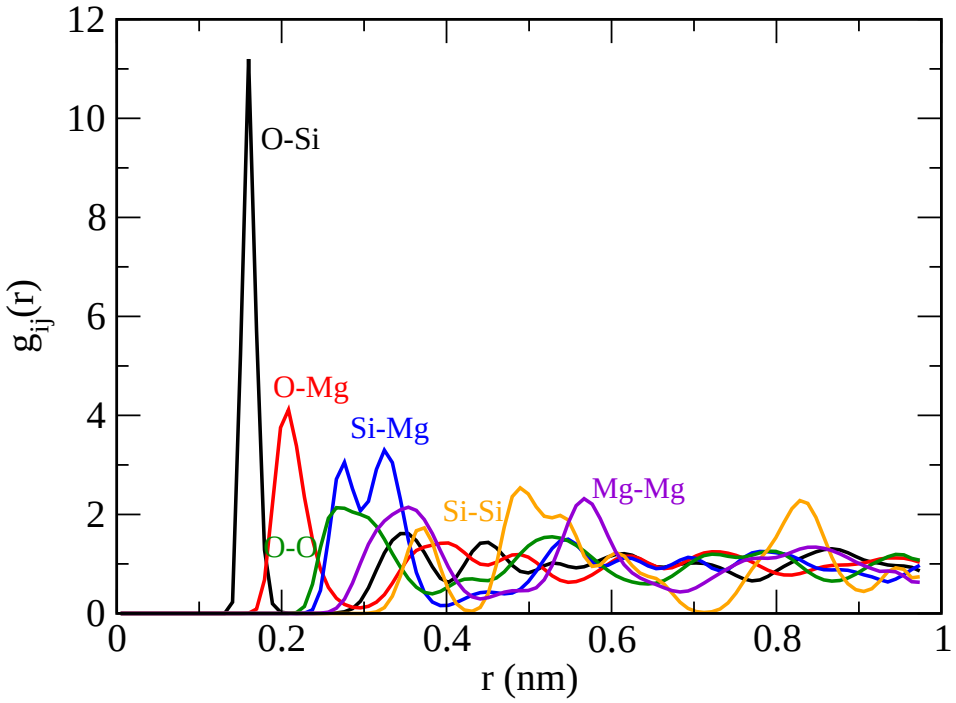


Fig. 3.2: Partial radial distribution functions of forsterite crystal at 2000 K.

The radial distribution functions of the crystal have a large number of peaks up to very long distance as shown in figure 3.2. Eventually, coordination shells increasingly overlap also due to thermal vibrations and the g(r) approaches to one.

Fig. 3.3 shows the resulted mean square displacements of Mg, Si and O for the bulk crystal. Blue dotted lines on all three plots show the zero slope i.e there is no measurable diffusion in the pure crystal. Different values of oxygen, Si and Mg in figure 3.3 are due to different vibrational amplitude between these three species.

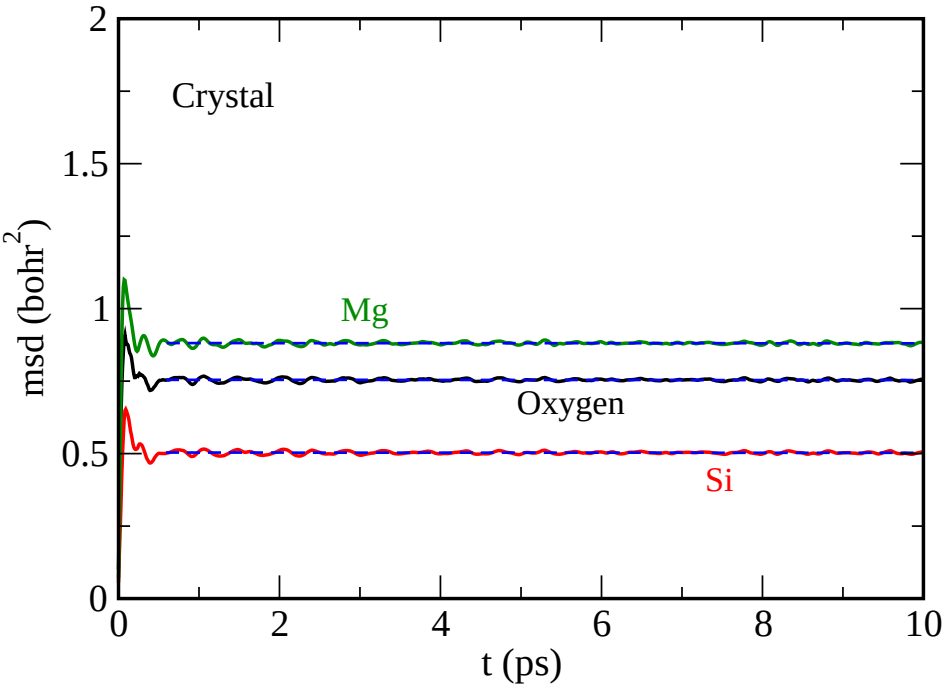


Fig. 3.3: Mean square displacement (msd) versus t (ps) at long time of the crystal at 2000 K. Dashed lines are the regression line which shows that there is no slope.

### ◦ Bulk Melt

Some structural and transport properties are calculated for the bulk melt ($MgSiO_3$) to compare its properties with the melt confined between crystals.

Figure 3.4(a) shows the atomic and charge distribution profiles for the melt. The difference in the structure between melt and crystal can be easily observed from the density

profiles of both as shown in figures 3.1 and 3.4(a). Compared to the crystal there are only small fluctuations in the atomic and charge distribution of the melt which reflects the disordered structure.

The coordination profiles of oxygen by silicon are shown in the figure 3.4(b). Black dotted horizontal lines represents the nominal distribution according to the formula $MgSiO_3$, in which 2/3 of the oxygens are non-bridging and 1/3 are bridging oxygen. There are small fluctuation around these numbers (2/3 and 1/3), due to the simulation cell size effects and the finite simulation time. There are very few free oxygens with no nearest neighbor of Si. Bridging oxygens are defined as having two nearest neighbors of silicon, whereas non-bridging oxygen have only one.

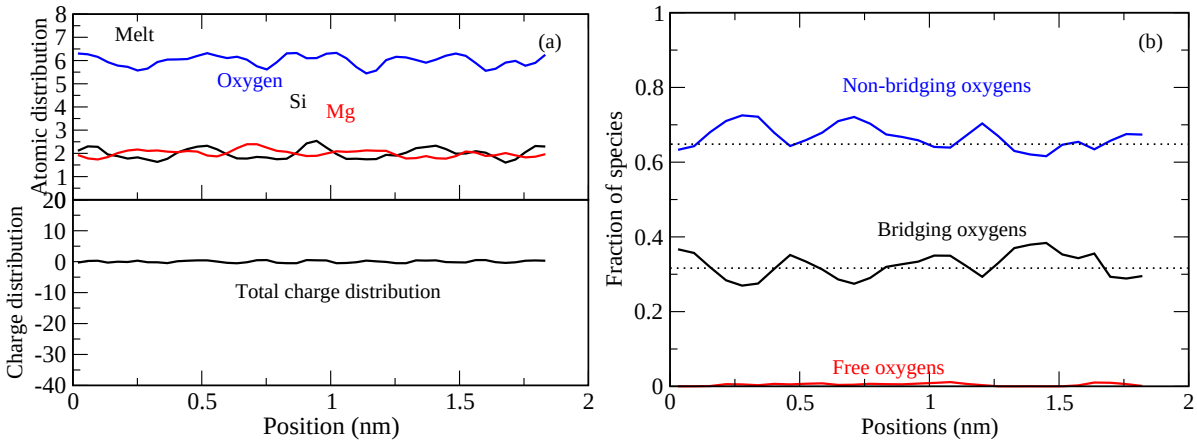


Fig. 3.4: (a) Atomic (top) and charge (bottom) distribution profiles of $MgSiO_3$ melt at 2000 K. (b) Fractional distribution of oxygen coordinations by silicon as a function of position for $MgSiO_3$ melt.

The partial radial distribution functions of $MgSiO_3$ melt, with a small number of peaks at short distances, is shown in figure 3.5. By comparing the partial RDF's of the crystal and the melt (see figures 3.2 and 3.5), it is clear that crystal has a larger number of peaks up to longer distance then the melt.

Self-diffusion coefficients of all three species (Mg,Si,O) for bulk melt ($MgSiO_3$) are obtained from the respective mean square displacements (as discussed in chapter 2). They

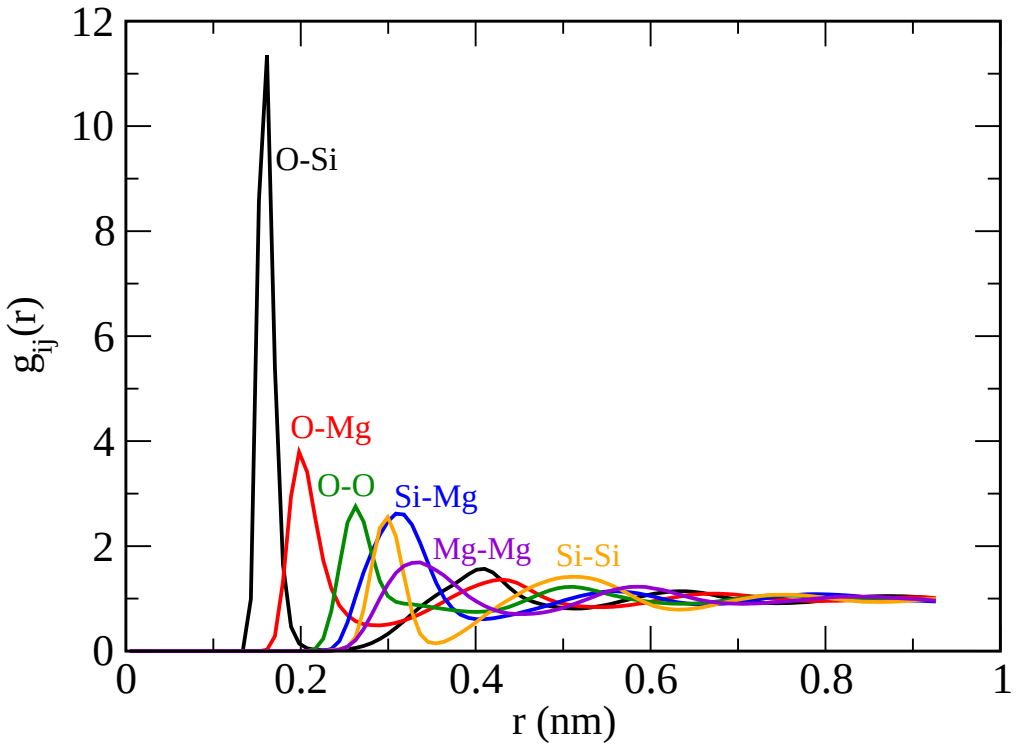


Fig. 3.5: Partial radial distribution function of $MgSiO_3$ melt at 2000 K.

are averaged over 600 ps in six intervals of 100 ps. The data in table 3.3 is for cubic bulk melt with simulation cell length 1.75 nm. This corresponds to the thickness of melt in interface B. Later we double this melt ($2 \times 1 \times 1$ supercell) in one direction to increase the melt thickness for the interface C and use a $4 \times 1 \times 1$ supercell for interface D. The Mg self-diffusion coefficient is about four times larger than that of oxygen and 6-7 times larger than that of Si as given in table 3.3 for cubic melt.

Table 3.3: Self diffusion coefficients ($\times 10^{-6}$cm$^2$/s) of the three elements (O, Si, Mg) of bulk melt (Averaged over 600 ps).

| Bulk-melt $d^{tot}$ (nm) | O | Si | Mg |
|---|---|---|---|
| | diffusion | | |
| 1.75 | 2.4(2) | 1.5(2) | 9.9(4) |

Fig. 3.6 shows the resulting mean square displacements of Mg, Si and O drawn for $MgSiO_3$ melt from the simulation of bulk system. Blue dotted lines on the plot show

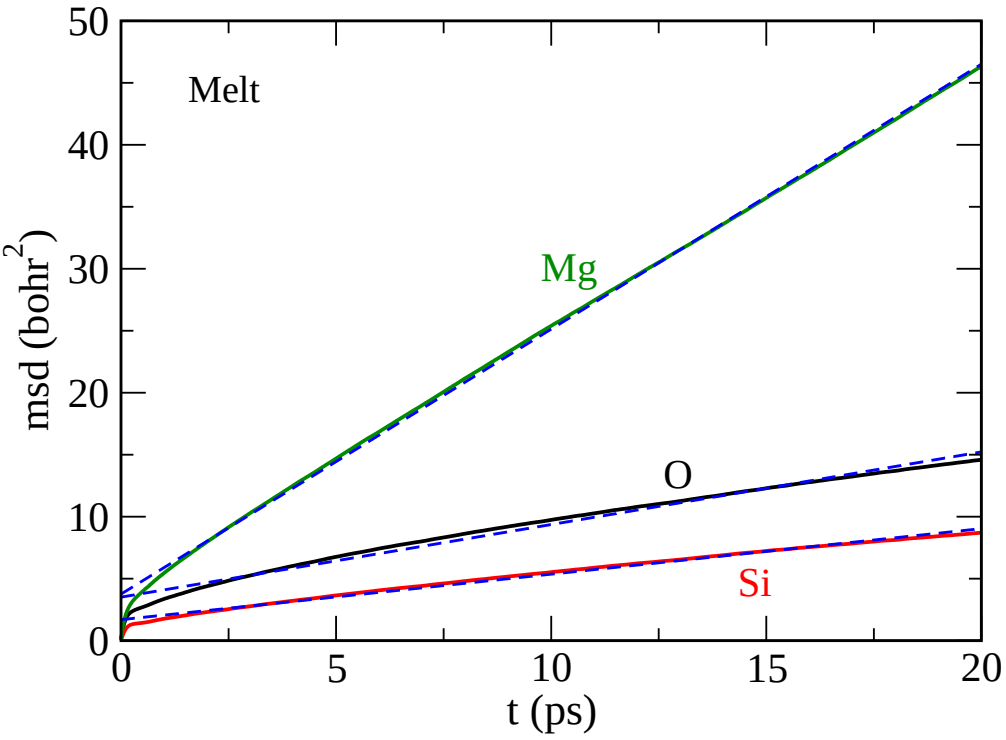


Fig. 3.6: Mean square displacement versus time of Mg, Si and O in $MgSiO_3$ melt at 2000 K. Dashed lines show the linear regression to the msd of each atom.

linear regression lines from which the self-diffusion coefficients are calculated. In case of melt, the mean square displacement increases linearly as $t$ increases for all species (O, Si, Mg). The difference between the mean square displacements of the melt and the crystal is clear by comparing the two figures for crystal and melt 3.3 and 3.6 respectively.

The viscosity of $MgSiO_3$ melt is calculated from EMD by using the *Green-Kubo* relation as defined in section 2.7.2. Table 3.4 represents the viscosity data of two different simulation cells. One is cubic melt ($1 \times 1 \times 1$) with simulation cell length of 1.75 nm. The other is $2 \times 1 \times 1$ supercell of the melt with simulation cell length of 3.50 nm. The viscosity of the cubic melt of cell length 1.75 nm is three time higher than that of larger supercell of cell length of 3.50 nm as given in the table 3.4.

Table 3.4: Viscosity of $MgSiO_3$ melt calculated from equilibrium MD for melt of different thickness (averaged over 400 ps).

| Bulk Melt | |
|---|---|
| Thickness $d^{tot}$ (nm) | Viscosity (Pas) |
| 1.75 | 0.08(2) |
| 3.50 | 0.05(2) |

• **Free Crystal Surface**

The free surface energies of three surfaces (100), (010) and (001) of forsterite were calculated. This is done by cutting the crystal in the plane of interest and adding a thick vacuum layer between the two half-crystals. In the next step, the atomic positions are allowed to relax while keeping the simulation cell parameters constant.

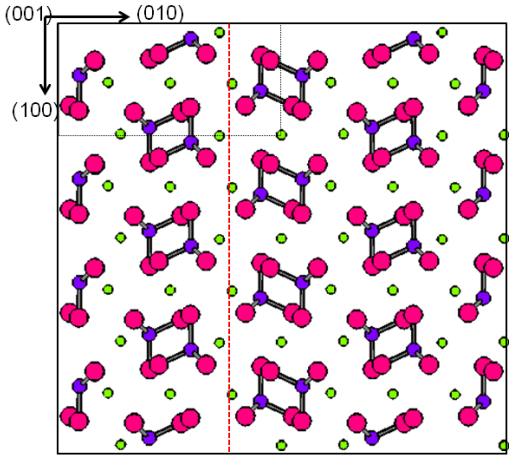


Fig. 3.7: Structure of the original forsterite crystal when dipole is not zero. The black dotted box represents the unit cell and the red dotted line shows the point where the crystal is cut.

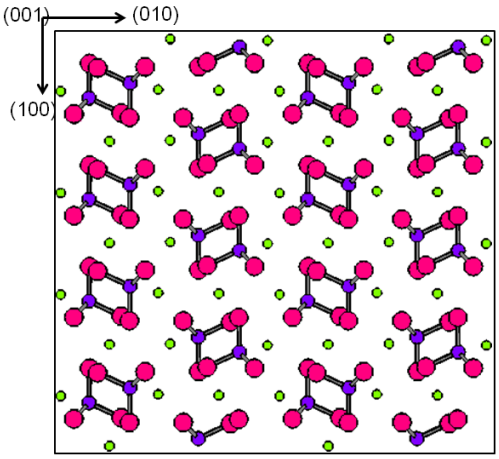


Fig. 3.8: Structure of the forsterite crystal after shifting the origin to obtain a zero dipole perpendicular to the (010) surface. (Green=Mg, Purple=Si, Pink=O)

There is one condition to calculate the free surface energy, which is that the dipole perpendicular to that surface should be zero in the repeat unit, because such a dipole in a periodic cell lead to a divergent surface energy (Bertaut, 1958). As an example Fig. 3.7 shows structure of forsterite along [001] as taken from the crystal structure

database. The forsterite supercell contains 672 atoms with 384 oxygen, 96 Si and 192 Mg.

In this original cell, the dipole is not zero perpendicular to surface (010). After cutting the surface in a different plane by keeping all tetrahedra intact, the simulation cell has a zero dipole (see figure 3.8). A procedure for cutting surfaces and making dipoles zero for forsterite is very well explained by *Watson et al.* (Watson et al., 1997). The relaxed cell with vacuum is shown in figure 3.9. The surface terminations and the relaxation process are similar to the those used by *Watson et al.* [1997].

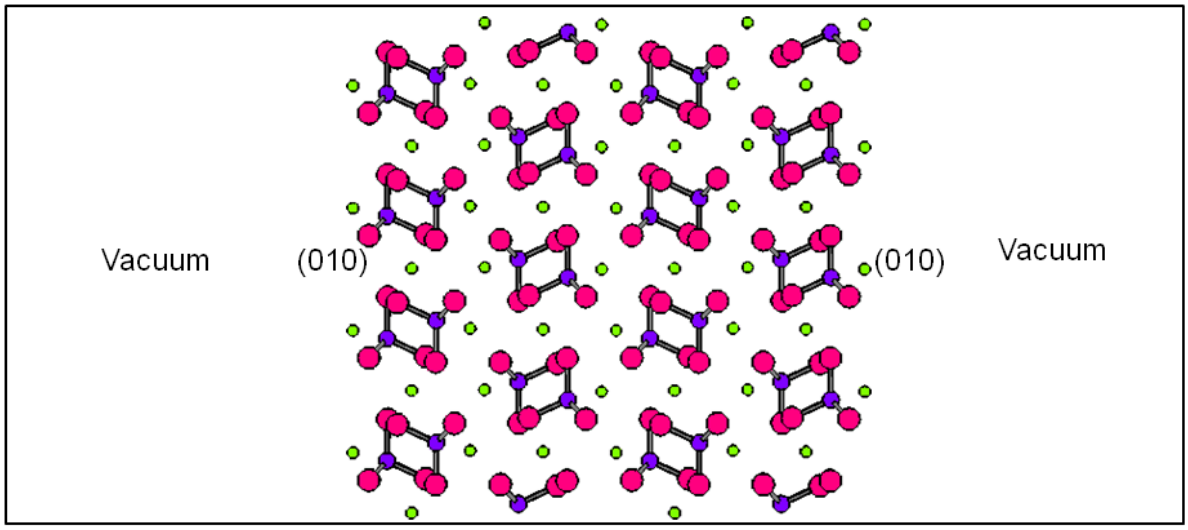


Fig. 3.9: Snapshot of relaxed forsterite crystal run with vacuum. Green=Mg, Purple=Si, Pink=O

The surface energy is defined as the energy per unit area, and formula for calculating the free surface energy is,

$$\gamma = \frac{E_S - E_B}{A} \tag{3.1}$$

where $E_S$ is the energy of the relaxed surface calculation, $E_B$ refers to the energy of the bulk system with the same number of ions, and A is the surface area. In table 3.5, the surface energies obtained from the AIM potential are compared to the results of the previous simulation study by *Watson et al.* [1997] using a rigid ion model. Despite

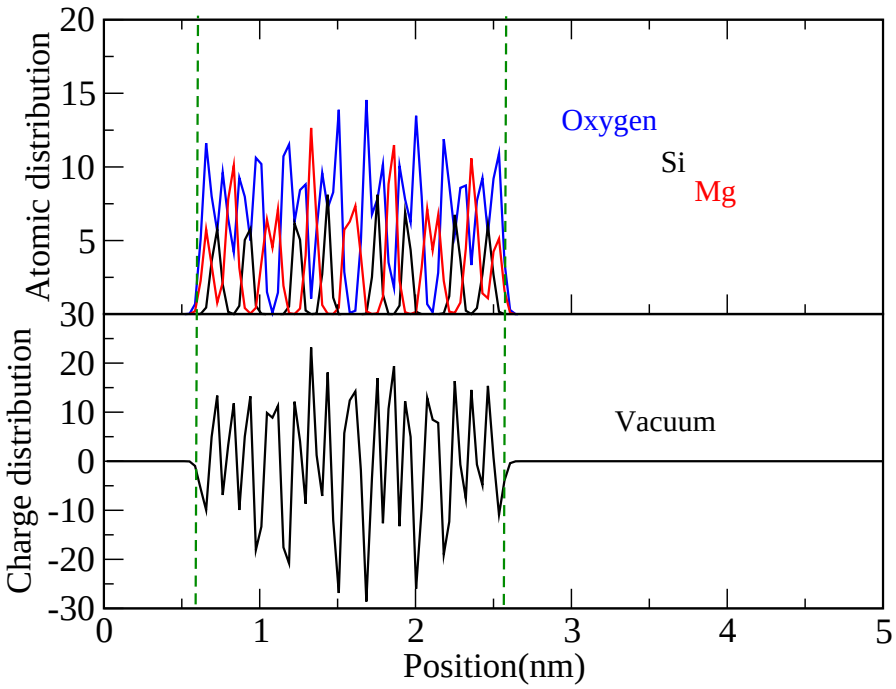


Fig. 3.10: Average atomic (upper graph) and charge (lower graph) distribution profiles of the relaxed free (010) surface of forsterite.

Table 3.5: Free surface energies (in $J/m^2$) of forsterite calculated for three surfaces by AIM and a rigid ion model (Watson et al., 1997).

| Surface | Present study | (Watson et al., 1997) |
|---|---|---|
| (100) | 2.21 | 2.02 |
| (010) | 1.27 | 1.28 |
| (001) | 1.89 | 1.61 |

relative differences of up to about 20% in the surface energies due to the different interaction potentials, both models agree in that the most stable surface is (010) because it has the lowest surface energy. The (100) surface is somewhat less stable than the (001) surface. The different surface energies affect the structural and transport properties as will be discussed in next section.

Fig. 3.10 represents the atomic and charge distributions of the relaxed free (010) surface, after relaxation by molecular dynamics simulations for 10 ps. Strong oscillations are observed due to crystalline order and some small variation close to the surface due to

the atomic relaxation.

### 3.1.2 Structure and Chemical Composition of the Interfaces with (010) Crystal Surface Termination

Interfacial properties are divided into two parts, the structural and the transport properties. In this section structural properties, like charge densities, cation coordinations and chemical compositions of the interfaces with (010) crystal surface termination are presented. The structural properties of all four (A, B, C and D) interfaces with different melt thickness are investigated. In the next section (3.1.3) the effect of surface termination on the structural properties is studied by comparison of the results for the (010) surface to those of (100) and (001) surfaces. Transport properties such as self diffusion coefficients are derived in section 3.1.4.

**• Charge Density Profiles**

Variations of the structure across the interfaces may be represented by the charge and the atomic distribution profiles. As an example, the distribution of the different elements (Mg, Si and O) across interface A, B, C and D with (010) crystal surface termination is shown in the upper upper part of each graph of Fig. 3.11. All profiles shown are results averaged over the total production run of 700 ps. The spacial resolution after dividing the simulation cell into 200 layers for interface C is about 0.04 nm. Green vertical lines represent the position of the original interface.

The total charge distributions are shown in the lower parts of each graph of Fig. 3.11. These functions oscillate around zero due to charge neutrality of the whole simulation cell. The strong oscillations in the crystal part on both sides of all distribution profiles for all interfaces are due to the periodic crystal structure. A relatively strong solid-like charge ordering is also observed in the first melt layers close to the mineral-melt

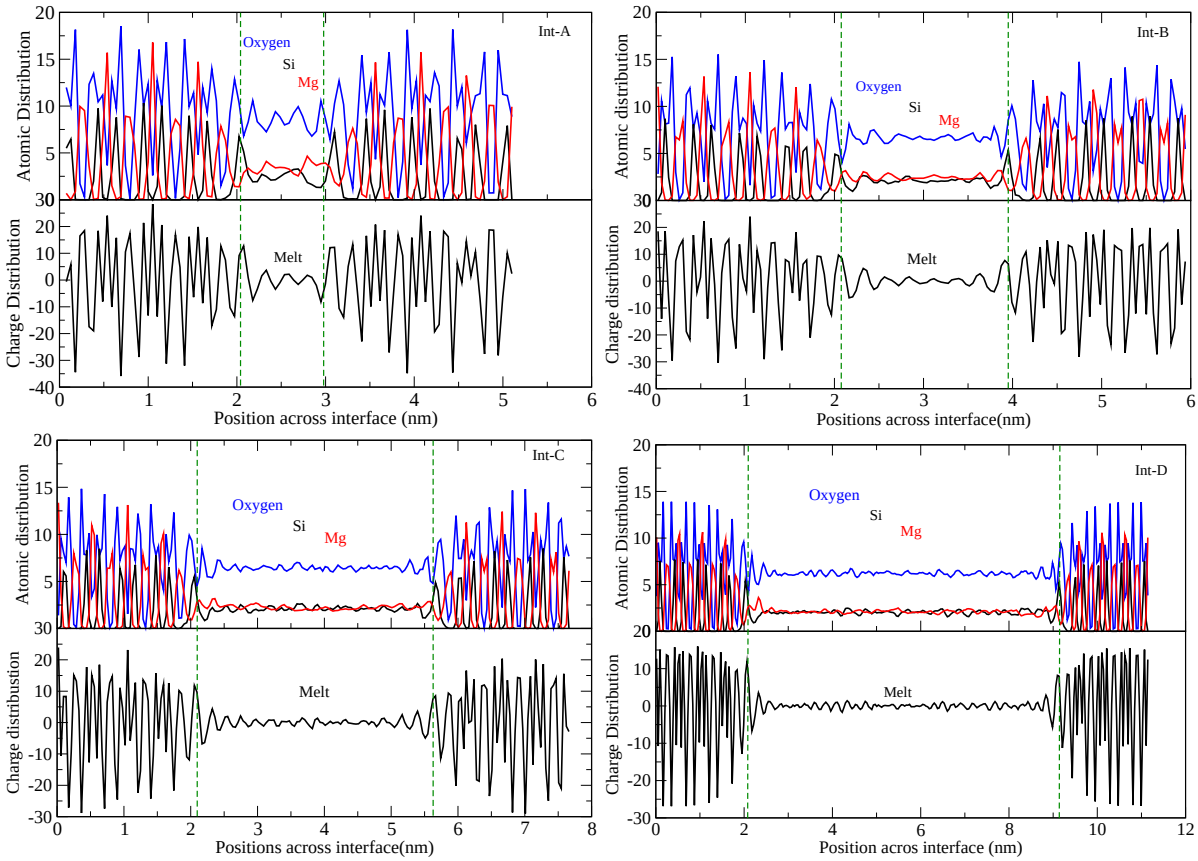


Fig. 3.11: Average atomic (upper graph) and charge (lower graph) distribution profiles across all the interfaces of different melt thickness (A, B, C and D) with (010) crystal surface termination.

interface. In the middle of the melt, very small peaks are observed.

The effect of the melt on the crystal surfaces is apparent from the comparison of the interfacial element and charge distribution profiles (Fig. 3.11) with the corresponding profiles of the free surface, i.e. the crystal surface in contact with vacuum (Fig. 3.10). The latter show much less reconstruction or distortions from the bulk structure close to the interface than the crystal surfaces in contact with the melt.

The atomic and charge distribution functions suggest an interfacial width with strong deviations from the bulk behavior of about 1-2 nm. However, there are still small oscillations even in the central part of the melt, which is due to the strong effect of the

interface on the melt.

Comparing the four diagrams of Fig. 3.11 for the different interfaces, a strong effect of melt thickness on the structure is observed. In the case of interface A, the effect of the crystal (on the melt) is most pronounced. Due to the confinement effect, there are sharp peaks in the central part. As the melt thickness increases, the effect of the crystal on melt is reduced.

• **Chemical Composition**

On the atomic scale, wetting of the crystal surface by the silicate melt leads to chemical heterogeneities in the interfacial region. For all interfaces with (010) crystal orientation, the simulation cells are divided into 80, 100, 120 and 160 layers of A, B, C and D respectively.

Their respective chemical composition of each layer in terms of MgO and $SiO_2$ components are shown in Fig. 3.12 for all four interfaces from A-D. The immediate contact between crystal and melt is characterized by strong compositional fluctuations.

The atomic layers of the crystal close to the interface are somewhat enriched and the average melt composition is slightly depleted in $SiO_2$ component in all interfaces of different melt thickness. As mentioned earlier (see figure 2.5), the phase diagram suggests a MgO mole fraction above 0.5 for the melt under the $P-T$ conditions studied here, which seems to be consistent with the simulation results. The horizontal line on each plot represents the the original $MgSiO_3$ melt composition.

Strong fluctuations are observed across interface-A in the interfacial region as well as in the center of the melt. The fluctuations are decreasing as the melt thickness increases (A to D), similarly as in case of charge and atomic distribution profiles. For interface-D the fluctuations in the center of the melt are already small and probably more due to statistical fluctuations than to interfacial effect ( more detail on this effect is explained

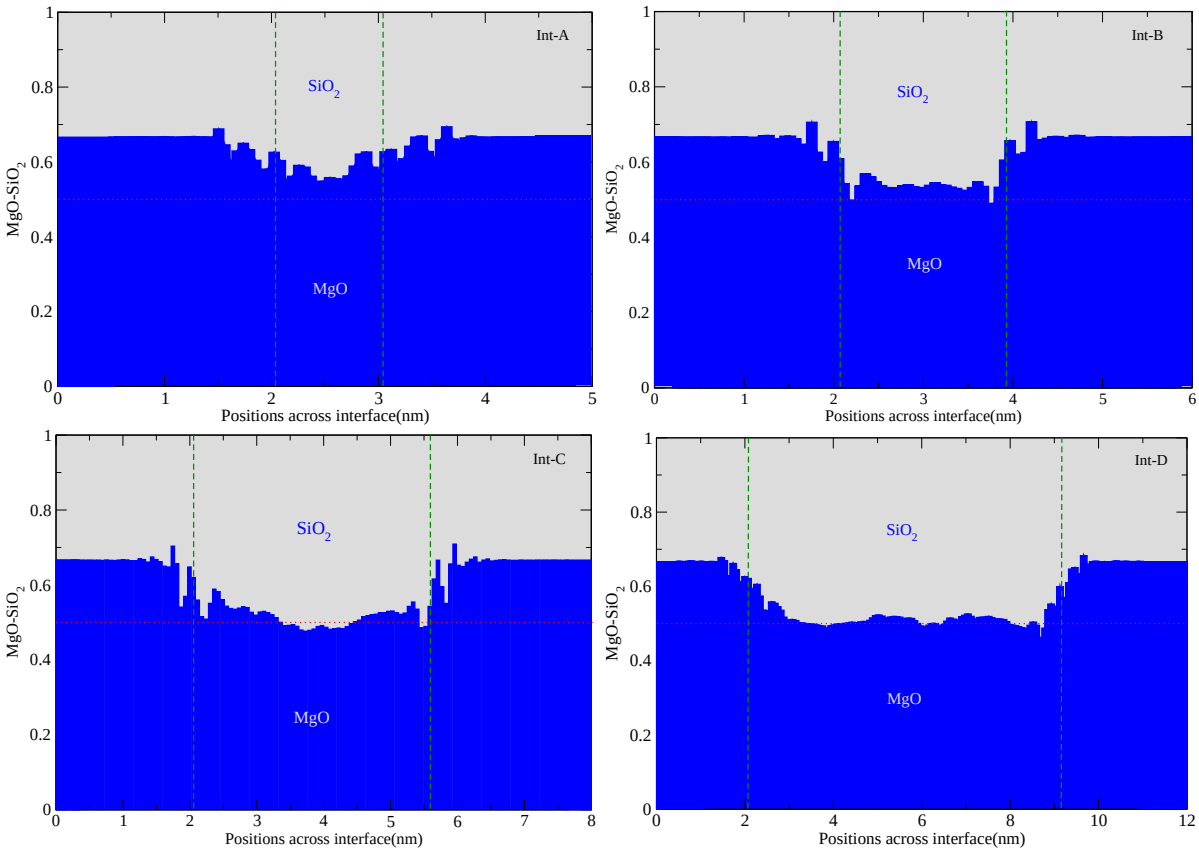


Fig. 3.12: Chemical composition across all interfaces with (010) crystal orientation in terms of MgO and $SiO_2$ components. The horizontal dotted line indicates $MgSiO_3$ composition.

in section 4.3 ).

**• Coordination**

The coordination of an atom $i$ was determined by counting all atoms of a given species $j$ within a sphere of a cutoff radius. The latter is defined by the first minimum in the respective radial distribution function $g_{ij}(r)$. Again all the interfaces are divided into layers like density and composition profiles, its 80, 100, 120 and 250 for interface A, B, C and D respectively. The coordination profiles of oxygen by silicon are shown in Fig. 3.13 for all interfaces from A to D with (010) crystal surface termination.

Bridging oxygens are defined as having two nearest neighbors of silicon, whereas non-

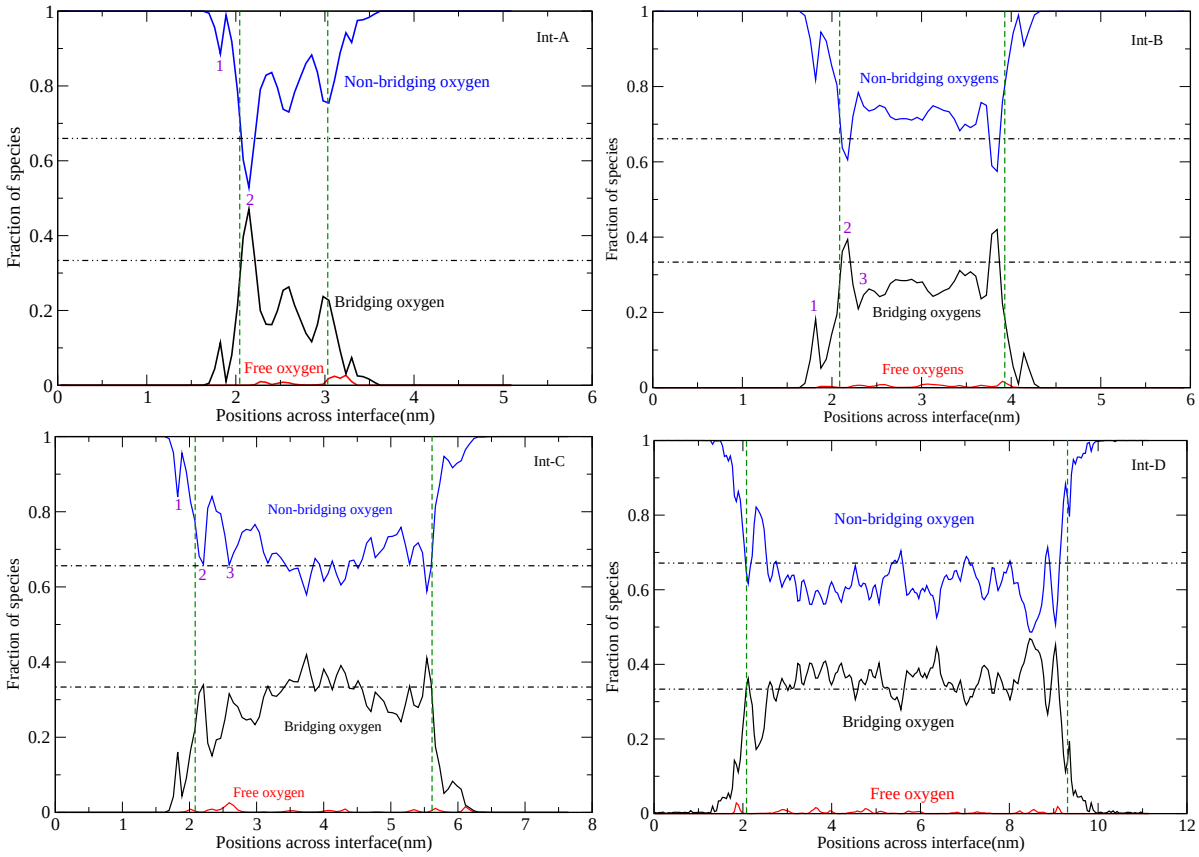


Fig. 3.13: Fractional distribution of oxygen coordinations by silicon for all four interfaces (A-D) with (010) crystal surface termination as a function of position across interface.

bridging oxygens have only one. There are also a few free oxygens with no nearest neighbor Si. Horizontal lines represent the nominal distribution according to the formula $MgSiO_3$, in which 2/3 of the oxygens are non-bridging and 1/3 are bridging oxygens. The olivine crystal ($Mg_2SiO_4$) has only non-bridging oxygens, which can be seen in the crystal part of all plots Fig. 3.13.

All interfaces show a similar behavior at the interfacial region with a small peak in the crystal which is marked by 1 in the diagram, then a minimum and a second peak (2) just in the liquid. There may be a third peak (3) but then the distribution become more random. Interface-A has strong peaks and the central melt part does not cross the black horizontal lines which are representing the nominal distribution.

### 3.1.3 Effect of Crystal Surface Termination on the Structure of the Interface

As described earlier, three types of crystal surface terminations of forsterite are used to construct interfaces of different melt thickness. By looking at the structure of all interfaces and their properties, we observe different behavior due to the surface terminations. This relative difference shows up in the density and coordination profiles as illustrated in figure 3.14.

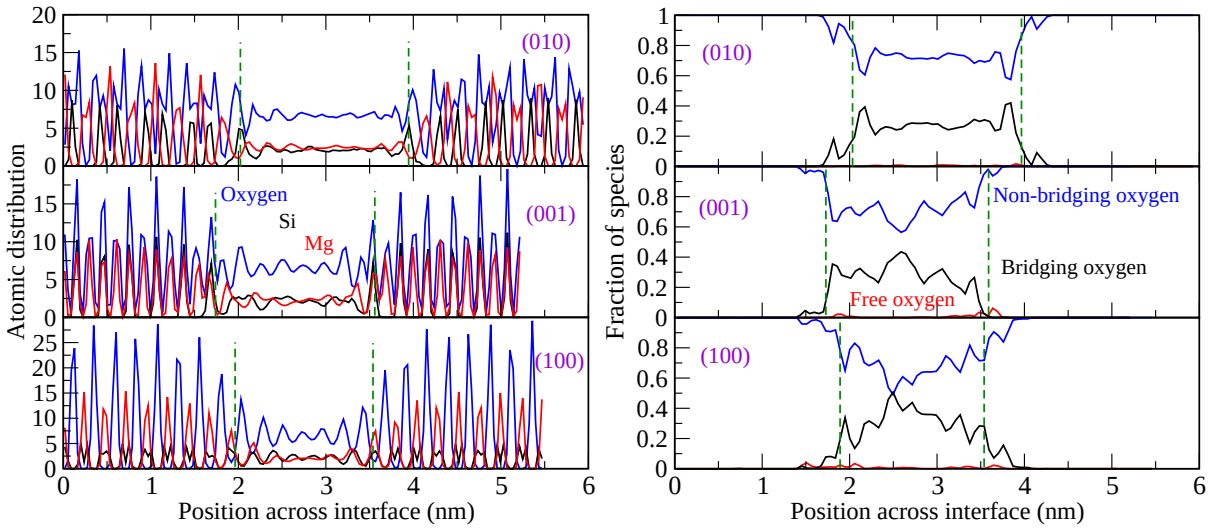


Fig. 3.14: Atomic density profiles (left) and coordination profiles (right) of interface-B for all three crystal orientations. Green vertical lines represents the position of original interface.

The atomic distribution profile for (010) orientation has less fluctuations in the melt region and is less structured in the interfacial region. The other two interfaces with (001) and (100) surface terminations have strong fluctuations in the interfacial region and also some peaks in the center of the melt. Similarly, in the coordination profile of the (100) and (001) interfaces fluctuations in the whole are much stronger as compared to the (010) interfaces. The small difference in the melt thickness and the variation in simulation cell lengths between different crystal surface terminations for the same

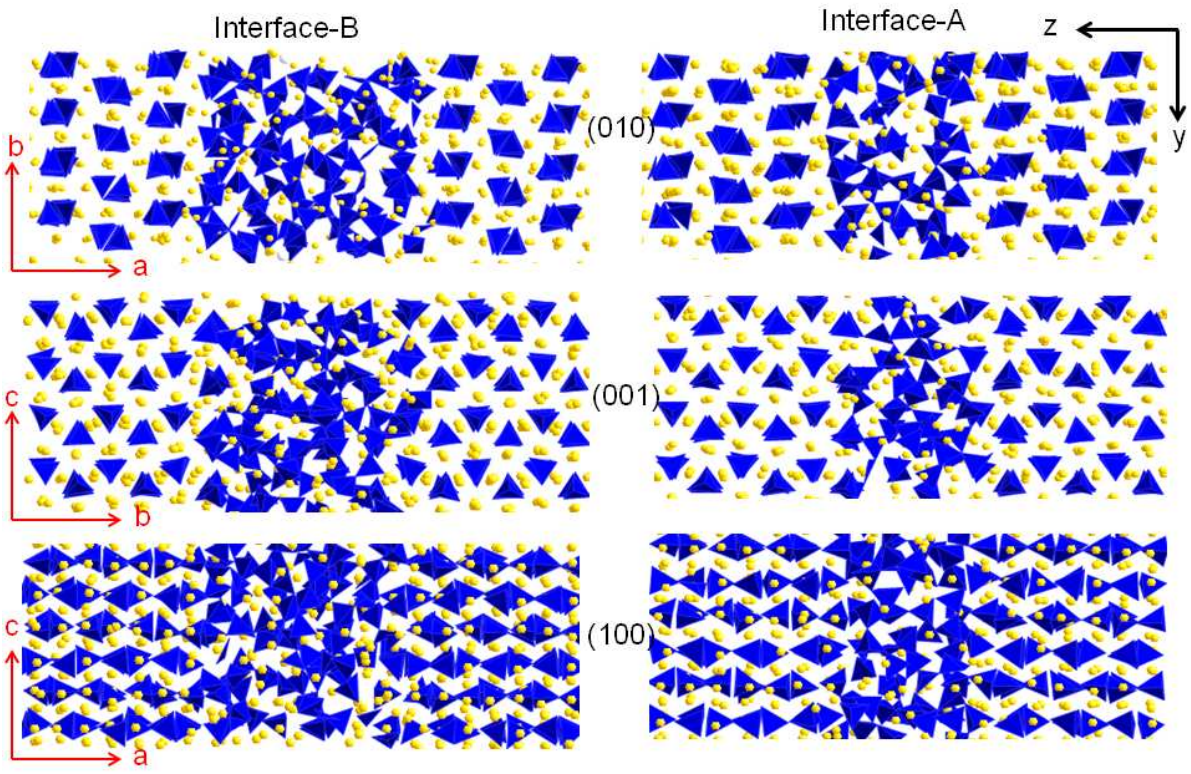


Fig. 3.15: Snapshot of interface A and B with all three crystal surface terminations

interface, e.g. interface-B, are due to the different cross-sections of the crystal in (010), (100) and (001) and a constant number of atoms in the initial cell. This difference in melt thickness can be observed from the snapshots of interface-B for three crystal surface termination as shown in figure 3.15.

Similar behavior is observed for interfaces C and D. As the melt thickness increases from interface B to D, a decrease in the structuring of the melt part of the interface with (010) crystal surface termination is observed. Also in the other two crystal surface terminations (001) and (100), the structuring of the melt part is reduced. In case of the smallest melt thickness, it is difficult to differentiate clearly the effect of surface termination from the structure due to the confinement. Interfaces A have a melt thickness of about 0.88 nm, but still from the snapshot of interface A we can observe that the

interface with (010) crystal surface termination has a little broader thickness of melt as compared to the other (100) and (001).

### 3.1.4 Self-Diffusion Coefficients

The self-diffusion coefficients are calculated by two different methods for all interfaces. In the first case, all atoms that were contained in the original melt before constructing the interface are considered in the averaging of the mean square displacements. A time average is performed over 500 ps of the production runs.

Table 3.6: Self diffusion coefficients ($\times 10^{-6}$cm$^2$/s) of the three elements (O, Si, Mg) in A, B, C and D interfaces and for the three crystal orientations (100), (010) and (001). $d^{tot}$ (nm) is the total melt layer thickness. The three columns on the left represent self-diffusion coefficients that are derived from the complete melt, whereas the three columns on the right include averaging over the central melt part only (see main text for more explanations).

| Interface | Melt-thickness $d^{tot}$ (nm) | O | Si | Mg | O | Si | Mg |
|---|---|---|---|---|---|---|---|
| | | total melt | | | central melt | | |
| A | | | | | | | |
| 100 | 0.80 | 1.1(2) | 0.6(2) | 3.4(3) | 1.1(2) | 0.6(2) | 4.0(2) |
| 010 | 0.88 | 1.9(2) | 1.2(2) | 6.4(16) | 2.0(2) | 1.2(1) | 8.4(14) |
| 001 | 0.77 | 1.2(2) | 0.6(2) | 3.2(7) | 1.2(3) | 0.6(2) | 4.4(3) |
| B | | | | | | | |
| 100 | 1.60 | 1.4(2) | 0.9(2) | 5.9(7) | 1.5(3) | 1.0(2) | 7.2(8) |
| 010 | 1.75 | 2.2(2) | 1.5(2) | 7.4(7) | 2.4(3) | 1.6(3) | 9.1(7) |
| 001 | 1.54 | 1.7(2) | 1.1(2) | 7.1(5) | 1.8(3) | 1.2(2) | 7.9(5) |
| C | | | | | | | |
| 100 | 3.20 | 1.8(2) | 1.2(2) | 7.9(11) | 2.0(2) | 1.4(2) | 9.2(12) |
| 010 | 3.50 | 2.4(2) | 1.7(2) | 9.2(4) | 2.5(2) | 1.8(3) | 10.0(7) |
| 001 | 3.10 | 2.0(2) | 1.3(1) | 8.0(6) | 2.2(2) | 1.5(2) | 9.3(9) |
| D | | | | | | | |
| 100 | 6.40 | 2.2(2) | 1.5(2) | 8.1(7) | 2.4(2) | 1.7(3) | 9.2(11) |
| 010 | 7.00 | 2.6(2) | 1.9(2) | 9.3(2) | 2.7(4) | 2.1(3) | 10.0(8) |
| 001 | 6.20 | 2.3(2) | 1.5(1) | 8.3(5) | 2.3(3) | 1.6(2) | 9.0(7) |

In the second case, the interface is divided into 10, 15, 20 and 30 equidistant layers for the A, B, C and D interfaces, respectively. To account for interdiffusion between the

layers, the time average over the mean square displacements is constrained to intervals of 100 ps. This means that for production runs of 700 ps, there are seven intervals of 100 ps. The assignment of atoms to individual layers is made at the beginning of each 100 ps interval. Finally, an average over the seven intervals is taken. Self-diffusion coefficients of all three species are averaged over a few central layers (2, 3, 6 and 12 for all A, B, C, and D interfaces, respectively). The resulting self-diffusion coefficients are compiled in Table 3.6.

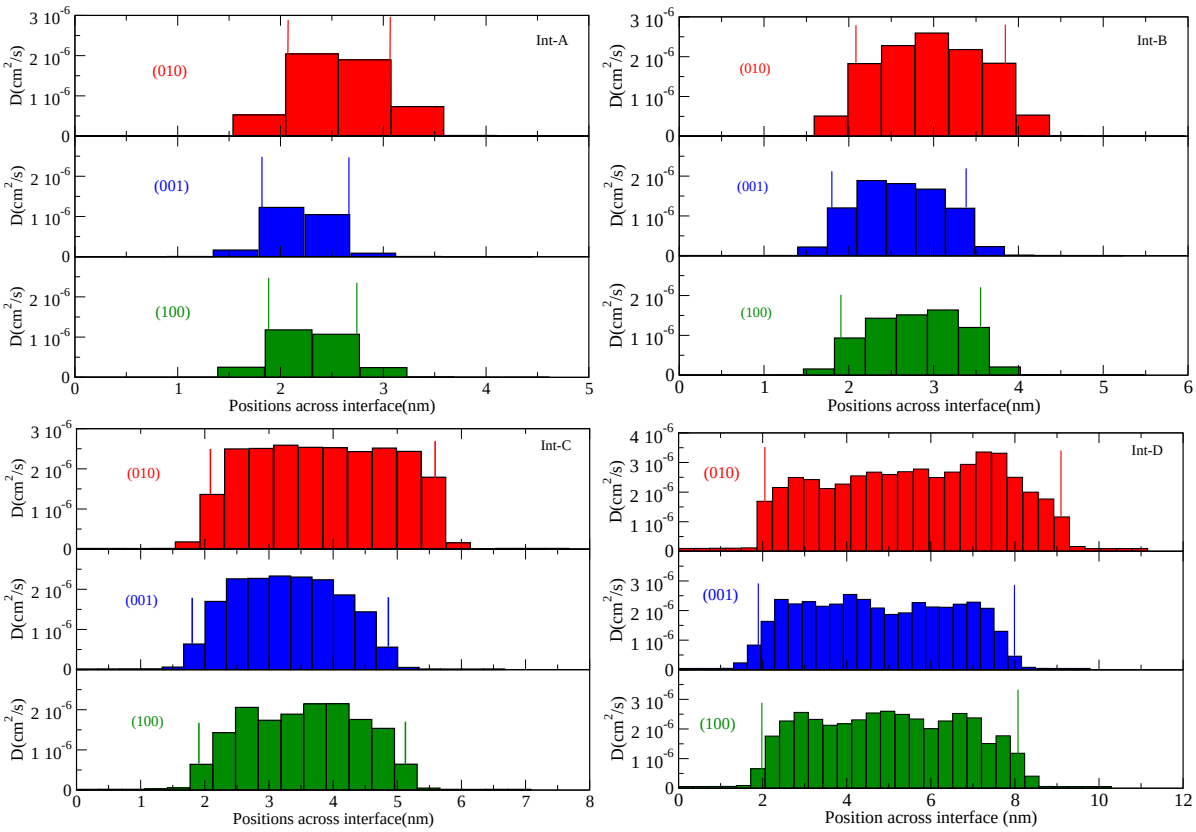


Fig. 3.16: Self-diffusion coefficients of oxygen across the interface for crystal surface terminations (010), (001) and (100) of all interfaces A-D. The vertical lines on each profile present the initial interface.

For all interfaces A to D, the atoms of crystal termination (010) show higher self-diffusion coefficients then those of the corresponding interfaces with (100) and (001) termination. By increasing the melt thickness of the same crystal surface, the self-diffusion coefficients

of all species increase. The largest difference is observed between the melts of interfaces A and B with an increase in diffusivity of up to about 40%. This increase reduces to about 20% between interfaces C and D (see Table 3.6).

Fig. 3.16 shows profiles of oxygen self-diffusion coefficients across all the interfaces A-D with different crystal orientations. The vertical lines on each plot refer to the initial contact between melt and crystal. The simulation cell lengths and hence the effective melt thickness in all four interfaces vary slightly between different crystal surface terminations due to the different cross-sections of the crystal in (100), (010) and (001) (see Table 3.6). While the diffusion in the crystal part is essentially zero, a plateau is formed in the central part of the melt. For the interface with (010) crystal orientation, the self-diffusion coefficients in this central region are higher than those for the other two profiles. Also, in the (010) profile the plateau is reached more quickly away from the original contact, which indicates a smaller interfacial width. Non-zero self-diffusion in the crystal part indicate an increased ionic mobility in the first atomic layers of the crystal close to the contact with the melt. The extend of the diffusion profiles into the crystal is consistent with that of the composition fluctuations (see Fig. 3.12), which can be explained by an increased defect density in the crystal or by the formation of a leached layer.

Fig. 3.17 shows the dependence of the oxygen self-diffusion coefficients for the different crystal terminations as a function of melt thickness. In this figure, both data of the complete melt and the central melt part are drawn, which shows clearly that the diffusion of the complete melt is somewhat smaller than that of the central melt part. A similar trend is observed for the Mg and Si self-diffusion coefficients (see Table 3.6). Averaging of the central layers gives higher self-diffusion coefficients because the electrostatic effect of crystal on the melt is better shielded away from the interface. Averaging over the complete melt also includes the region close to the interface which is less diffusive. By

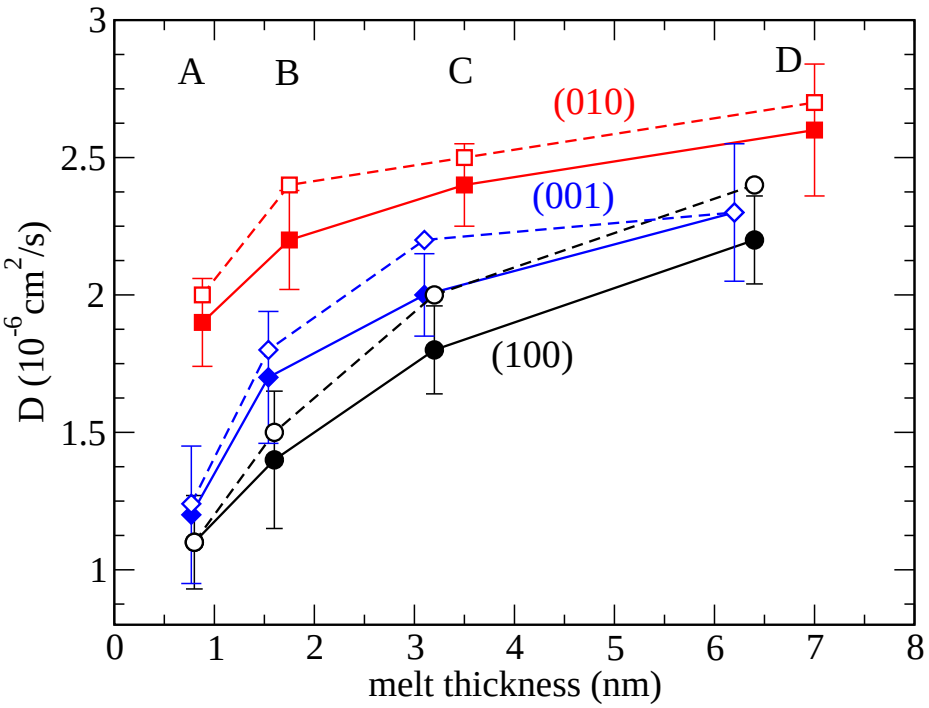


Fig. 3.17: Self-diffusion coefficients of oxygen for different melt thickness and different surface termination. Filled symbols are for the complete melt and open symbols refer to the central melt part. Lines are a guide to the eye.

making the melt layer thicker, the self-diffusion coefficients converge to the pure melt value and if the melt layer becomes very thin, the self-diffusion approaches that of the pure crystal, which is not observable on the time scale of our simulations.

### 3.1.5 Addition of Calcium (Ca)

In a first attempt to model a more complex melt composition, eighteen Mg atoms are replaced by Ca atoms in the melt of interface C with (100) crystal surface termination. Both cations have the same charge but different atomic size. Figure 3.18 shows a snapshot of interface-C with Ca atoms. This image is taken after a simulation run of 500 ps.

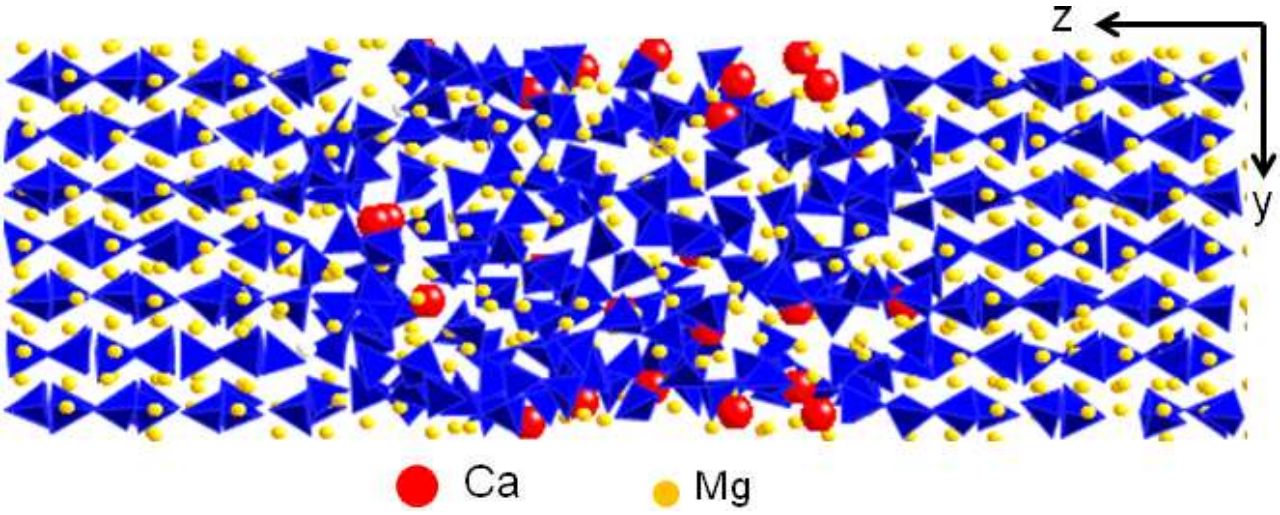


Fig. 3.18: Snapshot of interface-C and (100) crystal surface termination with 18 Ca replacing Mg cations.

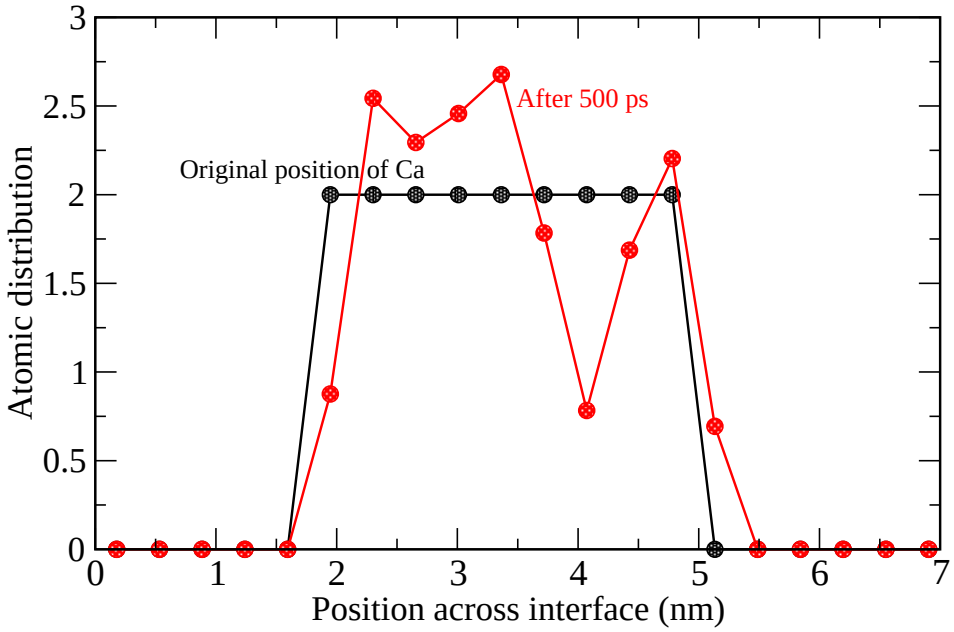


Fig. 3.19: Atomic density profiles of interface-C with Ca impurity of (100) crystal surface termination.

Figure 3.19 represents the atomic distribution profile of Ca. Black circles show the original position of Ca when added to the interface and red circles show the distribution of Ca after the 500 ps production run. After 500 ps, there is one Ca atom in the first layer of the direct contact area and similarly one atom in the second contact area. There are only two atoms of Ca in each layer. The coordination of Mg (left) and Ca (right) by oxygen is shown in figure 3.20. The plot for the coordination of Mg shows both the situations before and after adding Ca to the interface. Four and five-fold coordination of Mg is slightly decreased after adding Ca. Six-fold coordination of Mg is slightly increased due to Ca addition. Ca have more seven fold coordination. Some six and eight fold coordination of Ca can be observed from the diagram 3.20 (right). The average Mg and Ca coordinations are 5 and 7 respectively.

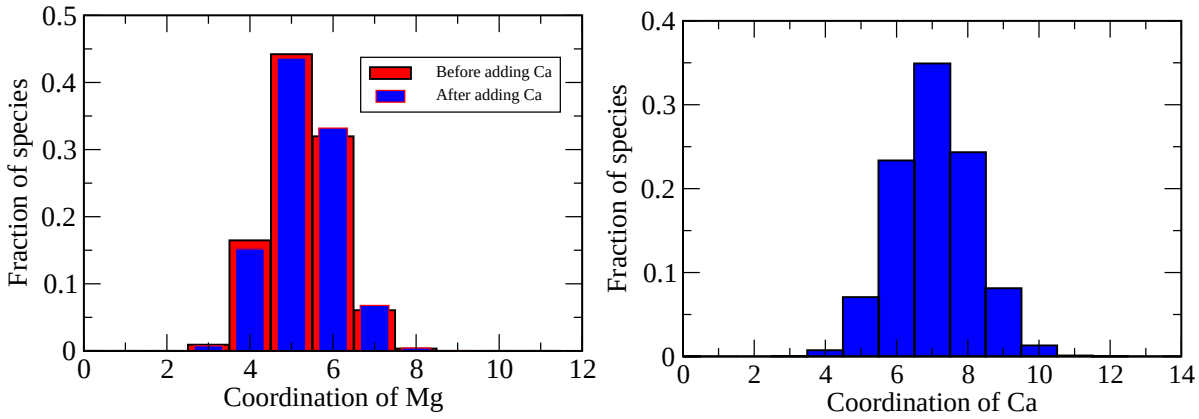


Fig. 3.20: Coordination of Mg before and after adding Ca (left) and Ca (right) of interface C with (100) crystal surface termination.

Table 3.7 shows the self-diffusion coefficients of all four elements. By adding Ca to the interface, the self-diffusion coefficients of oxygen and Si increases slightly and of Mg decreases. Ca is slower then Mg by a factor of 2 as shown in the tables 3.7 and 3.8.

| Interface C (100) | | | |
|---|---|---|---|
| Total melt | | | |
| O | Si | Mg | Ca |
| 2.1(2) | 1.4(2) | 7.4(3) | 5.1(2) |

Table 3.7: Self-diffusion coefficients ($\times 10^{-6}$cm$^2$/s) of the four elements (O,Si,Mg,Ca) of interface-C with (100) crystal surface termination (interface with Ca) of total melt (Averaged over 500 ps).

| Interface C (100) | | |
|---|---|---|
| Total melt | | |
| O | Si | Mg |
| 1.8(2) | 1.2(2) | 7.9(4) |

Table 3.8: self-diffusion coefficients ($\times 10^{-6}$cm$^2$/s) of the three elements (O,Si,Mg) of interface-C with (100) crystal surface termination (interface without Ca) of total melt (Averaged over 700 ps).

### 3.1.6 High Pressure and High Temperature Effect on Properties

To see the effect of different pressure and temperature ranges on our system, we studied the system (without Ca) at two different conditions. The choice of these pressure and temperature range is done according to the phase diagram of forsterite (e.g see figure(14) of Presnall (1995)). Forsterite should remain crystalline, and not be affected by changing the pressure and temperature conditions. The pressure is increased from 0 to 10 GPa with two different range of temperatures. First case is temperature of 2000 K with 10 GPa pressure, and second case is temperature of 2400 K with 10 GPa pressure. All four interfaces (A-D) with (010) crystal surface termination are investigated at these conditions.

**• Self-Diffusion Coefficients and Structured at 10 GPa and 2000 K**

In this case the pressure is increased from 0 GPa to 10 GPa, but the temperature is kept the same as in the previous calculations. Table 3.9 shows the self-diffusion coefficients of the three species for interfaces A-D with (010) crystal surface termination. The data presented in Table 3.9 is averaged over 400 ps by considering the complete melt part in each interface.

From this data, a decrease of the self-diffusion coefficient is observed. It seems that the $MgSiO_3$ melt starts to freeze in at 10 GPa and 2000 K. Enhanced ionic mobility is only

Table 3.9: Self diffusion coefficients ($\times 10^{-6}$cm$^2$/s) of the three elements (O, Si, Mg) in A, B, C and D interfaces for (010) crystal orientation at 10 GPa and 2000 K. $d^{tot}$ (nm) is the total melt layer thickness. The three columns represent self-diffusion coefficients of O, Si and Mg that are derived from the complete melt (Averaged over 400 ps).

| Interface (010) | Melt-thickness $d^{tot}$ (nm) | O | Si | Mg |
|---|---|---|---|---|
| | | total melt | | |
| A | 0.88 | 1.9(2) | 1.1(2) | 4.2(16) |
| B | 1.75 | 1.1(2) | 0.7(2) | 1.8(7) |
| C | 3.50 | 1.0(2) | 0.6(2) | 1.7(4) |
| D | 7.00 | 1.0(2) | 0.7(2) | 1.7(2) |

observed for interface A which has the smallest amount of melt (see figure 3.22). This may be due to the strong confinement effect (Alba-Simionesco et al., 2006).

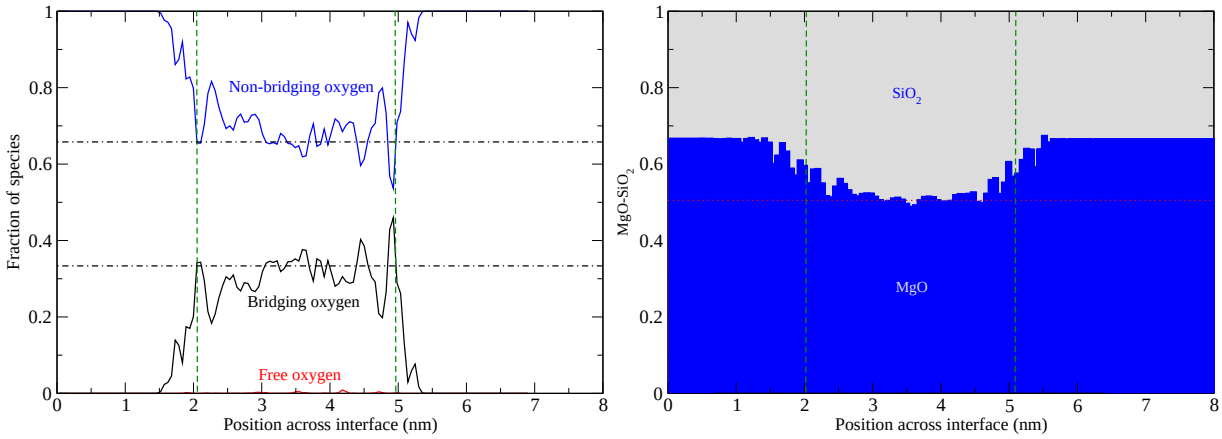


Fig. 3.21: Coordination and chemical composition profiles at 10 GPa and 2000 K

Looking at the structural properties (Fig. 3.21), it is difficult to identify the clear difference between the two different pressure conditions as we observe in the self-diffusion coefficients. Still, if we compare the oxygen coordination and the chemical composition profiles (see Fig. 3.12 and 3.21), the melt part and the contact region seem to be more structured at 10 GPa. The number of free oxygens in the coordination profile at 10 GPa is decreased compared to the profile at ambient pressure (Fig. 3.13 Int-

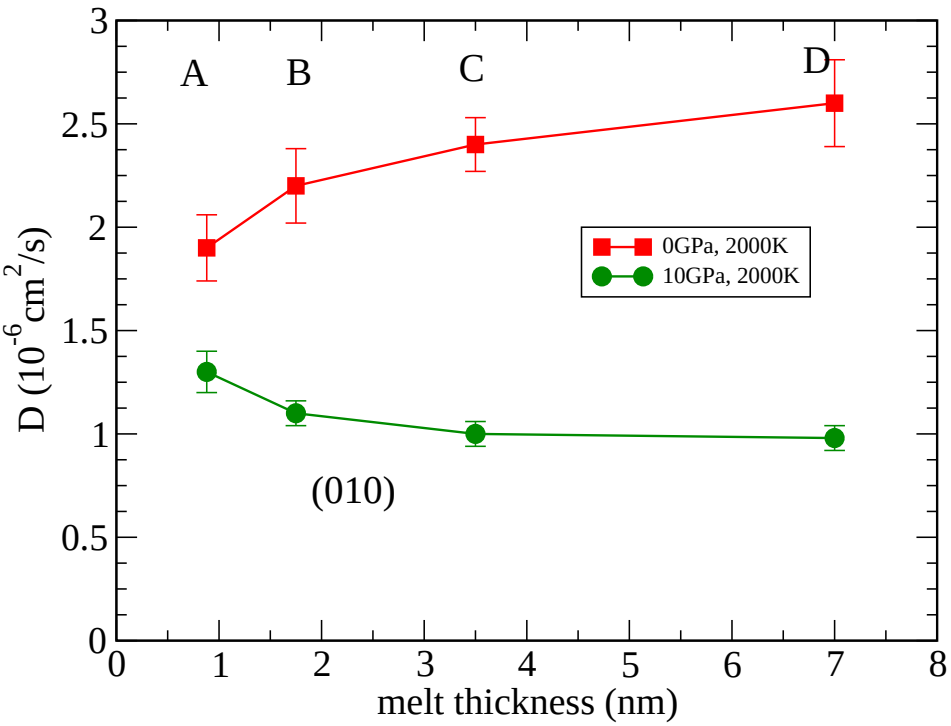


Fig. 3.22: Self-diffusion coefficients of oxygen for different melt thickness for crystal orientation (010). Results are compared between two different $P-T$ conditions. The results for ambient pressure correspond to those in figure 3.17

C). Fluctuations in the plot of bridging and non-bridging oxygens are increased in the central melt and some peaks crossed over the horizontal lines which is not observed in case of the coordination profile at ambient pressure.

• **Self-Diffusion Coefficients and Structure at 10 GPa and 2400 K**

Table 3.10 contains the self-diffusion coefficients of Mg, Si and O for interfaces A-D of the (010) crystal surface termination at 10 GPa and 2400 K.

From the pressure-temperature phase diagram of forsterite, this was possible to maintain the crystalline structure of forsterite (Presnall, 1995). Fig. 3.23 compares the evolution of the self-diffusion coefficients at 10 GPa and 2400 K (green circles) to that at 0 GPa and 2000 K (red boxes). At the higher P-T conditions, oxygen has a higher self-diffusion coefficients. Interface A shows a distinctly different behavior compared to interfaces B-

Table 3.10: Self diffusion coefficients ($\times 10^{-6}$cm$^2$/s) of the three elements (O, Si, Mg) for interfaces A-D wit (010) crystal surface termination at 10 GPa and 2400 K, $d^{tot}$ (nm) is the total melt layer thickness. The three columns represent self-diffusion coefficients of O, Si and Mg that are derived from the complete melt (Averaged over 400 ps).

| Interface (010) | Melt-thickness $d^{tot}$ (nm) | O | Si | Mg |
|---|---|---|---|---|
| | | total melt | | |
| A | 0.88 | 1.5(2) | 0.9(2) | 1.5(14) |
| B | 1.75 | 4.2(2) | 3.4(2) | 8.7(7) |
| C | 3.50 | 5.4(2) | 4.0(2) | 10.8(4) |
| D | 7.00 | 5.8(2) | 4.5(2) | 11.0(4) |

D. The difference in oxygen self-diffusion coefficient between the two P-T conditions (see figure 3.23) is very small for interface A as compared to interfaces C-D. This is due to the very thin melt layer in interface A. Even at such a high pressure and temperature, the atoms have a reduced mobility due to confinement effect.

Figure 3.24 shows the coordination and chemical composition profiles at 10 GPa and 2400 K. They look very similar to the structure at 0 GPa and 2000 K. The chemical composition profile shows more fluctuations in the interfacial region at 10 GPa and 2400 K as compared to the profile at 0 GPa and 2000 K (see figure 3.12 for Int-C). The central melt region has only small fluctuations in the chemical composition. Strong oscillations are observed in the coordination profile at 10 GPa and 2400 K as compared to coordination profile at 0 GPa and 2000 K for interface C with (010) crystal surface termination (see Fig.3.13).

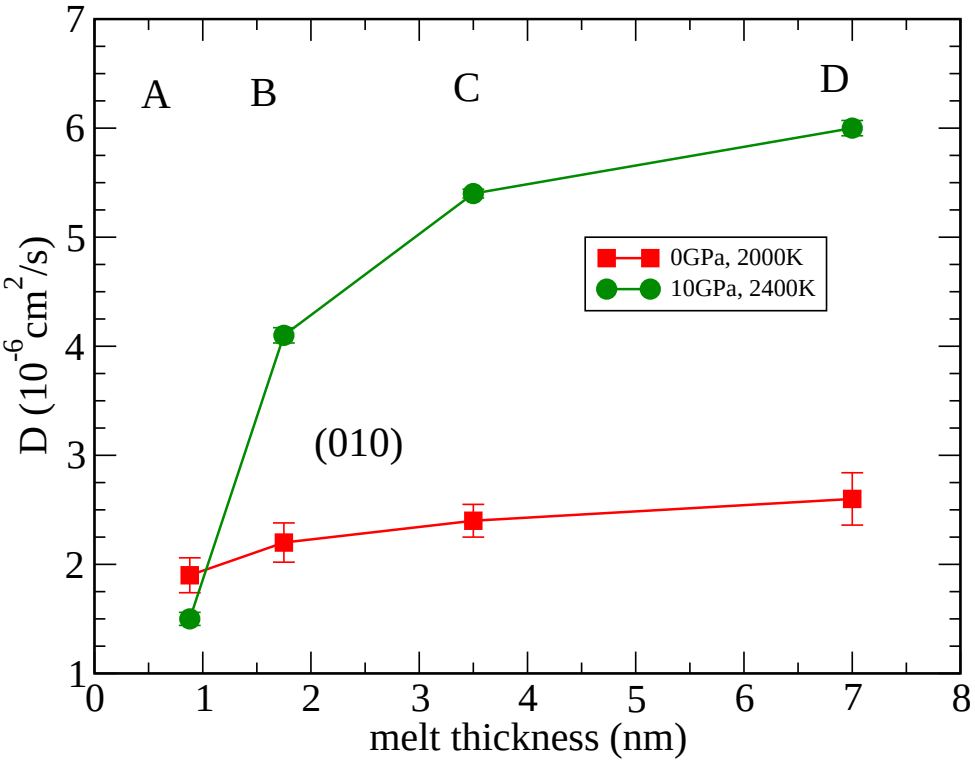


Fig. 3.23: Self-diffusion coefficients of oxygen for different melt thickness for crystal orientation (010). Results are compared between two different $P-T$ conditions.

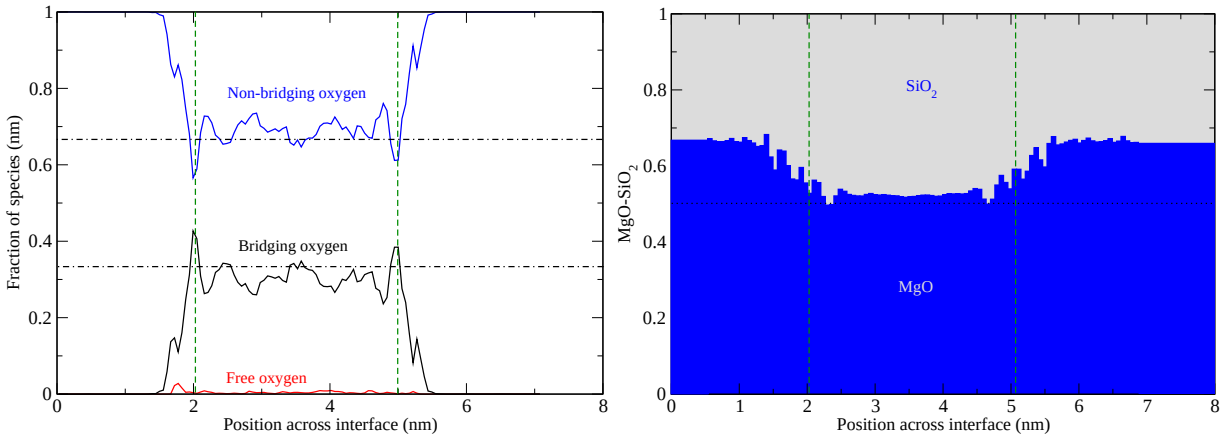


Fig. 3.24: Coordination and chemical composition profiles at 10 GPa and 2400 K

## 3.2 Non-Equilibrium Molecular Dynamics Simulation

A constant shear rate is applied to the system via non-equilibrium molecular dynamics simulation to calculate the viscosity for the different interfaces with (010) crystal surface termination. While the main goal is to discuss viscosity of the system, structural differences between equilibrium and non-equilibrium MD are investigated first at ambient pressure and temperature of 2000 K.

### 3.2.1 Structural Properties

To compare the structural properties between the equilibrium molecular dynamic (EMD) and non-equilibrium molecular dynamics (NEMD) simulations, we continue with interface C of orientation (010). Similar behavior is observed for the other interfaces (A, B, and D).

- **Charge Density Profiles**

Fig. 3.25 shows the charge and atomic distribution profiles of interface C of (010) crystal surface termination with (left) and without shear (right). These profiles are averaged results over the total production run of 700 ps. Comparing both EMD and NEMD simulation results, the profiles look very similar except that a small difference is observed in the central region which is less spiky in NEMD distribution profiles as compared to EMD.

- **Chemical Composition**

The chemical composition profiles in terms of MgO and $SiO_2$ components for interface C with (010) orientation with (left) and without shear (right) are shown in Fig. 3.26. In the interfacial region, both EMD and NEMD chemical profiles look similar. In the center of the melt, peaks are sharper in EMD as compared to the NEMD profile.

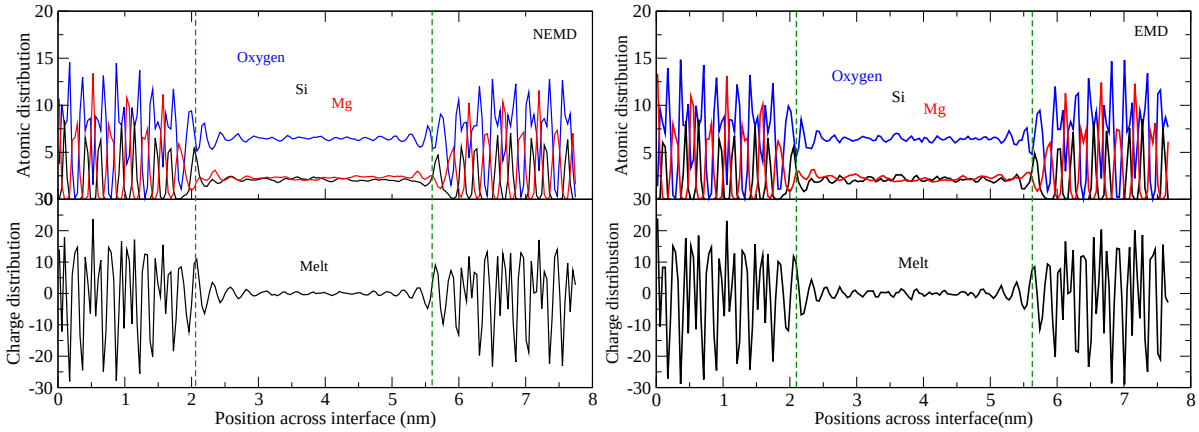


Fig. 3.25: Average atomic (upper graph) and charge (lower graph) distribution profiles across interface C of (010) crystal orientation with (left) and without (right) shear.

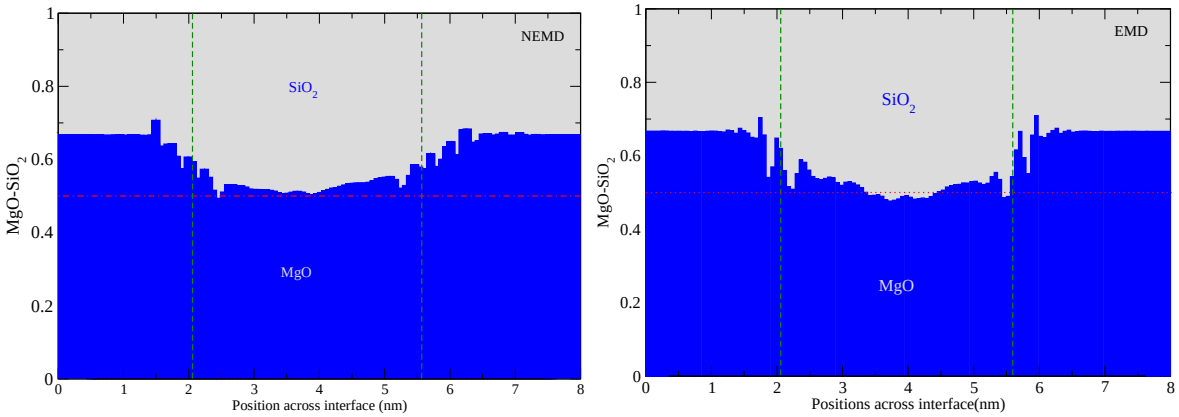


Fig. 3.26: Chemical composition across interface C of (010) crystal orientation with (left) and without (right) shear, in terms of MgO and $SiO_2$ components.

- **Coordination**

Sharper peaks are observed in NEMD coordination profile as compared to EMD along the contact area between crystal and melt as shown in figure 3.27. But in the central region, the EMD profiles are more spiky.

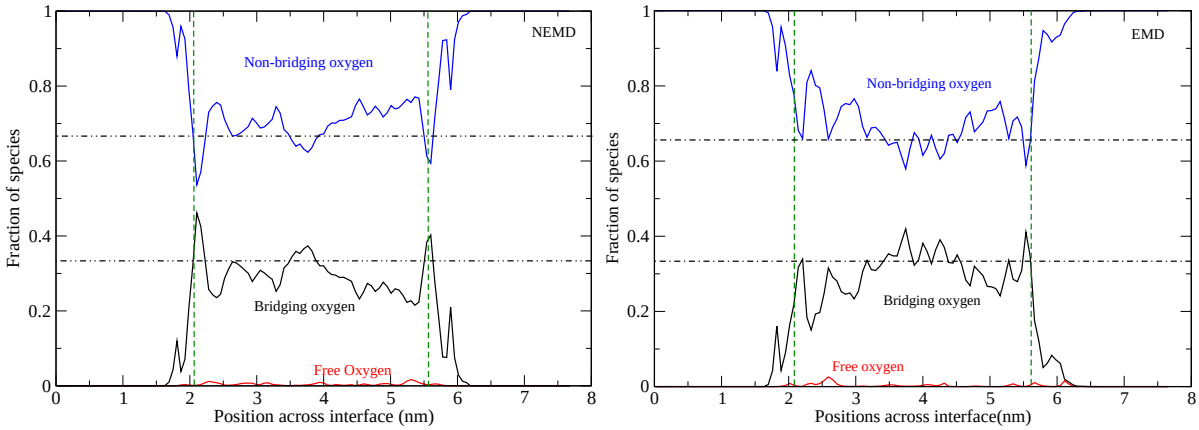


Fig. 3.27: Fractional distribution of oxygen coordinations by silicon as a function of position across interface C of (010) crystal surface termination with (left) and without (right) shear.

### 3.2.2 Viscosity

The shear viscosity, often referred to as simply viscosity, which describes the response of the system to an applied shear stress, is calculated for bulk melt and interfaces for (010) crystal orientation at different shear rates by using the following relation which is already described in detail in section 2.5.5.

$$\eta = \frac{\sigma_{ij}}{\frac{du}{dz}} \tag{3.2}$$

$\sigma_{ij}$ is the shear stress and $\frac{du}{dz}$ the velocity gradient. A constant shear rate is imposed on the simulation cell and the resulting stationary shear stress is obtained from molecular dynamics.

To obtain the viscosity for a given shear rate, the time average over the shear stress is evaluated in intervals of 100 ps. This means that for the production runs of 600 ps, there are six individual intervals of 100 ps. Finally, an average over the six intervals is taken and presented here.

Tables 3.11 and 3.12 present the viscosity data of bulk melt of different sizes at different

| Bulk melt (1.75 nm) | |
|---|---|
| Shear rate ($s^{-1}$) | Viscosity (Pas) |
| $10^9$ | 1.10(2) |
| $10^8$ | 1.80(7) |

Table 3.11: Viscosity of bulk melt of thickness 1.75 nm at different shear rate

| Bulk melt (3.50 nm) | |
|---|---|
| Shear rate ($s^{-1}$) | Viscosity (Pas) |
| $10^{11}$ | 0.060(2) |
| $10^9$ | 0.10(7) |

Table 3.12: Viscosity of bulk melt of thickness 3.50 nm at different shear rate

| Interface-A | |
|---|---|
| Shear rate ($s^{-1}$) | Viscosity (Pas) |
| $5.8 \times 10^{11}$ | 0.0030(2) |
| $5.8 \times 10^{10}$ | 0.020(7) |
| $5.8 \times 10^9$ | 0.040(7) |
| $5.8 \times 10^8$ | 0.180(7) |

Table 3.13: Viscosity of interface-A with melt thickness 0.88 nm at different shear rate

| Interface-B | |
|---|---|
| Shear rate ($s^{-1}$) | Viscosity (Pas) |
| $3.5 \times 10^{11}$ | 0.0060(2) |
| $3.5 \times 10^{10}$ | 0.030(7) |
| $3.5 \times 10^9$ | 0.070(7) |
| $3.5 \times 10^8$ | 0.20(7) |

Table 3.14: Viscosity of interface-B with melt thickness 1.75 nm at different shear rate

shear rate. From both tables of the bulk melt, we observe that the viscosity increases as the shear rate is decreasing. Tables 3.13 to 3.16 show the calculated viscosities for all interfaces at different shear rates. The shear rate presented here is the effective shear rate on melt (discussed before in section 2.6.3) in each interface. The interfaces show a similar trend as the bulk melt, i.e. inverse relation between viscosity and shear rate.

From all these tables, we observe a strong dependence of the viscosity on the shear rate. Viscosity versus shear rate is plotted in Fig. 3.28 for bulk melt and all interfaces. From the plotted data of viscosity and shear rate, we can see that the viscosity decreases as the shear rate increases. In figure 3.28, the experimental value of the viscosity of the $MgSiO_3$ melt at 2000 K and ambient pressure is also shown. The viscosity calculated

| Interface-C | |
|---|---|
| Shear rate ($s^{-1}$) | Viscosity (Pas) |
| $2.2 \times 10^{11}$ | 0.010(2) |
| $2.2 \times 10^{10}$ | 0.040(7) |
| $2.2 \times 10^{9}$ | 0.0860(7) |

Table 3.15: Viscosity of interface-C with melt thickness 3.50 nm at different shear rate

| Interface-D | |
|---|---|
| Shear rate ($s^{-1}$) | Viscosity (Pas) |
| $1.6 \times 10^{11}$ | 0.0130(3) |
| $1.6 \times 10^{10}$ | 0.050(7) |
| $1.6 \times 10^{9}$ | 0.090(7) |

Table 3.16: Viscosity of interface-D with melt thickness 7.0 nm at different shear rate

from equilibrium MD for the same composition is presented in the graph which and is then the NEMD viscosity.

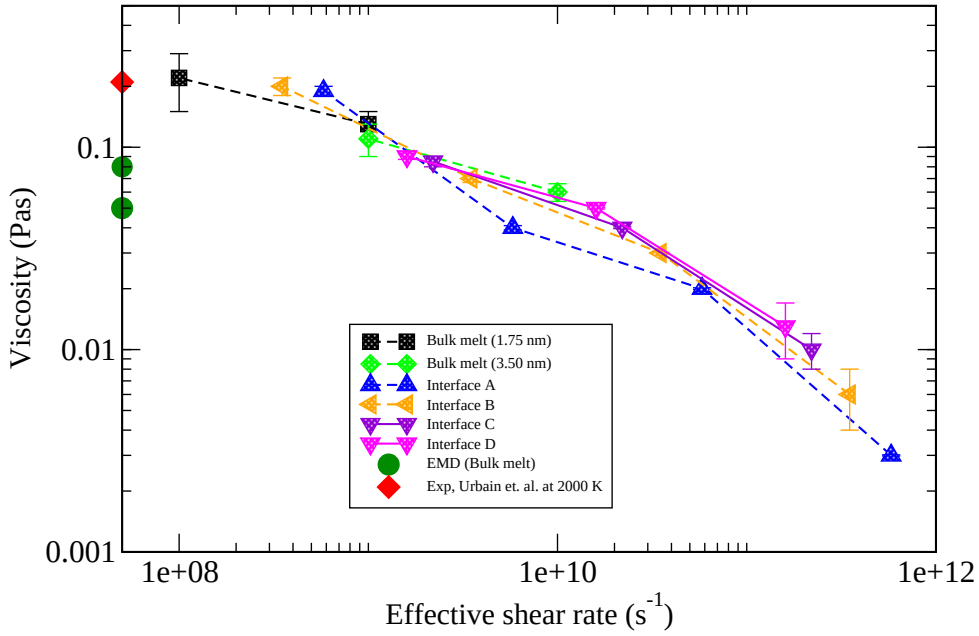


Fig. 3.28: Viscosity of bulk melt and interfaces as a function of effective shear rate on melt

Fig. 3.29 shows the correlation between shear stress and applied shear rate of our studied system. The plot is not linear, and the slope of shear stress versus shear rate curve is not constant as we change the shear rate. The plotted results of viscosity as

function of shear rate, and of shear stress as function of shear rate, (see figures 3.28 and 3.29 show a non-*Newtonian* behavior which will be discussed in next chapter. At low shear rate, the viscosity should approach the bulk value. Similar behavior is observed for different interfaces and bulk melt. There is no strong dependence on melt thickness as we observe in the case of the self-diffusion coefficients.

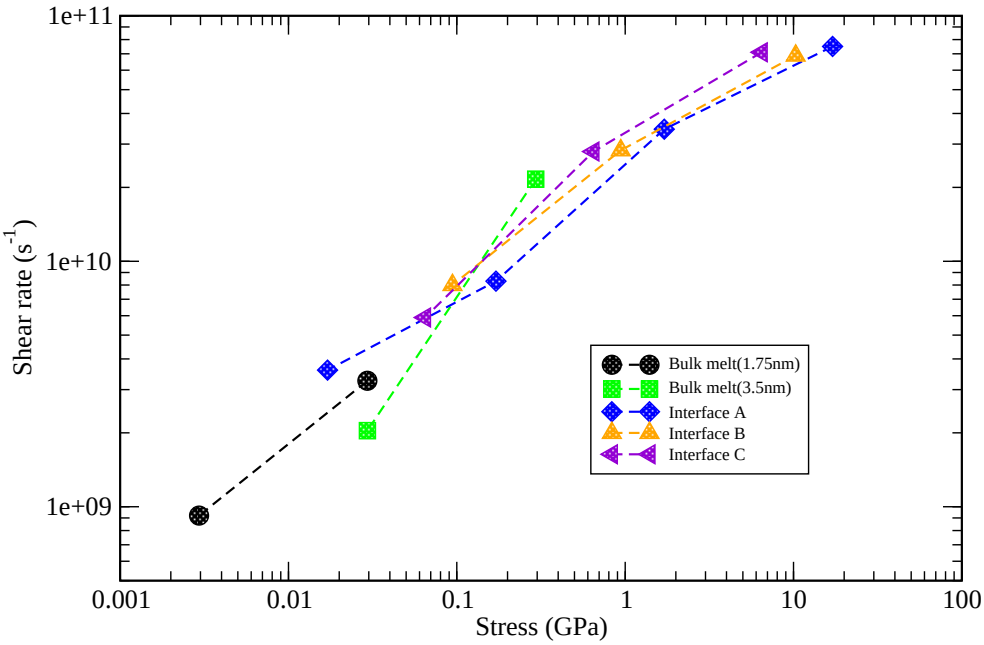


Fig. 3.29: Shear stress of bulk melt and interfaces A-D as a function of applied shear rate.

# Chapter 4

# Discussion

## 4.1 Structure at the Interface

As shown in Figs 3.12 and 3.13, strong oscillations of structural parameters are observed in the vicinity of the initial interface. Looking at the molecular structure at the contact between melt and crystal, information on the wetting behavior can be obtained. In the present case, $Mg_2SiO_4$ and $MgSiO_3$ are structurally quite similar. The crystals of both

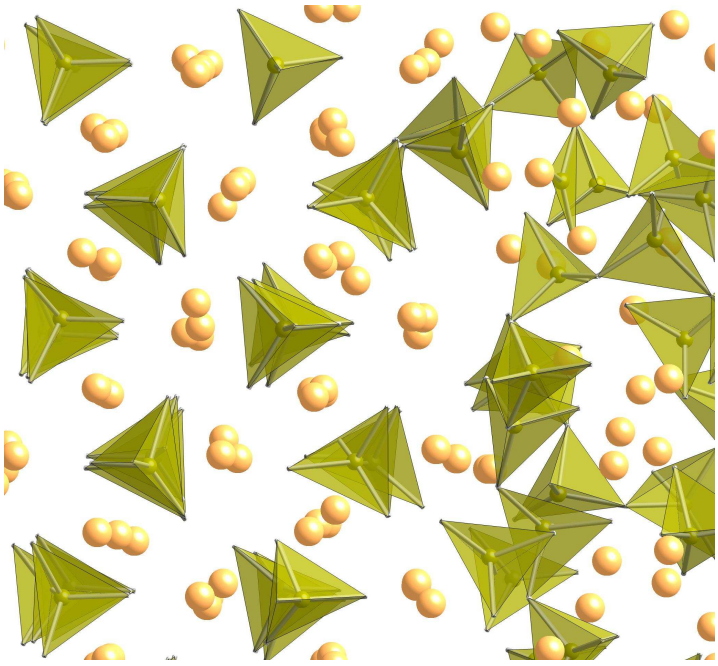

Fig. 4.1: Snapshot of the contact area between crystal (left) and melt (right). The alignment of the first melt layer(s) with the crystal surface causes fluctuations in the structural parameters, such as the number of bridging oxygens (see Fig. 3.13) in perpendicular direction to the interface.

systems are composed of $SiO_4$ tetrahedra and Mg in 6-fold octahedral coordination. The latter is reduced to an average 5-fold coordination in the melt (see Fig. 3.20). While in $Mg_2SiO_4$ forsterite the $SiO_4$ are not connected, in $MgSiO_3$ about 2 out of 4 oxygens are bridging oxygens that connect neighboring tetrahedra. In the contact area between the two phases (see Fig. 4.1), a partly polymerized meets a fully depolymerized structure. Some of the melt tetrahedra connect directly to tetrahedra of the crystal as shown in the upper part of the interfacial region in Fig. 4.1. In other parts, the first layer of the melt aligns parallel to the crystal surface, which leads to a fluctuating chemical composition and variations in the probability to find bridging oxygens. In contrast, the relaxation of the free surfaces as shown in Fig. 3.10 does not result in the formation of bridging oxygens.

## 4.2 Relation between Diffusion and Surface Energy

All ionic species (O, Si, Mg) have higher self-diffusion coefficients in the vicinity of the (010) as compared to (100) and (001) crystal surfaces. Looking at Table 3.5, (010) has the lowest surface energy of the three surfaces. This suggests that there is an inverse relation between free surface energy and the mean self-diffusion coefficients of ions in the melt layer. Figure 4.2 shows the surface energies versus oxygen self-diffusion coefficients for the different interfaces and crystal orientations.

As the surface energy increases the self-diffusion coefficient decreases. Similar behavior is observed for Mg and Si (see Table 3.6). The reduced ionic mobility for high surface energies is related to the stronger interaction of the crystal surface with the melt, which leads to more structured melt close to the interface. The strong variation in surface energies (Table 3.5) clearly indicates that simplified dihedral angle concepts are not capable to model interfacial melt-mineral assemblages and that more complex models need

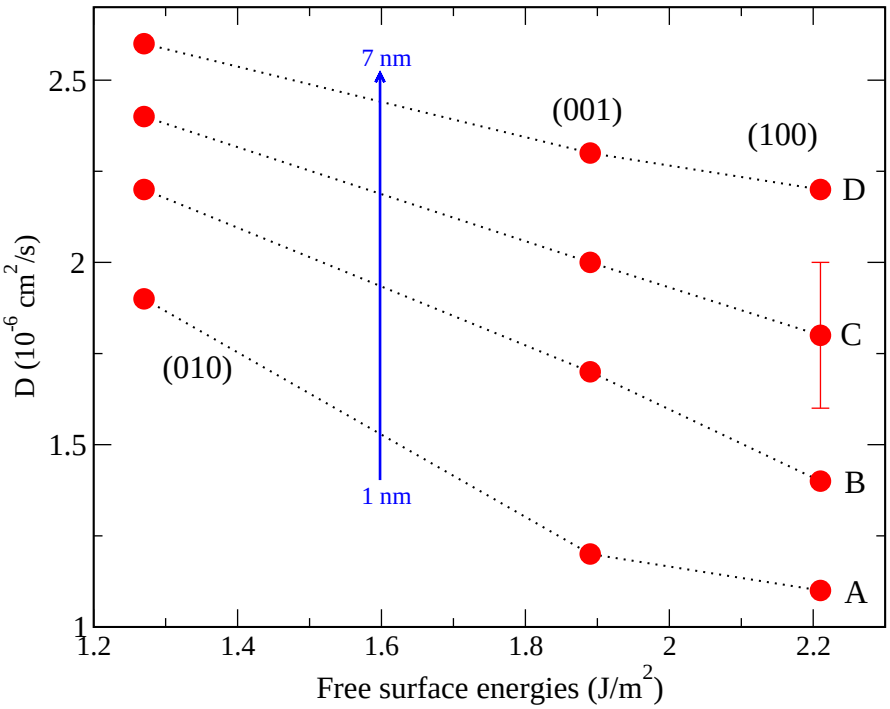


Fig. 4.2: Oxygen self-diffusion coefficients for different crystal surface terminations and melt layer thickness (interfaces A to D) with respect to free surface energies. All errors are in the same order as indicated for (100) of interface C. The dotted lines are a guide to the eye.

to be applied, e.g. (Cmiral et al., 1998). Such a study would require the computation of additional surface energies, especially of those surfaces with high Miller indices.

## 4.3 Confinement Effect on Self-Diffusion Coefficients

The self-diffusion coefficients of all three species (O, Si, Mg) in the melt are increased at 10 GPa and 2400 K as compared to the self-diffusion coefficients at 0 GPa and 2000 K as shown in figure 4.3. For all three crystal orientation the melt thickness increases from interfaces A-D, the self-diffusion coefficients increased as shown in figure 4.2. Similarly, by increasing the temperature and pressure, there is a huge (about 30 to 40 % for interfaces C-D compare to self-diffusion coefficients at ambient pressure and 2000 K)

increase in the self-diffusion coefficients for all three species O, Si, and Mg (see the plot for O 4.3). In case of interface A the self-diffusion coefficients decreases at 10 GPa and 2400 K as compared to other interfaces (C-D). The ionic mobility is reduced for interface A may be due to high pressure. For interfaces C-D, higher self-diffusion coefficients are due to high temperature.

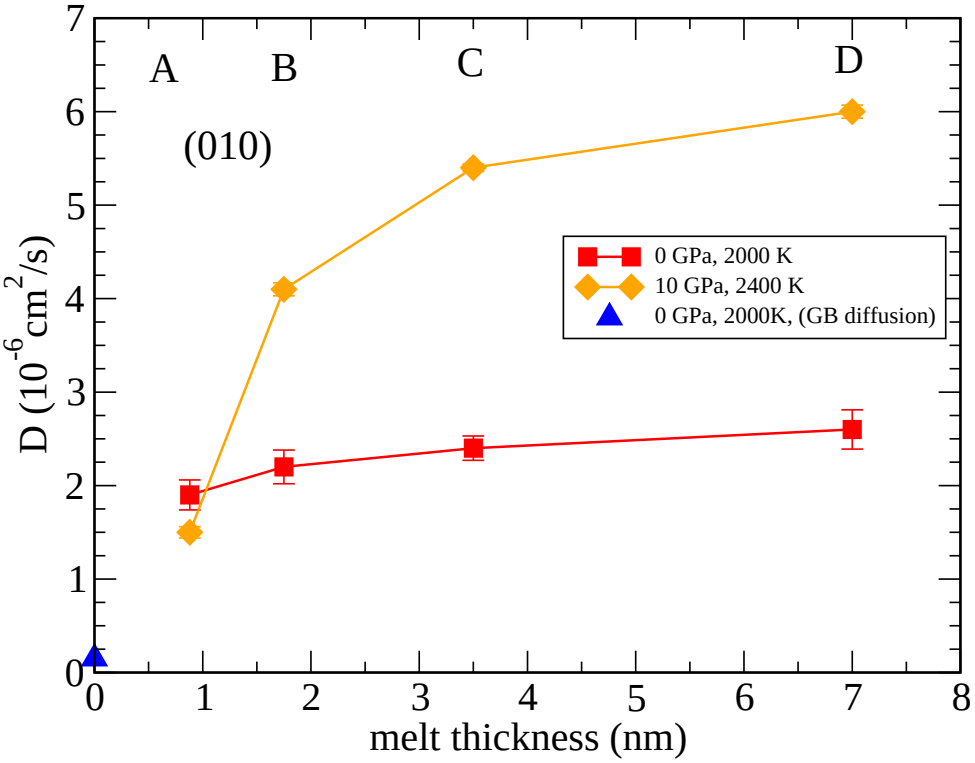


Fig. 4.3: Oxygen self-diffusion coefficient at three different pressure and temperature conditions, and symmetric grain boundary (GB) diffusion with tilt axis [010].

The data of the present study may be compared to the self-diffusion coefficients of symmetric grain boundaries with tilt axis of [010] (unpublished data from Dr. Omar Adjaoud with personal discussion) as shown in figure 4.3. From this comparison, we can observe that if the self-diffusion coefficient for interface A continues to decrease with time, it can approach to the self-diffusion in dry grain boundaries.

The time evolution plot for interface B at different P-T conditions is shown on the left

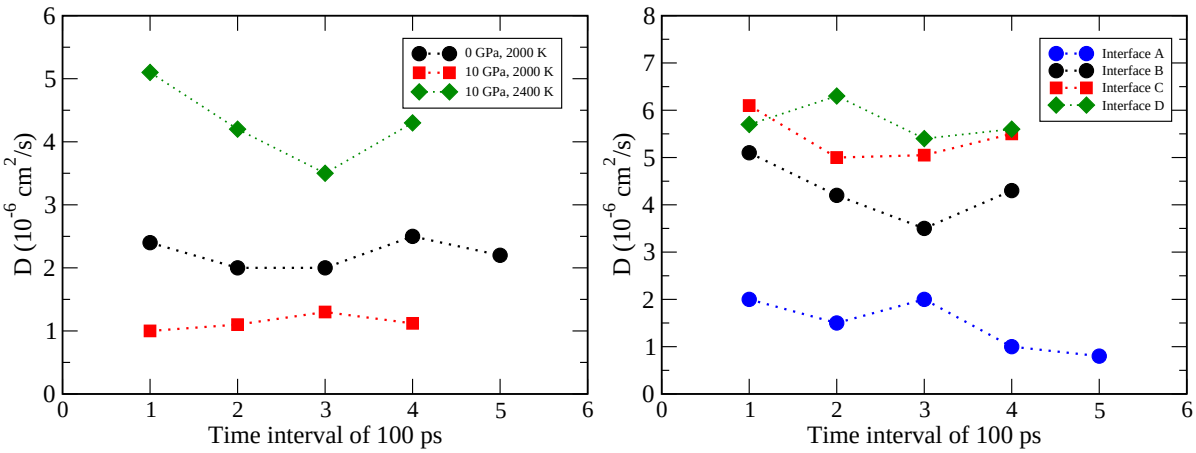


Fig. 4.4: Time evolution graph of oxygen self-diffusion coefficients of interface B (B) at different P-T conditions and for interfaces C-D (right) at 10 GPa and 2400 K with (010) surface termination at each interval of 100 ps.

plot of figure 4.4, and for different interfaces C-D at 10 GPa and 2400 K on the right. These figures show that the self-diffusion coefficients fluctuates when averaged over time intervals of 100 ps and that there is no systematic drift on time. This provides the evidence that the system has reached an equilibrium state. The self-diffusion coefficient for interface A is decreasing even after 500 ps which means that interface A does not reach to equilibrium.

## 4.4 Extrapolation to Bulk Diffusion Coefficient and Effective Passive Layer

The thickness of melt layers in partially molten rocks may be determined by transmission electron microscopy after quenching the sample to ambient pressure and temperature. Thereby it is assumed that melt layer is preserved as an amorphous layer. The thickness of this amorphous layer would be equivalent to the total thickness of the melt layer in the simulations. However, it has been shown above that not all particles of the same

kind contribute equally to the respective self-diffusion coefficient. Whereas particles in the central region of the melt may be almost as mobile as those in a bulk melt, the melt atoms close to the crystal surface diffuse much less. For practical use and as a first approximation, the derived diffusion profile of the total melt layer is divided into an active, bulk melt-like and a passive, essentially non-diffusive part. For that, we set

$$D^{tot} d^{tot} = D^{bulk} d^{eff} \tag{4.1}$$

where $D^{tot}$ and $D^{bulk}$ are the average self-diffusion coefficients of a particle in the melt layer of the crystal-melt interface and in the corresponding bulk melt. $d^{tot}$ is the total thickness of the melt layer in the interface and $d^{eff}$ is the effective thickness of the active layer. $D^{tot}$ and $d^{tot}$ are known from Table 3.6. $D^{bulk}$ is estimated from extrapolation of $D^{tot}$ to infinite melt layer thickness, where confinement effects are negligible.

A convincing extrapolation is achieved when $D^{tot}$ is plotted over the inverse square root of the melt layer thickness (see Fig. 4.5). The 480 atom simulation cell of pure $MgSiO_3$ melt has a slightly higher diffusivity than the confined melts but due to the relatively small simulation cell, finite size effects are apparent. A summary of the extrapolated $D^{bulk}$ is given in Table 4.1.

The thickness of the passive layer $d^{passive}$ of one crystal-melt interface is then given by

$$d^{passive} = (d^{tot} - d^{eff})/2 \tag{4.2}$$

Note that there are two interfaces and therefore two passive layers. The evolution of the passive layer thickness as a function of total melt layer thickness is shown for oxygen in Fig. 4.6. After a significant initial increase, a plateau is reached for thick melt layers.

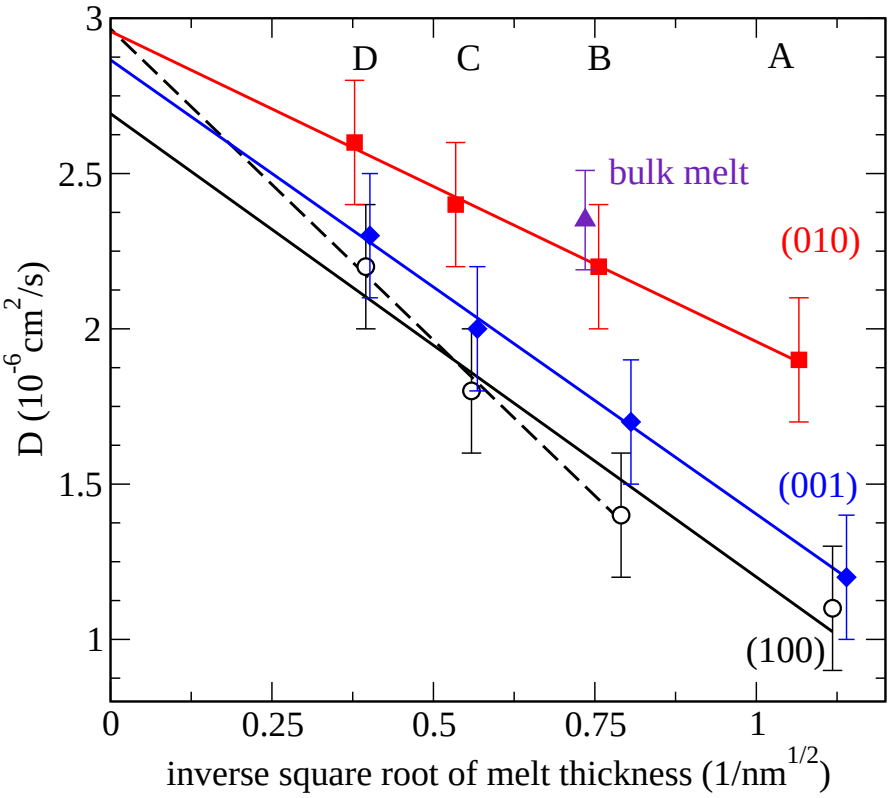


Fig. 4.5: Linear regression to self-diffusion coefficients of oxygen (all melt data of Table 3.6) plotted against the inverse square root of the total melt layer thickness. The dashed line refers to the (100) interfaces B to D only.

The data is well described by the relation

$$d^{passive} = d_{\infty}^{passive}(1 - \exp(-kd^{tot})) \tag{4.3}$$

where $d_{\infty}^{passive}$ is the maximum thickness of the passive layer for thick melt layers and $k$ is a constant. All fitted $d_{\infty}^{passive}$ and $k$ are listed in Table 4.1. We also attempted a self-consistent global fit of the self-diffusion data as a function of the total melt thickness by combining equations 4.1 to 4.3 but the small number of data points and their relatively large uncertainty resulted in large ambiguities of the fitted parameters. Within these uncertainties, however, those parameters were consistent with the results presented in Table 4.1.

Table 4.1: Extrapolated self-diffusion coefficients for bulk melt ($10^{-6}$ cm$^2$/s), thickness of the passive layer (nm) and $k$ fitting parameter of equation 4.3 (1/nm). Due to the relatively large errors in Mg self-diffusion coefficients (see Table 3.6), no meaningful estimation of $d_\infty^{passive}$ and $k$ for Mg could be obtained. [1]regression line fitted only to interfaces B to D

| | Surface | $D^{bulk}$ | $d_\infty^{passive}$ | $k$ |
|---|---|---|---|---|
| O | (100) | 2.69 | 0.60 | 0.64 |
| | (100)[1] | 2.97 | 0.82 | 0.44 |
| | (010) | 2.96 | 0.44 | 0.43 |
| | (001) | 2.87 | 0.64 | 0.46 |
| Si | (100) | 1.92 | 0.72 | 0.57 |
| | (100)[1] | 2.07 | 0.95 | 0.41 |
| | (010) | 2.26 | 0.58 | 0.43 |
| | (001) | 2.00 | 0.85 | 0.36 |
| Mg | (100) | 11.2 | | |
| | (010) | 11.2 | | |
| | (001) | 11.7 | | |

For thick melt pockets, the interfacial melt layer that has to be considered immobile is in the range of about 0.4 to 1.0 nm depending on the crystal surface termination. Although this thickness reduces for ultrathin films of only a few nanometers, its relative importance increases significantly. While for a total melt film of about 7 nm, the two passive layers comprise about 12% (010) to 24% (100) of the total melt thickness, these values increase to about 35% (010) to 60% (100) for a 1 nm thick melt. Thus, in the latter case the effective ionic mobility is reduced to half of that of the corresponding bulk melt.

The electrical conductivity of the bulk melt can be estimated by inserting the extrapolated self-diffusion coefficients $D^{bulk}$ (as substitute of the unknown conductivity diffusion coefficient) into the Nernst-Einstein equation

$$\sigma = \frac{e^2 n}{k_B T} \sum_i z_i^2 c_i D_i^{bulk} \tag{4.4}$$

where $e$ is the electronic charge, $n$ the particle density of the melt, $k_B$ the Boltzmann

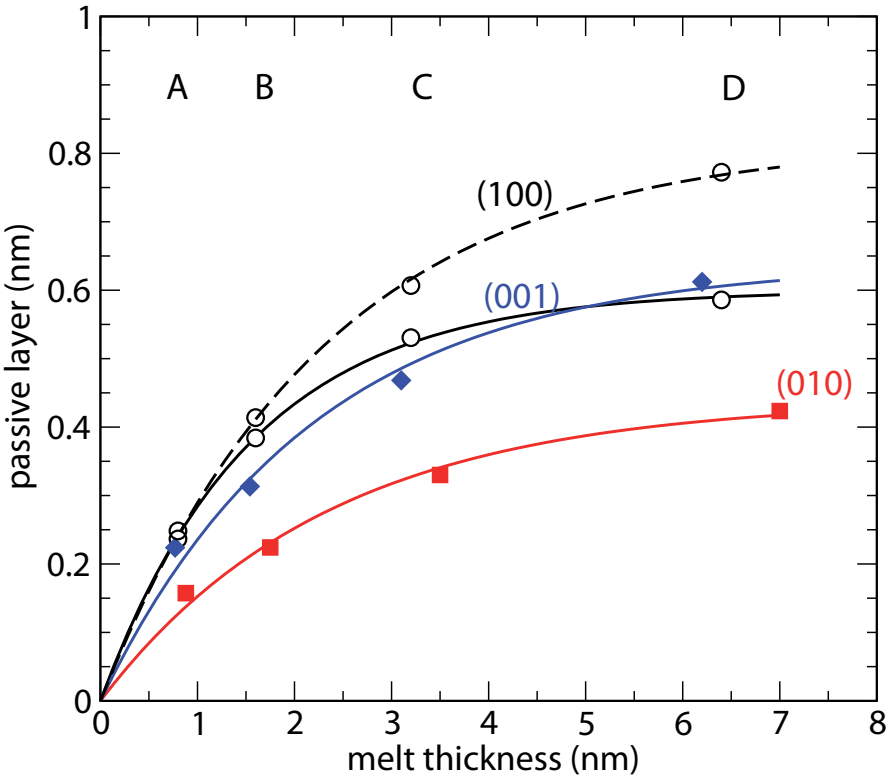


Fig. 4.6: Thickness of the passive layer of oxygen as a function of total melt layer thickness. The symbols and line styles correspond to those in Fig. 4.5.

constant, $z_i$ the nominal charge of ion $i$ (-2 for oxygen, +2 for Mg, +4 for Si) and $c_i$ the concentration of element $i$ (0.6 for oxygen, 0.2 for Mg and Si). The particle density of $7.66 \times 10^{28} \mathrm{m}^{-3}$ was obtained from the molecular dynamics simulation of the 480 ion bulk melt. Using average $D^{bulk}$ of $11.2 \times 10^{-6} \mathrm{cm}^2/\mathrm{s}$, $2.1 \times 10^{-6} \mathrm{cm}^2/\mathrm{s}$ and $2.9 \times 10^{-6} \mathrm{cm}^2/\mathrm{s}$ for Mg, Si and O, an electrical conductivity of 161 S/m is obtained. The corresponding partial contributions are 64 S/m (40%) for Mg, 48 S/m (30%) for Si and 49 S/m (30%) for O.

The calculated electrical conductivity of the melt is consistent with experimental data of (ten Grotenhuis et al., 2005). Extrapolation of their bulk melt conductivities to 2000 K gives a slightly lower value of about 130 S/m. The estimated conductivity from the simulation probably constitutes an upper limit since blocking and correlation effects

were not taken into account and all particles were treated as purely ionic. Our results suggest that for $MgSiO_3$ melt all ionic species contribute almost equally to the electrical conductivity.

In rocks with very thin melt films as they are expected as initial melts (Wirth, 1996) or under well wetting conditions, the thin interfacial layer may contribute significantly to the overall conductivity. In partially molten rocks, the electrical conductivity is mainly limited by the smallest junction of the melt. Considering the reduced self-diffusion coefficients for the ultrathin melt films studied here, the reduction in electrical conductivity or the anisotropy of the electrical conductivity in aggregates with preferred orientations should not exceed a factor of two if caused by interfacial layers only. Potentially, such simulations of partially molten rocks could be extended to sample the phase behavior and to study differentiation processes in model systems at varying $P-T$ conditions but also for different chemical composition.

## 4.5 Viscosity Dependence on Shear Rate

The observed behavior between viscosity and shear rate as shown in figure 3.28 is known as *non-Newtonian*. We found a strong shear rate dependency of viscosity. The viscosity of *non-Newtonian* fluids is dependent on shear rate and temperature. In *Newtonian* liquids, the viscosity is independent of the shear rate (Gohar, 2001).

All the data for bulk melt and interfaces show essentially a universal behavior (Fig. 3.28). At the lowest shear rates accessible to NEMD ($10^{+5} - 10^{-2}$) the macroscopic viscosity is approached. On the MD time scale it is not possible to apply smaller shear rates. Methods of non-equilibrium molecular dynamics simulations also have some limitations for predicting the *Newtonian* viscosity of fluid. A similar trend of shear rate dependent viscosity is observed for alkane fluids via equilibrium and non-equilibrium

molecular simulations (McCabe et al., 2002; Daivis and Evans, 1994). McCabe et. al. extrapolate their results (Non-Newtonian viscosities) for alkane fluid to get Newtonian viscosity from NEMD (McCabe et al., 2002).

Our results indicates that the NEMD method is not sensitive enough to resolve a possible dependence of the viscosity on melt thickness and surface termination.

# Chapter 5

# Conclusion

The most important conclusions from this thesis are,

- The thickness of a silicate melt films confined between two crystals has a significant effect on the self-diffusion coefficients of the melt.

- For ultrathin melt films between two forsterite grains the crystal orientation is important. An inverse relationship is observed between the self-diffusion coefficients of the centered melt and the surface energy of the confining crystal grains.

- For a $MgSiO_3$ melt, all ionic species contribute equally to the electrical conductivity. Under well wetting conditions, the thin interfacial layer may contribute significantly to the overall conductivity.

- Both equilibrium and non-equilibrium molecular dynamics simulations gives reasonable values for the melt viscosity at the lower shear rates. Good agreement with experimental data is observed for $MgSiO_3$ melt at 2000 K and 0 GPa.

- A strong shear rate dependence of viscosity is observed on non-equilibrium MD simulations. This method is not very sensitive to resolve a possible dependence of the viscosity on crystal (grain) orientations and melt thickness.

# Bibliography


O. Adjaoud, G. Steinle-Neumann, and S. Jahn. $Mg_2SiO_4$ liquid under high pressure from molecular dynamics. *Chem. Geol.*, 256:184–191, 2008.

O. Adjaoud, G. Steinle-Neumann, and S. Jahn. Transport properties of $Mg_2SiO_4$ liquid at high pressure: Physical state of a magma ocean. *Earth Planet. Sci. Lett.*, 312: 463–470, 2011.

C. B. Agee. Phase transformations and seismic structure in the upper mantle and transition zone. *Rev. Mineral. Geochem.*, 37:165–203, 1998.

A. Aguado, L. Bernasconi, S. Jahn, and P. A. Madden. Multipoles and interaction potentials in ionic materials from planewave-dft calculations. *Faraday Discuss.*, 124: 171–184, 2003a.

A. Aguado, L. Bernasconi, and P. A. Madden. Interionic potentials from ab initio molecular dynamics: The alkaline earth oxides CaO, SrO and BaO. *J. Chem. Phys.*, 118:5704–5717, 2003b.

C. Alba-Simionesco, B. Coasne, G. Dosseh, G. Dudziak, K. E. Gubbins, R. Radhakrishnan, and M. Silwinska-Bartkowiak. Effect of confinement on freezing and melting. *J. Phys.: Condens. Matter*, 18:R15–R68, 2006.

M. Alcoutlabi and G. B. McKenna. Effects of confinement on material behaviour at the nanometer size scale. *J. Phys.: Condens. Matter*, 17:R461–R524, 2005.

D. Alfe. Melting curve of MgO from first-principles simulations. *Phys. Rev. Lett.*, 94: 235701, 2005.

M. P. Allen and D. Tildesley. *Computer Simulation of Liquids*. Oxford Science Publications, 1987.

D. L. Anderson. *New theory of the Earth*. Cambridge University Press, 2007.

D. L. Anderson. *Theory of the Earth*. Blackwell, Boston, 1989.

D. Anthony, P. T. Simon, and A. V. O. James. *Time scales of Magmatic Processes: From Core to Atmosphere*. Blackwell Publishing Ltd., 2011.

W. T. Ashurst and W. G. Hoover. Dense-fluid shear viscosity via non-equilibrium molecular dynamics. *J. phys. Rev. A*, 11:658–678, 1975.

W. T. Ashurst and W. G. Hoover. Shear viscosity via periodic nonequilibrium molecular dynamics. *Phys. lett. A*, 61:175–177, 1977.

K. Baba, A. D. Chave, R. L. Evans, G. Hirth, and R. L. Mackie. Mantle dynamics beneath the east pacific rise at 17°s: insights from the mantle electromagnetic and tomography (melt) experiment. *J. Geophys. Res.*, 111:B02101, 2006.

D. R. Baker. Granitic melt viscosities: Empirical and configurational entropy models for their calculation. *Am. Mineral.*, 81:126–134, 1996.

A. B. Belonoshko and L. S. Dubrovinsky. Molecular dynamics of Nacl (B1 and B2) and MgO (B1) melting: Two-phase simulation. *Am. Mineral.*, 81:303–316, 1996.

F. Bertaut. The electrostatic term of the surface energy. *CR Acad Sci.*, 246:3447, 1958.

C. R. Bina. Patterns of deep seismisity reflect buoyancy stresses due to phase transitions. *GeoPhy. Res. Lett.*, 24:3301–3304, 1997.

Y. Bottinga and D. F. Weill. The viscosity of magmatic silicate liquids: A model for calculation. *Amer. J. Sci.*, 272:438–475, 1972.

N. L. Bowen and O. Andersen. The binary system MgO-$SiO_2$. *Am. J. Sci.*, 37:487–500, 1914.

W. L. Bragg and G. D. Brown. Die Struktur des Olivins. *Z. Kristallgr*, 63:538, 1926.

H. Brasse and D. Eydam. Electrical conductivity beneath the bolivian orocline and its relation to subduction processes at the south american continental margin. *J. Geophys. Res.*, 113:B07109, 2008.

G. Y. Bussod and J. M. Christie. Textural development and melt topology in spinel iherzolte experimentally deformed at hypersolidus conditions. *J. Petrol.*, Spec. Issue,: 17–39, 1991.

C. R. A. Catlow, I. D. Faux, and M. J. Norgett. Shell and breathing shell model calculations for defect formation energies and volumes in magnesium oxide. *J. Phys. C: Solid State Phys.*, C9:419–429, 1976.

C. R. A. Catlow, C. M. Freeman, M. S. Islam, R. A. Jackson, M. Leslie, and S. M. Tomlinson. Interatomic potentials for oxides. *Phil. Mag. A*, 58:123–141, 1988.

M. Cmiral, J. D. Fitz Gerald, U. H. Faul, and D. H. Green. A close look at dihedral angles and melt geometry in olivine basalt aggregates: A TEM study. *Contrib. Mineral. Petrol.*, 130:336–345, 1998.

R. E. Cohen, L. L. Boyer, and M. J. Mehl. Lattice dynamics of the potential-induced breathing model: Phonon dispersion in the alkaline-earth oxides. *Phys. Rev.*, B35: 5749–5760, 1987.

R. F. Cooper and D. H. Kohlstedt. Solution-precipitaion enhanced diffusional creep of partially molten olivine basalt aggregates during hot-pressing. *Tectonophysics*, 107: 207–233, 1984.

R. F. Cooper and D. H. Kohlstedt. Rheology and structure of olivine-basalt partial melt. *J. Geophys. Res.*, 91:9315–9323, 1986.

P. T. Cummuings and G. P. Morriss. Non-equilibrium molecular dynamics calculation of the shear viscosity of liquid rubidium. *J. Phys. F: Met. Phys*, 17:593–604, 1987.

P. J. Daivis and D. J. Evans. Comparison of constant pressure and constant volume non-equilibrium simulations of sheared model decane. *J. Chem. Phys.*, 100:541–547, 1994.

J. H. Davies and D. J. Stevenson. Physical model of source region of subduction zone volcanics. *J. Geophys. Res.*, 97:2037–2070, 1992.

R. de Kloe, M. R. Drury, and van Roermund H. L. M. Evidence for stable grain boundary melt films in experimentally deformed olivine-orthopyroxene rocks. *Phys. Chem. Minerals*, 27:480–494, 2000.

W. A. Deer, R. A. Howie, and J. Zussman. *Rock-forming minerals*. Geological Society, Nature, 1997.

B. G. Dick and A. W. Overhauser. Theory of the dielectric constants of alkali halide crystals. *Phys. Rev.*, 112:90–103, 1958.

M. R. Drury and J. D. Fitz Gerald. Grain boundary melt film in an experimentally deformed olivine-orthopyroxene rock: Implications for melt distribution in upper mantle. *J. Geophys. Res.*, 23(7):701–704, 1996.

D. W. Eaton, F. Darbyshire, R. L. Evans, H. Grutter, A. Jones, and X. Yuan. The elusive lithosphere-asthenosphere boundary (lab) beneath cratons. *Lithos*, 109:1–22, 2009.

D. J. Evans. Nonlinear viscous flow in the Lennard-Jones fluid. *Phys. Lett.*, 74A: 229–232, 1979.

D. J. Evans. Rheology and thermodynamics from non-equilibrium molecular dynamics. *Int. J. Thermophys.*, 7:573–584, 1986.

D. J. Evans and W. G. Hoover. Flows far from equilibrium via molecular dynamics. *Ann. Rev. Fluid Mech.*, 18:243–264, 1986.

P. Ewald. Die Berechnung optischer und elektrostatischer Gitterpotentiale. *Ann. Phys.*, 64:253–287, 1921.

U. H. Faul, J. D. Fitz Gerald, and I. Jackson. Shear wave attenuation and dispersion in melt-bearing olivine polycrystals: 2. microstructural interpretation and seismological implications. *J. Geophys. Res.*, 109:B06202, 2004.

D. Frenkel and B. Smit. *Understanding Molecular Simulation: From Algorithm to Application.* Academic Press, 2001.

K. Fujino, S. Saaski, Y. Takeuchi, and R. Sadanaga. X-ray determination of electron distributions in forsterite,fayalite and tephroite. *Acta Cryst. B*, 37:513–518, 1981.

N. G. Fuller and R. L. Rowley. Non-equilibrium molecular dynamics simulations of shear viscosity of polar liquids. *Int. J. Thermophys.*, 19:1039–1048, 1998.

M. J. Gillan, D. Alfe, J. Brodholt, L. Vocadlo, and G. D. Price. First-principles modelling of earth and planetary materials at high pressures and temperatures. *Rep. Prog. Phys.*, 69:2365–2441, 2006.

D. Giordano and J. K. Russell. A rheological model for glass forming silicates melts in the systems CAS, MAS, MCAS. *J. Phys. Condens. Matter*, 19:205148, 2007.

D. Giordano, J. K. Russell, and D. B. Dingwell. Viscosity of magmatic liquids: A model. *Earth Planet. Sci. Lett.*, 271:123–134, 2008.

R. Gohar. *Elastohydrodynamics*. Imperial College Press, 2001.

B. Guillot and N. Sator. A computer simulation study of natural silicate melts. part i: Low pressure properties. *Geochim. Cosmochim. Acta*, 71:1249–1265, 2007a.

B. Guillot and N. Sator. A computer simulation study of natural silicate melts. part ii: High pressure properties. *Geochim. Cosmochim. Acta*, 71:4538–4556, 2007b.

R. J. Heaton, P. A. Madden, S. J. Clark, and S. Jahn. Condensed phase ionic polarizabilities from plane wave density functional theory calculations. *J. Chem. Phys.*, 125: 144104, 2006.

K. U. Hess and D. B. Dingwell. Vicosities of hydrous leucogranitic melts: A non-arrhenian model. *Am. Mineral.*, 81:1297–1300, 1996.

P. C. Hess. Thermodynamics of thin fluid films. *J. Geophys. Res.*, 99:7219–7229, 1994.

T. Hiraga, I. M. Anderson, and D. L. Kohlstedt. Chemistry of grain boundaries in mantle rocks. *Am. Mineral.*, 88:1015–1019, 2003.

G. Hirth and D. H. Kohlstedt. Experimental constraints on the dynamics of the partially molten upper mantle:deformation in the diffusion creep regime. *J. Geophys. Res.*, 100: 1981–2001, 1995.

W. G. Hoover. Non-equilibrium molecular dynamics: the first 25 years. *Physica A*, 194: 450–461, 1993.

W. G. Hoover and C. G. Hoover. Non-equilibrium molecular dynamics. *Condens. Matter Phys.*, 8:247–260, 2005.

W. G. Hoover and C. G. Hoover. Nonlinear stresses and temperatures in transient adiabatic and shear flows via nonequilibrium molecular dynamics: Three definitions of temperature. *Phys. Rev. E*, 79:1, 2009.

H. Hui and Y. Zhang. Towards a general viscosity equation for natural anhydrous and hydrous silicate melts. *Geochim. Cosmochim. Acta*, 71:403–416, 2007.

S. Jahn. High-pressure phase transitions in $MgSiO_3$ orthoenstatite studied by atomistic computer simulation. *Am. Mineral.*, 93:528–532, 2008.

S. Jahn. Integral modelling approach to study the phase behavior of complex solids: Application to phase transition in $MgSiO_3$ pyroxene. *Acta. Cryst.*, A66:535–541, 2010.

S. Jahn and P. A. Madden. Modeling earth materials from crustal to lower mantle conditions: A transferable set of interaction potentials for the cmas system. *Phys. Earth Planet. Int.*, 162:129–139, 2007.

S. Jahn and R. Martoňák. Plastic deformation of orthoenstatite and the ortho- to high-pressure clinoenstatite transition: A metadynamics simulation study. *Phys. Chem. Minerals*, 35:17–23, 2008.

S. Jahn and R. Martoňák. Phase behavior of protoenstatite at high pressure studied by atomistic simulations. *Am. Mineral.*, 94:950–956, 2009.

S. Jahn, P. A. Madden, and M. Wilson. Transferable interaction model for $Al_2O_3$. *Phys. Rev. B*, 74:024112, 2006.

S. Karato. Does partial melting reduce the creep strength of the upper mantle? *Nature*, 319:309–310, 1986.

B. B. Karki and L. P. Stixrude. Viscosity of $MgSiO_3$ liquid at earth's mantle conditions: Implications for an early magma ocean. *Science*, 328:740–742, 2010.

J. Kendrick and W. C. Mackrodt. Interatomic potentials for ionic materials from first principles calculations. *Solid State Ionics.*, 8:247–253, 1983.

D. H. Kohlstedt. Structure, rheology and permeability of partially molten rocks at melt low fractions. in mantle flow and melt generation at mid-ocean ridges. *Geophys. Monogr, Phipps-Morgan J, Blackman DK, and Sinton JM (eds) American geophysical Union, Washington DC*, 71:103–121, 1992.

D. H. Kohlstedt and M. E. Zimmerman. Rheology of partially molten mantle rocks. *Annu. Rev. Earth Planet. Sci.*, 24:41–62, 1996.

D. L. Kohlstedt and B. K. Holtzman. Shearing melt out of the earth: An experimentalist's perspective on the influence of deformation on melt extraction. *Annu. Rev. Earth Planet. Sci.*, 37:561–593, 2009.

E. A. Kozlovsky and N. Andrianov. *The Superdeep well of the Kola Peninsula.* Springer-Verlag, New York, 1987.

I. Kushiro. Density and viscosity of hydrous calc-alkalic andesite magma at high pressures. *Year B.-Carnegie Inst. Wash. Sci. Lett.*, 77:675–678, 1978a.

I. Kushiro. Viscosity and structural changes of albite ($NaAlSi_3O_8$) melt at high pressures. *Earth Planet. Sci. Lett.*, 41:87–90, 1978b.

R. A. Lange and I. S. E. Carmichael. Densities of $Na_2O$-$K_2O$-CaO-MgO-FeO-$Fe_2O_3$-$Al_2O$-$TiO_2$-$SiO_2$ liquids: New measurements and derived partial molar properties. *Geochim. Cosmochim. Acta*, 51:2931–2946, 1987.

O. J. Lanning, S. Shellswell, and P. A. Madden. Solid-liquid coexistence in ionic systems and the properties of the interface. *Mol. Phys.*, 102:839–855, 2004.

C. Liebske, B. Schmickler, H. Terasaki, B. T. Poe, A. Suzuki, K. Funakoshi, R. Ando, and D. C. Rubie. Viscosity of peridotite up to 13 GPa: Implications for magma ocean viscosities. *Earth Planet. Sci. Lett.*, 240:589–604, 2005.

P. A. Madden and M. Wilson. 'covalent' effects in 'ionic' liquids. *J. Phys.: Condens. Matter*, 12:A95–A108, 2000.

P. A. Madden, R. Heaton, A. Aguado, and S. Jahn. From first-principles to material properties. *J. Mol. Struc. (Theochem)*, 771:9–18, 2006.

E. Madelung. Das elektrische feld in systemen von regelmÃ¤ssig angeordneten punktladungen. *Phys. Z.*, 19:524–532, 1918.

G. B. Martin, F. J. Spera, M. S. Ghiorso, and D. Navins. Structure, thermodynamics, and transport properties of molten $Mg_2SiO_4$: molecular dynamics simulations and model eos. *Am. Mineral.*, 94:693–703, 2009.

G. J. Martyna, D. J. Tobias, and M. L. Klein. Constant pressure molecular dynamics algorithms. *J. Chem. Phys.*, 101:4177–4189, 1994.

M. Matsui. Molecular dynamices simulation of $MgSiO_3$ perovskite and the 660-km seismic discontinuity. *Phys.Earth Planet. Int.*, 121:77–84, 2000.

M. Matsui. A transferable interatomic potential model for crystals and melts in the system CaO-MgO-$Al_2O_3$-$SiO_2$. *Mineral. Mag.*, 58a:571–572, 1994.

M. Matsui. Molecular dynamics simulation of structures, bulk moduli, and volume thermal expansivities of silicate liquids in the system CaO-MgO-$Al_2O_3$-$SiO_2$. *Geophys. Res. Lett.*, 23:395–398, 1996.

M. Matsui. Computational modeling of crystals and liquids in the system $Na_2O$-CaO-MgO-$Al_2O_3$-$SiO_2$. *Geophysical Monograph (AGU)*, 101:145–151, 1998a.

M. Matsui. Breathing shell model in molecular dynamics simulation: Application to MgO and CaO. *J. Chem. Phys.*, 108:3304–3309, 1998b.

M. Matsui. Computer simulation of the $Mg_2SiO_4$ phases with application to the 410 km seismic discontinuity. *Phys. Earth Planet. Int.*, 116:9–18, 1999.

M. Matsui, S. C. Parker, and M. Leslie. The MD simulation of the equation of state of MgO: Application as a pressure calibration standard at high temperature and high pressure. *Am. Mineral.*, 85:312–316, 2000.

S. Matsunaga. Structural study on liquid Au-Cs alloys by computer simulations. *J. Phys. Soc. Jpn.*, 69:1712–1716, 2000.

J. Maumus, N. Bagdassrov, and H. Schmeling. Electrical conductivity and partial melting of mafic rocks under pressure. *Geochim. Cosmochim. Acta*, 69:4703–4718, 2005.

C. McCabe, C. W. Manke, and P. T. Cummings. Predicting the newtonian viscosity of complex fluids from high strain rate molecular simulations. *J. Chem. Phys.*, 116: 3339–3342, 2002.

S. Mei and D. H. Kohlstedt. Influence of water on plastic deformation of olivine aggregates:1.diffusion creep regime. *J. Geophys. Res.*, 105:21457–21481, 2000.

S. Mei, W. Bai, T. Hiraga, and D. H. Kohlstedt. Influence of melt on the crppe behavior of olivine-basalt aggregates under hydrous conditions. *Earth Planet. Sci. Lett.*, 201: 491–501, 2002.

T. Naitoh and S. Ono. The shear viscosity of hard-sphere fluid via non-equilibrium molecular dynamics. *Phys. Lett.*, 57A:448–450, 1976.

T. Naitoh and S. Ono. The shear viscosity of hard-sphere fluid via non-equilibrium molecular dynamics. *J. Chem. Phys.*, 70:4515–4523, 1979.

D. Nevins, J. S. Frank, and M. S. Ghiorso. Shear viscosity and diffusion in liquid $MgSiO_3$: Transport properties and implications for terrestrial planet magma ocean. *Am. Mineral.*, 94:975–980, 2009.

S. Nosé and M. L. Klein. Constant pressure molecular dynamics for molecular systems. *Mol. Phys.*, 50:1055–1076, 1983.

G. M. Partzsch, F. R. Schilling, and J. Arndt. The influence of partial melting on the electrical behavior of crustal rocks: laboratory examinations, model calculations and geological interpretations. *Tectonophysics*, 317:189–203, 2000.

J. P. Poirier. *Introduction to the Physics of the Earth's Interior*. Cambridge: Cambridge University Press, 2000.

D. C. Presnall. *Mineral Physics and Crystallography, A Handbook of Physical Constants*, volume 2 of *AGU Reference Shelf*, chapter Phase diagrams of Earth-forming minerals, pages 248–268. American Geophysical Union, 1995.

A. Putnis. *Introduction to mineral sciences*. Cambridge University Press, 1992.

J. E. Reid, A. Suzuki, K. Funakoshi, H. Terasaki, B. T. Poe, D. C. Rubie, and E. Ohtani. The viscosity of $CaMgSi_2O_6$ liquid at pressure up to 13 GPa. *Phys. Earth Planet. Inter.*, 139:45–54, 2003.

G. N. Riley and D. H. Kohlstedt. An experimental study of melt migration in an olivine-melt system. in magma transport and storage. *John Wiley and Sons, New York*, pages 77–86, 1990.

J. J. Roberts and J. A. Tyburczy. Impedance spectroscopy of single and polycrystalline olivine: Evidence for grain boundary transport. *Phys. Chem. Minerals*, 20:19–26, 1993.

J. J. Roberts and J. A. Tyburczy. Partial melt electrical conductivity: Influence of melt composition. *J. Geophys. Res.*, 104(B4):7055–7065, 1999.

D. C. Rubie, H.J. Melosh, J. E. Reid, and K. Righter. Mechanisms of metal-silicates equilibrium in the terrestrial magma ocean. *Earth Planet. Sci. Lett.*, 205:239–255, 2003.

H. Sato and Y. Ida. Low frequency electrical impedence of partially molten gabbro: The effect of melt geometry on electrical properties. *Tectononphysics*, 107:105–134, 1984.

H. Schmeling. Numerical models on the influence of partial melt on elastic, anelastic and electrical properties of rocks. part 1: elasticity and anelasticity. *Phys. Earth Planet. Int.*, 41:34–57, 1985.

H. Schmeling. Numerical models on the influence of partial melt on elastic, anelastic and electrical properties of rocks. part 2: electrical conductivity. *Phys. Earth Planet. Int.*, 43:123–136, 1986.

V. S. Solomatov and D. J. Stevenson. Kinetics of crystal growth in a terrestrial magma ocean. *J. Geophys. Res.*, 98 (E3):5407–5418, 1993a.

V. S. Solomatov and D. J. Stevenson. Suspension in convective layers and style of differentiation of a terrestrial magma ocean. *J. Geophys. Res.*, 98 (E3):5407–5418, 1993b.

A. J. Stone. *The theory of intermolecular forces.* Oxford University Press, Oxford, 1996.

I. Suzuki, O. L. Anderson, and Y. Sumino. Elastic properties of a single-crystal forsterite $Mg_2SiO_4$ up to 1200 k. *Phys. Chem. Minerals*, 10:38–64, 1983.

P. J. Tackley. Dynamics and evolution of the deep mantle resulting from thermal, chemical, phase and melting effects. *Earth-Sci. Rev.*, 110:1–25, 2012.

K. T. Tang and J. P. Toennies. An improved simple model for the van der waals potential based on universal damping functions for the dispersion coefficients. *J. Chem. Phys.*, 80:3726–3741, 1984.

P. Tangney and S. Scandolo. An ab-initio parametrized interatomic force field for silica. *J. Chem. Phys.*, 117:8898–8904, 2002.

Y. Tatsumi. Migration of fluid phasesand genesis of basalt magmas in subduction zones. *J. Geophys. Res.*, 94:4697–4707, 1989.

S. M. ten Grotenhuis, M. R. Drury, C. J. Peach, and C. J. Spiers. Electrical properties of fine-grained olivine: Evidence for grain boundary transport. *J. Geophys. Res.*, 109: B06203, doi:10.1029/2003JB002799, 2004.

S. M. ten Grotenhuis, M. R. Drury, C. J. Spiers, and C. J. Peach. Melt distribution in olivine rocks based on electrical conductivity measurements. *J. Geophys. Res.*, 110: B12201, doi:10.1029/2004JB003462, 2005.

D. A. Toffelmier and J. A. Tyburczy. Electromagnetic detectio of a 410-km-deep melt layer in the southwestern united states. *Nature*, 447:991–994, 2007.

W. B. Tonk and H. J. Melosh. *The physics of crystal settling and suspension in a turbulent magma ocean. In: N.E. Newsom and J.H. Jones, Editors, Origin of the Earth.* Oxford University Press, New York, 1990.

G. Urbain, Y. Bottinga, and P. Richet. Viscosity of liquid silica, silicates and aluminosilicates. *Geochim. Cosmochim. Acta*, 46:1061–1072, 1982.

B. W. H. van Beest, G. J. Kramer, and R. A. van Santen. Force fields of silicas and aluminophosphates based on ab initio calculations. *Phys. Rev. Lett.*, 64:1955–1958, 1990.

H. S. Waff and J. R. Bulau. Equilibrium fluid distribution in an ultramafic partial melt under hydrostatic stress conditions. *J. Geophys. Res.*, 84(B11):6109–6114, 1979.

H. S. Waff and J. R. Bulau. Experimental determination of near-equilibrium textures in partially molten silicates at high pressures. *Adv. Earth Planet. Sci.*, 12:229–236, 1982.

H. S. Waff and U. H. Faul. Effects of crystalline anisotropy on fluid distribution in ultramafic partial melts. *J. Geophys. Res.*, 97(B6):9003–9014, 1992.

A. M. Walker, K. Wright, and B. Slater. A computational study of oxygen diffusion in olivine. *Phys. Chem. Minerals*, 30:536–545, 2003.

J. T. K. Wan, T. S. Duffy, S. Scandolo, and R. Car. First principles study of density, viscosity, and diffusion coefficients of liquid $MgSiO_3$ at conditions of the earth's deep mantle. *J. Geophys. Res.*, 112:B03208, 2007.

G. W. Watson, P. M. Oliver, and S. C. Parker. Computer simulation of the structure and stability of forsterite surfaces. *Phys. Chem. Minerals*, 25:70–78, 1997.

M. Wilson and P. A. Madden. Polarization effects in ionic systems from first principles. *J. Phys.: Condens. Matter*, 5:2687–2706, 1993.

M. Wilson, P. A. Madden, and B. J. Costa-Cabral. Quadrupole polarization in simulations of ionic systems: Application to agcl. *J. Phys. Chem.*, 100:1227–1237, 1996a.

M. Wilson, P. A. Madden, M. Hemmati, and C. A. Angell. Polarization effects, network dynamics, and the infrared spectrum of amorphous $SiO_2$. *Phys. Rev. Lett.*, 77:4023–4026, 1996b.

M. Wilson, P. A. Madden, N. C. Pyper, and J. H. Harding. Molecular dynamics simulations of compressible ions. *J. Chem. Phys.*, 104:8068–8081, 1996c.

J. D. Winter. *An introduction to igneous and metamorphic petrology.* Prentice-Hall Inc., 2001.

R. Wirth. Thin amorphous films (1-2 nm) at olivine grain boundaries in mantle xenoliths from San Carlos, Arizona. *Contrib. Mineral. Petrol.*, 124:44–54, 1996.

T. Yoshino, Y. Takei, D. A. Wark, and E. B. Watson. Grain boundary wetness of texturally equilibrated rocks, with implications of seismic properties of the upper mantle. *J. Geophys. Res.*, 110:B08205, 2005.

T. Yoshino, D. Yamazaki, and K. Mibe. Well-wetted olivine grain boundaries in partially molten peridotite in the asthenosphere. *Earth Planet. Sci. Lett.*, 283:167–173, 2009.

S. Yoshioka, H. Hayashi, A. Kuwabara, F. Oba, K. Matsunaga, and I. Tanaka. Structures and energetics of $Ga_2O_3$ polymorphs. *J. Phys.: Condens. Matter*, 19:346211, 2007.